Attosecond Sources and Interferometers - Developments and Applications

Witting Larsen, Esben

2016

Document Version:
Early version, also known as pre-print

Attosecond Sources and Interferometers - Developments and Applications

Esben Witting Larsen

Doctoral Thesis
2016

Lund University

Akademisk avhandling som för avläggande av teknologie doktorsexamen vid tekniska fakulteten vid Lunds Universitet kommer att offentligen försvaras den 16 september 2016, kl. 09.15 i Rydbergssalen, på Fysiska Institutionen, Professorsgatan 1, Lund.

Fakultetsopponent: Dr. Caterina Vozzi
Institute for Photonics and Nanotechnologies,
Italian National Research Council (IFN-CNR), Milan, Italy.

Academic dissertation which, by due permission of the Faculty of Engineering at Lund University, will be publicly defended on September 16th, 2016, at 09.15 a.m. in the Rydberg's hall, at the Department of Physics, Professorsgatan 1, Lund, for the degree of Doctor of Philosophy in Engineering.

Faculty opponent: Dr Caterina Vozzi
Institute for Photonics and Nanotechnologies,
Italian National Research Council (IFN-CNR), Milan, Italy.

Attosecond Sources and Interferometers
- Developments and Applications

Printed in Sweden by Media-Tryck, Lund, 2016

Division of Atomic Physics
Department of Physics
Faculty of Engineering, LTH
Lund University
P.O. Box 118
SE–221 00 Lund
Sweden

http://www.atomic.physics.lu.se

ISSN: 0281-2762
Lund Reports on Atomic Physics, LRAP 518 (2016)

ISBN (PRINT): 978-91-7623-893-6
ISBN (PDF): 978-91-7623-894-3

Keywords: High-order harmonic generation, Attosecond interferometry
Electron spectroscopy, Transient absorption, Free induction decay.

PACS: 29.30.Dn, 32.60.+i, 32.80.Rm, 32.80.Qk,
32.80.Zb, 42.50.Md, 42.65.Ky, 78.47.jb.

To the old Atomic Physics coffee machine;
you may have been replaced by a fancy young model,
but without you this work would not have been possible.

Abstract

Attosecond science deals with atomic physics on the natural time scale of electron motion in atoms and molecules. According to the Bohr model, the time taken for one orbit of an electron in the ground state of a hydrogen atom is 150 attoseconds (1 as = 10^{-18} s). In order to resolve motion on this short timescale, attosecond light pulses are nowadays routinely applied in a steadily increasing number of laboratories. Attosecond experiments usually utilize a scheme called pump-probe. The pump-probe technique relies on two pulses. The first pulse, called the pump, is used to initiate a dynamic process, while the second pulse, the probe, is used to terminate the process and generate a readout signal. The readout signal carries information on the dynamics of the process, and therefore depends on the precise delay between the two light pulses. The delay must consequently be controlled and varied with attosecond precision in order to obtain information on the system.

Attosecond pulses are produced through the process of high-order harmonic generation (HHG), and come in two forms; either as a single attosecond pulse, or as a train of attosecond pulses. The latter is technically easier to achieve and additionally has the benefit of being applicable for an interferometric technique called the reconstruction of attosecond beating by interfering two-photon transitions (RABBITT), which allows for time-delay measurements in the attosecond regime. Although, attosecond pulses are becoming widely available, the attosecond toolbox has until recently been limited to experiments on the dynamics of valence electrons, and the experiments have often suffered from large interferometric instabilities as well as instability in the attosecond pulse sources.

This thesis is concerned with three main topics. The first research topic is improvement of the attosecond sources. Various ways of improving the attosecond sources are presented, such as performing the HHG process with more reliable laser systems, increasing the tunability of the attosecond pulses by driving the HHG with frequency tunable lasers, and extending the harmonics to higher photon energies through the use of long wavelength drivers. The second research topic of the thesis deals with improvements of the interferometric stability of attosecond experiments through the development of high-stability interferometers, which were tested on demanding applications. The final research topic of the thesis deals with improving the controllability of extreme ultraviolet (XUV) pulses through the development of a technique to control the spatial phase of XUV light, in the pursuit of an opto–opto modulator in the XUV.

The first decade of attosecond physics has seen the demonstration of numerous proof-of-principle experiments. Many of these experiments suffered from relatively large uncertainties and a lack of reproducibility. The work described in this thesis has

helped in obtaining more reliable and reproducible measurements, providing better control of the dynamics, while at the same time, improving the usability.

Populærvidenskabeligt Resumé

Hvad er et øjeblik? Et atom består af en atomkerne omringet af sky af elektroner. Udsættes atomet for en meget kraftigt laser begynder elektronerne at vibrere, og hele elektronskyen begynder at forskydes. Hvis laseren er kraftig nok bliver enkelte elektroner så forskudt fra atomkernen, at de bliver løsrevet fra resten af atomet. De løsrevne elektroner vender aldrig tilbage til atomet - selv hvis man slukker for laseren igen. Vi kalder atomet uden de frigjorte elektroner for en ion, mens de frigjorte elektroner kaldes for fotoioniserede elektroner. Selve processen kaldes for den fotoelektriske effekt og blev første gang observeret i 1887 af Heinrich Hertz. Hertz's eksperiment viste desuden, at det ikke alene var lysets styrke, men også dets farve, der afgør om et atom bliver ioniseret. I 1905 udgav Einstein en artikel, hvori han forklarede den fotoelektriske effekt ved at kvantisere lyset. Dvs. Einstein antog at lys bestod af små partikler, såkaldte fotoner, som havde en bestemt energi afhængigt af farven. I artiklen blev det videre antaget, at lysets energi er linært proportionalt med dets frekvens, således at en rød foton havde mindre energi end en blå foton. Hvis en foton havde højere energi end bindingsenergien for elektronen var det dermed muligt at fotoionisere atomet. Einstein blev i 1921 tildelt nobelprisen i fysik for denne forklaring. Så selvom den grundlæggende forståelse af den fotoelektriske effekt har mere end et århundrede på bagen, så kender man ikke detaljerne for hvordan atomet overgår til at være ion. Vi har et nogenlunde billede af hvordan atomet ser ud i begyndelsen, før vi tænder for laseren, og hvordan ionet ser ud efter den fotoelektriske effekt. Men hvordan systemet ser ud, mens laseren er på, er derimod langt sværere at måle.

Problemet kan være lettere at forstå med en analogi fra dagligdagen. Tænker vi stedet på hvad der sker når en dart pil kastes imod en oppustet ballon. Vi ved alle at, hvis pilen rammer ballonen, så er der stor sandsynlighed for at ballonen sprænger. Men er der forskel om ballonen rammes med et stumt objekt, som for eksempel en hammer, i stedet? For det menneskelige øje ser det umiddelbart ud som om ballonen sprænger øjeblikkeligt i begge tilfælde. Men ved nærmere eftertanke kan vi dog forestille os at sprængningerne foregår gradvist, men præcist hvordan og hvorledes er dog svært at få intuitivt billede af.

Spørgsmålet kan dog besvares ved hjælp af moderne højhastighedskameraer, som kan optage billeder på kortere tid end det tager for ballonen at sprænge. Er det muligt at optage mange billeder i tidsrummet, fra pilen kommer i kontakt med ballonen til ballonen sprænger, kan vi skabe en film. Bagefter kan vi se hvordan ballonen mødte sin ende på film, såfremt vi sænker hastigheden tilstrækkeligt.

På samme vis kan vi anvende kameraer til at få adgang til information om universet, som umiddelbart virker usynlige med det blotte øje. For at studere universets

udvikling på stor skala, kan vi anvende teleskoper sammen med kameraer med lang eksponeringstid. Mange har formodentligt set Deep Field billedet optaget af Hubble teleskopet. Hubble teleskopet blev rettet mod et område i universet, der i første ombæring så ud til at være komplet mørkt uden hverken stjerner eller galakser. Men ved at sammensætte 342 billeder optaget i streg med samme kamera over en periode på 10 dage, kunne man i stedet se omkring 3000 galakser i det område, der umiddelbart virkede tomt. Hvert billede blev optaget med en eksponeringstid på mellem 15 og 45 minutter. Hubble teleskopet var i stand til at foretage fotografierne, da eksponeringstiden var så "kort"' at galakserne flyttede sig mindre end en pixel før billedet var taget. Hvis galakserne havde bevæget sig hurtigere, ville vi intet se da billedet blot ville blive sløret. De fleste kender denne udfordring fra dagligdagen, når man vil tage et billede, så er det vigtigt at motivet står stille, mens man tager fotografiet, ellers bliver billedet uskarpt.

Vil man filme et objekt i hurtig bevægelse, som for eksempel en fugl, der basker med sine vinger om natten, kan man i stedet for at anvende en anden teknik. Man kan deaktivere kameraets lukkemekanisme, således at filmen er konstant eksponeret, og så belyse fuglen med korte lyspulser. Kun når fuglen rammes af lyspulserne reflekteres lys tilbage til kameraet og fuglen er synlig. Hvis målingen gentages periodisk kaldes det for en stroboskopisk måling. Dette fænomen er kendt fra dagligdagen fra eksempel dansegulvet på natklubber, hvor stroboskopbelysning kan få folk til at se stillestående ud selvom de danser.

Faktaboks		
1 sekund	1 s	1 s
1 millisekund	10^{-3} s	0.001 s
1 microsekund	10^{-6} s	0.000 001 s
1 nanosekund	10^{-9} s	0.000 000 001 s
1 picosekund	10^{-12} s	0.000 000 000 001 s
1 femtosekund	10^{-15} s	0.000 000 000 000 001 s
1 attosekund	10^{-18} s	0.000 000 000 000 000 001 s
1 zeptosekund	10^{-21} s	0.000 000 000 000 000 000 001 s

Den relevante tid en proces tager er omvendt proportional med størrelsen af objektet, som illustrativt vist i Figur 1. På astronomisk skala kan begivenheder foregå på tidsskaler på helt op til millioner eller sågar milliarder af år, for eksempel rotere mælkevejen med en omløbstid på ca. 250 millioner år. Biologiske objekter som dyr og mennesker kræver tidsopløsning ned til millisekunder. For et elektronisk kredsløb er nanosekunder nødvendigt, mens kemiske processer kan foregå så hurtigt som picosekunder eller sågar femtosekunder. På et sub-atomart niveau omfordeler elektroner sig på endnu kortere tid, nemlig attosekunder for let bundne elektroner, eller sågar zeptosekunder for elektroner nær kernen i store atomer. Disse tidsskaler er så korte, at det kan være næsten umuligt at forestille sig. For at sætte det i perspektiv; et attosekund forholder sig til et sekund på samme vis, som et sekund forholder sig til to gange universets alder! På grund af elektronernes utroligt hurtige bevægelse er det umuligt at direkte filme en elektrons bevægelse og sænke hastigheden, som vi kunne gøre det med ballonen. I stedet må man anvende korte lyspulser, i dette tilfælde laserpulser med varigheder af attosekunder eller femtosekunder. Målet med denne PhD afhandling er at anvende og videreudvikle tekniker, der muliggør direkte målinger af overgangstilstande i atomer. Afhandlingen består af to dele, første del handler om

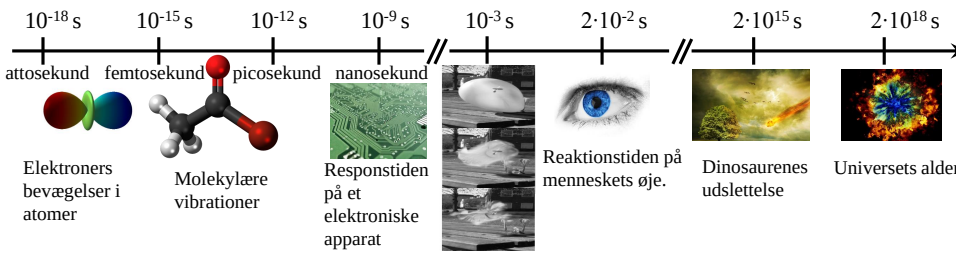

Figur 1: Oversigt over relevante tidsskalaer for forskellige processor.

videre udvikling af lyspulser med laserlignende egenskaber i det ultraviolet område. Disse pulser har typisk en længde på hundredvis af attosekunder, og er derfor ideelle for stroboskoplignende målinger af elektroner. I den anden del af afhandlingen anvendes disse attosekund pulser til blandt andet tidsopløste målinger af den fotoelektriske effekt i diverse ædelgasser. Den mest anvendte teknik for tidsopløste målinger, er en såkaldt pumpe-probe teknik. I pumpe-probe teknikken anvendes to laserpulser. Den første laserpuls (kaldet pumpen) anvendes til at starte en dynamisk process – med andre ord den får elektronerne til at vibrere. Den anden puls (kaldet proben) anvendes til at afslutte processen og skabe et signal, som kan måles med et elektronisk apparat. Dette signal afhænger af tiden der går mellem de to laser pulser. For at få information om elektronbevægelser, er det derfor nødvendigt at have kontrol over tidsforskydelsen mellem to lys pulser med en præcision på omkring 100 attosekunder. I denne afhandling udføres dette ved hjælp af såkaldte optiske interferometre. I et optisk interferometer opdeles en lyspuls i to dele, som forsinkes imod hinanden ved at gøre vejlængden længere for den ene puls. Dette er illustreret i højre side af Figur 2. Efter det optiske interferometer sendes de to pulser ind i en atomar gas, hvori den fotoelektriske effekt foregår. I første ombæring har det været muligt at måle tidsforskelle i fotoionisation af forskellige ædelgasser, men dette er bare begyndelsen. I princippet vil det i fremtiden formodentligt være muligt at måle og muligvis kontrollere for eksempel kemiske reaktioner ved hjælp af lys. Er man i stand til dette vil man potentielt være i stand til at skabe nye og bedre materialer. Derudover kan disse tekniker potentielt skabe højere muligheder for kvalitetskontrol af meget små objekter, som for eksempel fremtidens mikrochips.

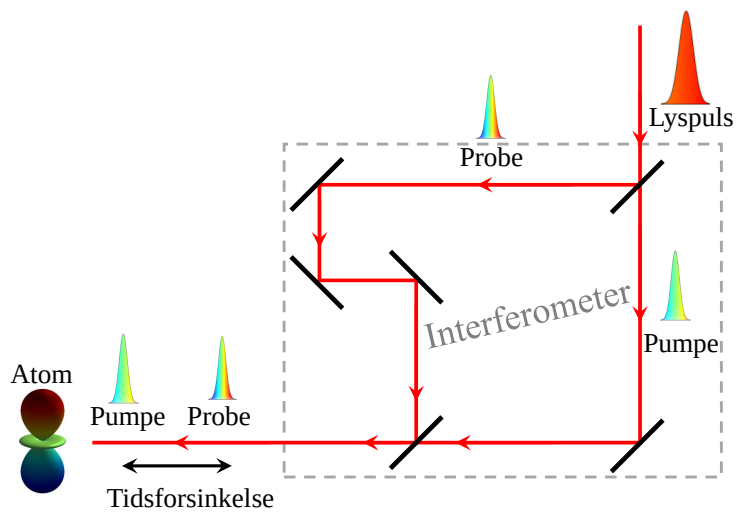

Figur 2: Skematisk illustration af et optisk interferometer. En indkommende lyspuls splittes i to mindre pulser, kaldet en pumpe og en probe puls. De to pulser sendes hver sin vej igennem et interferometer, hvorefter de samles igen. Da pumpe pulsen har en kortere vejlængde igennem interferometret end probe pulsen kommer pumpen hurtigere frem, og dermed opstår en tidsforsinkelse mellem de to pulser.

List of Publications

This dissertation thesis is based on the following papers and manuscripts, which will be referred to in the text by their Roman numerals.

I **High-order harmonic generation using a high-repetition-rate turnkey laser**
E. Lorek, E.W. Larsen, C.M. Heyl, S. Carlström, D. Paleček, D. Zigmantas and J. Mauritsson.
Review of Scientific Instruments **85**, 123106 (2014).

II **Sub-cycle ionization dynamics revealed by trajectory-resolved, elliptically-driven high-order harmonic generation**
E.W. Larsen, S. Carlström, E. Lorek, C.M. Heyl, D. Paleček, K. J. Schafer, A. L'Huiller, D. Zigmantas and J. Mauritsson.
Submitted for publication.

III **Spatially and spectrally resolved quantum path interference with chirped driving pulses**
J. Preclíková, S. Carlström, E. Lorek, E. W. Larsen, C. M. Heyl, D. Paleček, D. Zigmantas, K. J. Schafer, M. Gaarde, and J. Mauritsson.
Submitted for publication.

IV **Carrier-envelope phase-dependent high-order harmonic generation with a high-repetition-rate OPCPA system**
P. Rudawski, A. Harth, C. Guo, E. Lorek, M. Miranda, C.M. Heyl, E.W. Larsen, J. Ahrens, O. Prochnow, T. Binhammer, U. Morgner, J. Mauritsson, A. L'Huillier and C.L. Arnold.
The European Physical Journal D **69**, 1434-6060 (2015).

V **Measurements of relative photoemission time delays in noble gas atoms**
D. Guénot, D. Kroon, E. Balogh, E. W. Larsen, M. Kotur, M. Miranda, T. Fordell, P. Johnsson, J. Mauritsson, M. Gisselbrecht, K. Varjú, C. L. Arnold, T. Carette, A. S. Kheifets, E. Lindroth, A. L'Huillier and J. M. Dahlström.
Journal of Physics B: Atomic, Molecular and Optical Physics **47**, 245602 (2014).

VI **Attosecond pulse walk-off in high-order harmonic generation**
D. Kroon, D. Guénot, M. Kotur, E. Balogh, E. W. Larsen, C. M. Heyl, M. Miranda, M. Gisselbrecht, J. Mauritsson, P. Johnsson, K. Varjú, A. L'Huillier and C. L. Arnold.
Optics Letters **39**, 2218-2221 (2014).

VII **Spectral phase measurement of a Fano resonance using tunable attosecond pulses**
M. Kotur, D. Guénot, Á. Jiménez-Galán, D. Kroon, E. W. Larsen, M. Louisy, S. Bengtsson, M. Miranda, J. Mauritsson, C. L. Arnold, S. E. Canton, M. Gisselbrecht, T. Carette, J. M. Dahlström, E. Lindroth, A. Maquet, L. Argenti, F. Martín and A. L'Huillier.
(2016) *Nature Communications.*

VIII **Gating attosecond pulses in a noncollinear geometry**
M. Louisy, C. L. Arnold, M. Miranda, E. W. Larsen, S. N. Bengtsson, D. Kroon, M. Kotur, D. Guénot, L. Rading, P. Rudawski, F. Brizuela, F. Campi, B. Kim, A. Jarnac, A. Houard, J. Mauritsson, P. Johnsson, A. L'Huillier, and C. M. Heyl.
Optica **2**, 563-566 (2015).

IX **Controlled free induction decay in the extreme ultraviolet**
E.W. Larsen, S. Bengtsson, D. Kroon, S. Camp, M. Miranda, C. L. Arnold, A. L'Huillier, K. J. Schafer, M. Gaarde, L. Rippe, and J. Mauritsson.
Manuscript in preparation.

X **Photoemission electron microscopy of localized surface plasmons in silver nanostructures at telecommunication wavelengths**
E. Mårsell, E. W. Larsen, C. L. Arnold, H. Xu, J. Mauritsson, and A. Mikkelsen.
Journal of Applied Physics **117**, 083104 (2015).

Abbreviations

Abbreviation	Long Form
AOM	Acousto-Optic Modulator
APT	Attosecond Pulse Train
ATAS	Attosecond Transient Absorption Spectroscopy
BBO	Beta Barium Borate
CEP	Carrier–Envelope Phase
CFID	Controlled Free Induction Decay
CPA	Chirped Pulse Amplification
CRAB	Complete Reconstruction of Attosecond Burst
DFG	Difference Frequency Generation
FEL	Free-Electron Laser
FID	Free Induction Decay
FROG	Frequency-Resolved Optical Gating
GD	Group Delay
GDD	Group Delay Dispersion
GV	Group Velocity
GVD	Group Velocity Dispersion
HH	High-order Harmonic
HHG	High-order Harmonic Generation
IR	Infrared
MBES	Magnetic Bottle Electron Spectrometer
MCP	Micro-channel Plate
MRI	Magnetic Resonance Imaging
NIR	Near-Infrared
NOG	Non-collinear Optical Gating
OPA	Optical Parametric Amplification
OPCPA	Optical Parametric Chirped Pulse Amplification
NC-OPA	Non-collinear Optical Parametric Amplifier

C-OPA	Collinear Optical Parametric Amplifier
PEEM	Photo-emission Electron Microscopy
RABBITT	Reconstruction of Attosecond Beating By Interfering Two-photon Transitions
SAP	Single Attosecond Pulse
SFA	Strong-Field approximation
SFG	Sum Frequency Generation
SIR	Short-wavelength Infrared
SPM	Self-Phase Modulation
TDSE	Time-Dependent Schrödinger Equation
TOF	Time Of Flight
TOPAS	Travelling-wave Optical Parametric Amplifier of Superfluorescence
VIS	Visible
WLG	White Light Generation
X-FROG	Cross-correlation frequency-resolved optical gating
XUV	Extreme Ultraviolet ($10 < \hbar\omega < 124$ eV)

List of Symbols

Symbol	Quantity
α_{traj}	Trajectory-dependent dipole phase
b	Confocal parameter
B	Magnetic field
c	Speed of light
ϵ_0	Electric permittivity of the vacuum
E	Energy
$\mathcal{E}$	Electric field
f	Frequency
ϕ	Spectral phase
Φ	Temporal phase
h	Planck's constant
$\hbar$	Reduced Planck constant
I	Intensity/Irradiance
$\mathbf{j}$	Current density
k	Wavenumber
$\mathbf{k}$	Wave vector
λ	Wavelength
μ_0	Magnetic permeability of the vacuum
m_e	Electron mass
n	Refractive index
P	Dielectric polarization
e	Elementary charge
ρ	Charge density
σ	Cross section
t	Time
T	Kinetic energy
T	Period

U_p	Ponderomotive energy
V	Potential energy
w	Spot size
ω	Angular frequency
Ω	Angular frequency of high-order harmonic
ω_p	Plasma frequency
χ	Electric susceptibility
z_R	Rayleigh Length

Contents

Papers

Chapter 1

Introduction

The work described in this thesis is concerned with atomic physics on the attosecond ($1\,\mathrm{as} = 10^{-18}\,\mathrm{s}$) timescale. One of the earliest quantum mechanical theories was the Bohr model of the atom, in which the atom consisted of a nucleus surrounded by electrons. In this model the electrons orbit the nucleus at distances r for which the Coulomb force is compensated for by the centripetal force. In the case of a single electron orbiting around a singly charged nucleus the orbits must obey:

$$\frac{m_e v_e^2}{r} = \frac{e^2}{4\pi\epsilon_0 r^2}, \tag{1.1}$$

where ϵ_0 denotes the permittivity of vacuum and m_e, e, and v_e represent the electron mass, charge and velocity, respectively. The second assumption of the Bohr model is that only a discrete set of allowed orbits exists, and that the angular momentum of these orbits can be quantized in terms of the reduced Planck constant, $\hbar$, as:

$$m_e v_e r = n\hbar, \tag{1.2}$$

where n is an integer number. The radius of the ground state, where $n = 1$, is called the Bohr radius, and is given by $a_0 = 5.3 \cdot 10^{-11}\,\mathrm{m}$. It follows that the period of this orbit is given by

$$T_B = 2\pi \left(a_0^2 m_e/\hbar\right) \equiv 2\pi t_a \equiv 150\ \mathrm{as}, \tag{1.3}$$

where t_a is the atomic unit of time.

Although the Bohr model has been superseded by the probabilistic quantum mechanical theories, the quantization part is still valid. Additionally, the model gives an intuitive picture of the timescale of the electron dynamics in atoms. Attosecond science deals with dynamic processes on this timescale inside atoms, molecules and solids [1–8].

Scientists have long been pondering and discussing what happens on timescales shorter than that observable by the technology available at the time. In the nineteenth century the movement of fast-running mammals was debated. The advent of fast shutter mechanisms for cameras [9] provided answers to these types questions, and would later lead to the development of the motion picture. However, mechanical

shutters are ultimately limited by the speed at which the physical object can move, which *de facto* limits the recording speed to about a tenth of a millisecond. An alternative technique relies on the use of a short light pulse as a gating pulse for image acquisition. When using this technique the object is in a dark environment and the camera shutter constantly open, thus allowing constant exposure of the film. The object is only visible when the light pulse illuminates it, so the picture acquisition time is determined by the duration of the light pulse. If the measurement is repeated with a series of short pulses it is called a stroboscopic measurement, while the apparatus is called a stroboscope. In the earliest stroboscopic experiments the light pulses were delivered by the electrical discharge of a charged capacitor. The use of such an electric discharge is usually called flash photography [10, 11], and allows objects to be illuminated for durations of microseconds (10^{-6} s), or even nanoseconds (10^{-9} s).

It was only with the invention of the laser [12], that timescales shorter than a nanosecond became available. The fastest cameras available today generally rely on femtosecond (1 fs = 10^{-15} s) light pulses delivered by Ti:sapphire based lasers [13]. Figure 1.1 shows relevant timescales for various dynamic processes that can be recorded using appropriate light pulses.

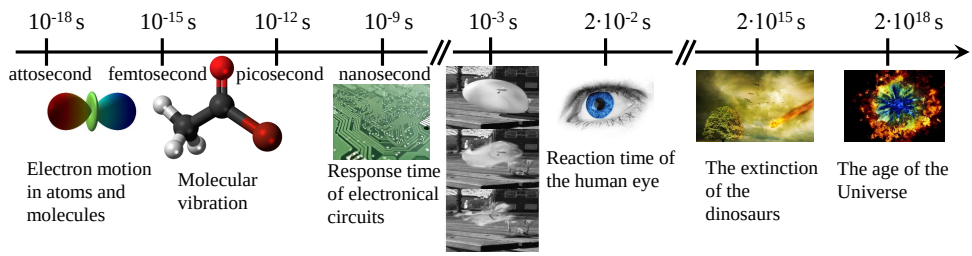

Figure 1.1: Relevant timescales for various processes. (Some of these images were acquired from reference [14]).

1.1 Attosecond Light Pulses

The shortest possible duration of a light pulse is inversely proportional to the spectral bandwidth through the *time–bandwidth* product:

$$\Delta\nu\Delta t \geq K, \tag{1.4}$$

where Δt and $\Delta\nu$ denotes the full-width at half-maximum of the temporal and spectral shape, respectively, and K is a constant that depends on the exact shape of the pulse. For a light pulse with a Gaussian spectral shape $K = 0.441$, while a table of time–bandwidth products for other common pulse shapes can be found in reference [15]. The duration of an electromagnetic pulse is ultimately limited by a single cycle of the carrier frequency of the pulse, which can be expressed in terms of the carrier wavelength, λ, and the speed of light, c, as:

$$\mathrm{T}_{1\mathrm{cyc}} = \lambda/c. \tag{1.5}$$

This shows that in order to obtain a sub-femtosecond duration the carrier wavelength must be shorter than 300 nm, *i.e.,* in the ultraviolet. From Equation (1.4) it is evident

that short pulses require a broadband spectrum. In laser technology broadband spectra capable of providing short pulses are usually generated by either Q-switching or mode locking [16], where the latter has paved the way for few-cycle laser systems in the optical regime [17]. However, at the present time no attosecond lasers exist. Instead, attosecond pulses are produced using a nonlinear optical technique called high-order harmonic generation (HHG) [18, 19]. HHG involves nonlinear up-conversion of femtosecond near-infrared (NIR) or visible (VIS) pulses delivered by a laser system into the extreme ultraviolet (XUV) or even the X-ray regime. It was proposed already in 1992 that attosecond pulses could be produced through the mechanism of HHG [20], but this was not experimentally validated until 2001 [21, 22]. Using this technique, pulses as short as 67 as have been demonstrated [23]. The widest spectrum ever produced through HHG [24] could, in principle, support pulses with durations down to 2.5 as, however, the duration of the pulse has never been measured. Attosecond pulses produced by HHG can either be produced as a single attosecond pulse (SAP) [22], or as a sequence of closely spaced attosecond pulses known as an attosecond pulse train (APT) [21]. In the spectral domain a SAP corresponds to a XUV supercontinuum, while an APT consists of discrete harmonics of the fundamental laser.

There are numerous other methods of producing XUV and X-ray light, for example, large-scale facilities such as synchrotrons [25, 26] and free-electron lasers [27, 28]. However, since none of these currently are capable of producing attosecond pulses, they will not be discussed in this thesis.

1.2 Aims and Outline of this Thesis

When work began on this thesis project in 2011 the field of attosecond physics was already well established. The first attosecond pulses had been measured more than a decade earlier, and the first experiments with attosecond time resolution were also almost a decade old [1]. The Attosecond Physics Group at Lund University had previously held the record for the shortest pulses produced [29], and had recently demonstrated the capability of extracting photo-ionization time delays from various systems using APTs in interferometric measurements known as reconstruction of attosecond beating by interfering two-photon transitions (RABBITT) [5, 6, 30, 31].

Many of the experiments conducted in the first decade of attosecond physics had poor reproducibility and the sources suffered from instability. In addition, the attosecond sources generally suffered from low tunability in the spectral domain, which limited the measurement of photo-ionization time delays to a few data points using APTs. Furthermore, highly complicated laser systems, which were generally limited to repetition rates of a few kHz, were required to drive harmonics sources, which made coincidence-based experiments such as double-ionization, as presented, for example, by reference [6], very demanding. Figure 1.2 shows an overview of the light sources used in Lund at beginning of the work presented in this thesis, together with an overview of the light sources used by other groups. As apparent from the figure a large variety of light sources existed in the Attosecond community, but not in Lund. Therefore, a large effort in recent years has been to develop the attosecond sources simultaneously with development of the attosecond applications.

The work described in this thesis had three main aims.

- The first was to increase the accessibility of attosecond or HHG sources by

combining the harmonic generation process with more user-friendly laser systems than traditionally used.

- The second was to further develop attosecond sources and interferometers to allow for greater tunability of the harmonic sources and better reproducibility in the measurements.

- The final aim was to increase the repetition rate of the attosecond sources.

This thesis consists of two parts. The second part is a compilation of the ten manuscripts and papers published throughout these doctoral studies, while the first part is meant as a summary of the underlying theoretical and experimental background of the studies presented in these papers. Furthermore, work towards the construction of a quantum stroboscope [32] driven by a frequency tunable short wavelength IR (SIR) source is presented in the first part.

Paper **I** describes the development of a HHG setup for use with high-repetition-rate systems. The HHG setup was combined with a highly reliable commercial laser system as described in the paper. This combination was then used to study differences between different quantum trajectories involved in HHG (Papers **II** and **III**). The HHG setup was also used to study the effects of the carrier-envelope phase (CEP) of few-cycle pulses in HHG (Paper **IV**).

The studies presented in Papers **V**, Paper **VI** and **VII** follow the tradition of studying photo-ionization time delays by the Attosecond Physics Group in Lund using a system with a repetition rate of 1 kHz. Paper **VI** presents a study of macroscopic effects involved in the measurements of attosecond time delays. Paper **V** describes the comparison of photo-ionization time delays for various noble gases, while Paper **VII** describes the use of a tunable laser to study the impact of a narrow-band resonance in two-photon ionization. Paper **VIII** describes the investigations of the possibility of generating SAPs from few-cycle pulses in a non-collinear geometry. Paper **IX** presents investigations into the possibility of controlling the spatial and spectral content of XUV light using of intense IR light by a technique called controlled free induction decay.

Finally, Paper **X** describes the use of an optical parametric amplifier in the NIR to study plasmonic resonances in nanostructures through a surface science tool known as a photo-electron emission microscope. The author's contribution to this study was limited to work on the laser and TOPAS for this experiment, thus the details of the surface science tool are not discussed in this thesis.

Apart from the introduction this thesis consists of six chapters. Chapter 2 starts by giving a basic introduction to nonlinear and ultrafast optics. The second part of the chapter presents the various laser systems used in this work. Chapter 3 introduces the concept of HHG from a theoretical point of view. HHG is described using both a semi-classical model and a quantum mechanical model known as the strong-field-approximation. The chapter continues with a description of the various complexities inherent in HHG, such as the effects of multiple electrons and phase-matching. Chapter 4 presents the experimental attosecond sources developed as part of this work. The chapter additionally outlines the experimental studies of HHG under various conditions. Chapter 5 is devoted to attosecond interferometry, and describes the experimental setups used for pump-probe experiments in this work. Chapter 6 starts by introducing the concept of atomic time delays in photo-ionization, and is

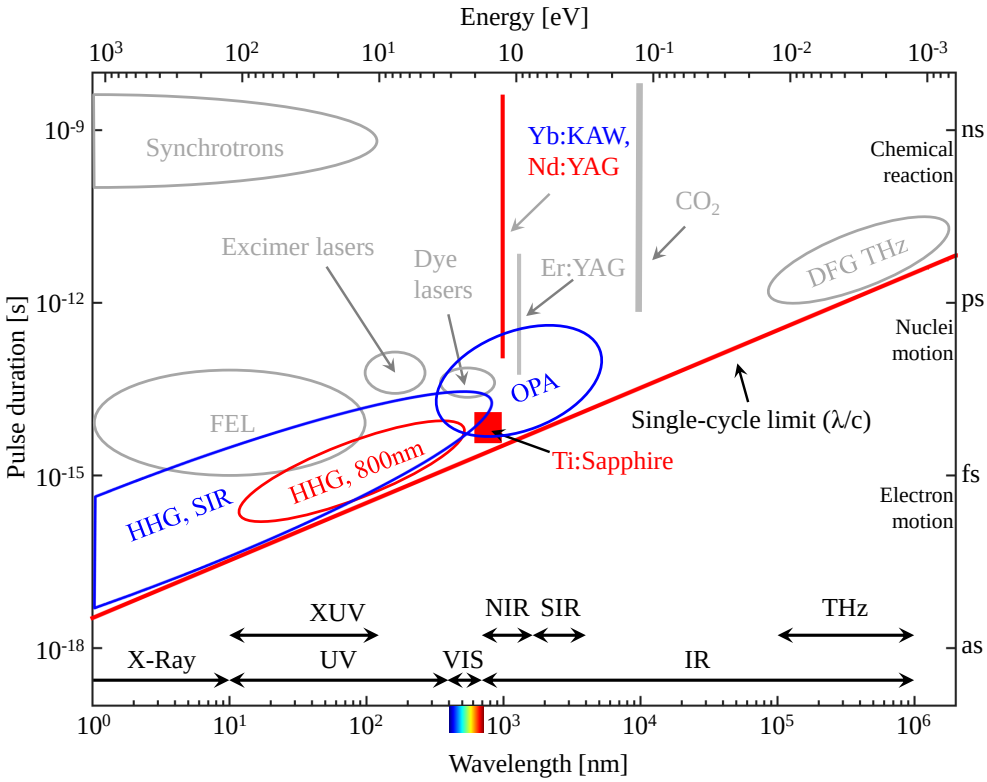

Figure 1.2: Characteristic carrier wavelengths and timescales for the most common ultrashort light sources. The light sources are color-coded as: red, laser-driven light sources used by the Attosecond Physics Group prior to the present work; blue, laser-driven light sources used within the attosecond community, but not in Lund prior to this work; gray, light sources not commonly used for attosecond experiments or those requiring large- scale facilities. IR, infrared; UV, ultraviolet; VIS, visible. NIR, near-infrared; SIR, short-wavelength infrared; XUV, extreme ultraviolet. DFG, difference frequency generation; FEL, free-electron lasers; HHG, high-order harmonic generation; OPA, optical parametric amplification; SAP, single-attosecond pulse.

concluded with a description of free induction decay. Finally, Chapter 7 provides a summary of the thesis and future outlook.

Chapter 2

Ultrashort Pulses and Nonlinear Optics

The purpose of this chapter is to introduce the basic concepts and notation of ultrashort optics used throughout this work. This chapter is structured in the following way. Section 2.1 lays the theoretical groundwork for ultrashort nonlinear optics, while Section 2.2 is provides an overview of the various experimental laser techniques used.

2.1 Fundamentals of Ultrafast Nonlinear Optics

The interaction between light and matter can be described classically by Maxwell's equations together with the Lorentz force. Maxwell's equations relate the electric, $\boldsymbol{\mathcal{E}}(\mathbf{r},t)$, and the magnetic, $\mathbf{B}(\mathbf{r},t)$, fields to the current, $\mathbf{j}(\mathbf{r},t)$, and charge $\rho(\mathbf{r},t)$ densities, while the Lorentz force, $\mathbf{F}(\mathbf{r},t)$, governs the motion of charged particles. The system can be solved using the Newtonian equations of motion. In differential form Maxwell's equations are given by [33]:

$$\nabla\cdot\boldsymbol{\mathcal{E}}(\mathbf{r},t)=\frac{1}{\epsilon_0}\rho(\mathbf{r},t)\equiv\frac{1}{\epsilon_0}\nabla\cdot\mathbf{P}(\mathbf{r},t)\,, \qquad \text{(Gauss' Law)} \qquad (2.1)$$

$$\nabla\cdot\mathbf{B}(\mathbf{r},t)=0, \qquad \text{(Gauss' Law for Magnetism)} \qquad (2.2)$$

$$\nabla\times\boldsymbol{\mathcal{E}}(\mathbf{r},t)=-\frac{\partial}{\partial t}\mathbf{B}(\mathbf{r},t)\,, \qquad \text{(Faraday's Law)} \qquad (2.3)$$

$$\nabla\times\mathbf{B}(\mathbf{r},t)=\frac{1}{c^2}\frac{\partial}{\partial t}\mathcal{E}(\mathbf{r},t)+\frac{1}{\epsilon_0 c^2}\mathbf{j}(\mathbf{r},t)\,. \qquad \text{(Ampere's Law)} \qquad (2.4)$$

The Lorentz force is given by:

$$\mathbf{F}(\mathbf{r},t)=Q\left[\boldsymbol{\mathcal{E}}(\mathbf{r},t)+\mathbf{v}(\mathbf{r},t)\times\mathbf{B}(\mathbf{r},t)\right]. \qquad (2.5)$$

Here $\mathbf{r}$ is the position and t the time, c is the speed of light, which is related to the electric permittivity ϵ_0 and the magnetic permeability μ_0 of the vacuum by $c=1/\sqrt{\mu_0\epsilon_0}$, and Q and $\mathbf{v}$ are the particle charge and velocity, respectively. Finally, $\mathbf{P}(\mathbf{r},t)$ is the dielectric polarization (simply called the polarization), which is a measure

of the density of electric dipoles. Throughout this work slow moving particles were considered, which means that the Lorentz force can be approximated by the Coulomb force $\mathbf{F}(\mathbf{r},t) = Q\boldsymbol{\mathcal{E}}(\mathbf{r},t)$.

The wave equation of the electric field can be derived by taking the curl of Equation (2.3) and then applying Equations (2.1) and (2.4). In a homogeneous isotropic non-magnetic medium, in the absence of free currents and charges, the wave equation takes the form:

$$\nabla^2\boldsymbol{\mathcal{E}}(\mathbf{r},t) - \frac{1}{c^2}\frac{\partial^2}{\partial t^2}\boldsymbol{\mathcal{E}}(\mathbf{r},t) = \mu_0\frac{\partial^2}{\partial t^2}\mathbf{P}(\mathbf{r},t), \tag{2.6}$$

where the polarization current due to the time-variation of the induced dipole moment has been used *i.e.,*

$$\mathbf{j}(\mathbf{r},t) = \frac{\partial}{\partial t}\mathbf{P}(\mathbf{r},t). \tag{2.7}$$

For weak fields, the polarization is linked to the electric field by $P(t) = \epsilon_0\chi^{(1)}\mathcal{E}(t)$, where $\chi^{(1)}$ is the linear electric susceptibility. The refractive index, n, is related to the susceptibility by $n^2 = 1 + \chi^{(1)}$. In most cases, it is reasonable to assume that the electric field is separable in time and space. It can then be shown that in vacuum, where the right-hand side of Equation (2.6) is 0, solutions to the wave equation can be written in Euler representation as:

$$\boldsymbol{\mathcal{E}}(\mathbf{r},t) = \hat{\boldsymbol{\ell}}\mathcal{E}_0(\mathbf{r})A(t)\mathrm{e}^{i(\omega t - \mathbf{k}\cdot\mathbf{r} - \Phi_0)} + \text{c.c.}. \tag{2.8}$$

In Equation (2.8) $\hat{\boldsymbol{\ell}}$ denotes the polarization vector[1], ω the frequency, $\mathbf{k} = (\omega/c)\hat{\mathbf{k}}$ the wave vector, $A(t)$ a temporal envelope function and $\mathcal{E}_0(\mathbf{r})$ a spatial envelope, and Φ_0 denotes a constant phase. Finally, c.c. denotes the complex conjugate of the previous term. Since the field is a real quantity the complex conjugate part of the field carries redundant information and will be omitted in most cases throughout this thesis to simplify the notation. Nevertheless, the full-field representation may be used occasionally for reasons of clarity. The amplitude of the wave vector is conventionally called the wavenumber, and can be written in terms of the refractive index as $|\mathbf{k}| = \frac{\omega}{c}n$.

Using Equation (2.8) the polarization may be expressed as:

$$\mathbf{P}(\mathbf{r},t) = \hat{\boldsymbol{\ell}}_P\epsilon_0\chi^{(1)}\mathcal{E}_0(\mathbf{r})A(t)\mathrm{e}^{i(\omega t - \mathbf{k}\cdot\mathbf{r} - \Phi_0)}, \tag{2.9}$$

where $\hat{\boldsymbol{\ell}}_P$ denotes the polarization vector of the induced polarization field.

If the applied field is of comparable strength to the intra-atomic potential, the medium will start to behave nonlinearly. Nonlinear optics is significantly more complex than linear optics and the polarization may instead be written in terms of the spatial components ($i \in x, y, z$) as a power series of the electric field:

$$\begin{aligned} P_i(t) &= \epsilon_0\left(\sum_j \chi^{(1)}_{ij}\mathcal{E}_j(t) + \sum_{jk}\chi^{(2)}_{ijk}\mathcal{E}_j(t)\mathcal{E}_k(t) + \sum_{jkl}\chi^{(3)}_{ijkl}\mathcal{E}_j(t)\mathcal{E}_k(t)\mathcal{E}_l(t) + \cdots\right) \\ &\equiv P_i^{(1)}(t) + P_i^{(2)}(t) + P_i^{(3)}(t) + \cdots, \end{aligned} \tag{2.10}$$

[1]It is unfortunate that the term polarization refers to both a field and a vector. However, this ambiguity is common and will be used throughout this thesis. Hopefully, the difference will be clear from the context.

where, the sums are taken over the spatial coordinates. It is apparent from the equation above that the different $\chi^{(k)}$ are tensors of rank $k+1$. Analogous with the linear case they are usually called the kth order susceptibility. Likewise, $P_i^{(k)}$ are referred to as the kth order polarization. As the temporal response of the electric susceptibility is generally unknown, it is often helpful to approach the problem in the frequency domain by performing frequency decomposition of both the electric and polarization fields. In the frequency domain (the Fourier domain of time) the wave equation takes the following form:

$$\nabla^2 \boldsymbol{\mathcal{E}}(\mathbf{r},t) + \frac{\omega^2}{c^2}\boldsymbol{\mathcal{E}}(\mathbf{r},t) = -\mu_0\omega^2 \mathbf{P}(\mathbf{r},\omega)\,. \tag{2.11}$$

with

$$\boldsymbol{\mathcal{E}}(\mathbf{r},\omega) = \mathcal{F}_t\{\boldsymbol{\mathcal{E}}(\mathbf{r},t)\} \equiv \int_{-\infty}^{\infty} \boldsymbol{\mathcal{E}}(\mathbf{r},t)\,\mathrm{e}^{-i\omega t}dt, \tag{2.12}$$

$$\mathbf{P}(\mathbf{r},\omega) = \mathcal{F}_t\{\mathbf{P}(\mathbf{r},t)\} \equiv \int_{-\infty}^{\infty} \mathbf{P}(\mathbf{r},t)\,\mathrm{e}^{-i\omega t}dt. \tag{2.13}$$

Using Equation (2.8), the field can be expressed in frequency space as:

$$\boldsymbol{\mathcal{E}}(\mathbf{r},\omega) = \hat{\boldsymbol{\ell}}\mathcal{E}_0(\mathbf{r})\tilde{A}(\omega)\mathrm{e}^{-i\,\phi(\omega)}, \tag{2.14}$$

where $\tilde{A}(\omega)$ and $\phi(\omega)$ are the spectral amplitude and phases. The various orders of polarization in the frequency domain can be calculated by applying the convolution theorem of Fourier transforms[2] an appropriate number of times. For example, in the case of a second-order nonlinearity the convolution theorem should be applied twice, and in the case of a third-order nonlinearity, three times, *etc.* In systems where resonances can be ignored, nonlinear polarization [3] is often computationally easier in the time domain. However, it is sometimes necessary to perform frequency analysis.

Once the polarization and electrical fields have been found in the frequency domain the temporal fields can be found by inverse Fourier transforms, *i.e.,*

$$\boldsymbol{\mathcal{E}}(\mathbf{r},t) = \frac{1}{2\pi}\int_{-\infty}^{\infty} \boldsymbol{\mathcal{E}}(\mathbf{r},\omega)\,\mathrm{e}^{i\omega t}d\omega \equiv \mathcal{F}_t^{-1}\{\boldsymbol{\mathcal{E}}(\mathbf{r},t)\}, \tag{2.15}$$

$$\mathbf{P}(\mathbf{r},t) = \frac{1}{2\pi}\int_{-\infty}^{\infty} \mathbf{P}(\mathbf{r},\omega)\,\mathrm{e}^{i\omega t}d\omega \equiv \mathcal{F}_t^{-1}\{\mathbf{P}(\mathbf{r},\omega)\}. \tag{2.16}$$

2.1.1 Spectral and Temporal Phase

The spectral and temporal phases $[\phi(\omega), \Phi(t)]$ of an ultrashort pulse can both be expressed in terms of Taylor series around either a given time t_0 or a given frequency ω_0

$$\Phi(t) = \underbrace{\Phi(t_0)}_{\Phi_0} + \left.\frac{\partial\Phi}{\partial t}\right|_{t_0}(t-t_0) + \left.\frac{\partial^2\Phi}{\partial t^2}\right|_{t_0}\frac{(t-t_0)^2}{2!} + \left.\frac{\partial^3\Phi}{\partial t^3}\right|_{t_0}\frac{(t-t_0)^3}{3!} + \cdots, \tag{2.17}$$

[2] Let f and g be two functions with the product $f\cdot g$ in real space. Then the convolution theorem states that in Fourier space $\mathcal{F}\{f\cdot g\} = \mathcal{F}\{f\} * \mathcal{F}\{g\}$, where $*$ denotes convolution.

[3] Such as off-resonant second harmonic generation [See Section 2.1.4], or HHG within the strong-field approximation [See Section 3.2.1].

$$\phi(\omega) = \underbrace{\phi(\omega_0)}_{\text{CEP}} + \underbrace{\left.\frac{\partial\phi}{\partial\omega}\right|_{\omega_0}}_{\text{GD}} (\omega-\omega_0) + \underbrace{\left.\frac{\partial^2\phi}{\partial\omega^2}\right|_{\omega_0}}_{\text{GDD}} \frac{(\omega-\omega_0)^2}{2!} + \left.\frac{\partial^3\phi}{\partial\omega^3}\right|_{\omega_0} \frac{(\omega-\omega_0)^3}{3!} + \cdots . \quad (2.18)$$

Focusing on the spectral phase the first term is the absolute phase of the pulse, which is usually referred to as the CEP or the carrier-envelope offset and is shown for a few-cycle pulse in Figure 2.1. The second term describes the group delay (GD) of the pulse. In the time domain the GD corresponds to a linear shift in time. The third term is called the group delay dispersion (GDD). For a symmetric pulse in the spectral domain[4], the GDD results in symmetric broadening of the pulse in the time domain. Higher-order terms may be applicable, depending on the spectral bandwidth and shape of the pulse. For symmetric pulses, even-order terms lead to symmetric broadening in the time domain, while odd-order terms lead to asymmetric broadening. A pulse for which the duration is limited by the time–bandwidth product is called

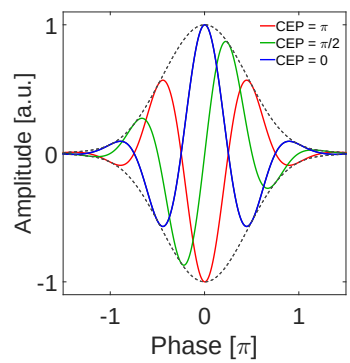

Figure 2.1: Illustration of the CEP of ultrashort pulses.

Fourier-transform-limited or simply transform-limited. If the pulse is longer than the transform-limited duration it is said to be chirped. One usually distinguishes between positive and negative chirp, where positive chirp means that the time derivative of the temporal phase increases with time, while it is negatively chirped if it decreases with time. Figure 2.2 shows how the linear to fourth–order terms of the spectral phase can influence the temporal structure of an ultrashort pulse.

2.1.2 Dispersion of Ultrashort Pulses

When a light pulse impinges on a material, the electrons in the material start to move. The moving electrons constitute new but phase-shifted sources of radiation, which can be described by the polarization density. These radiators are related to the incident field, as they will oscillate with the same frequency. Thus, the total field will be modified by a so-called induced field. The remaining atoms and electrons within the

[4]For which $\mathcal{E}(\omega_0-\omega) = \mathcal{E}(\omega_0+\omega)$, where ω_0 is the central frequency.

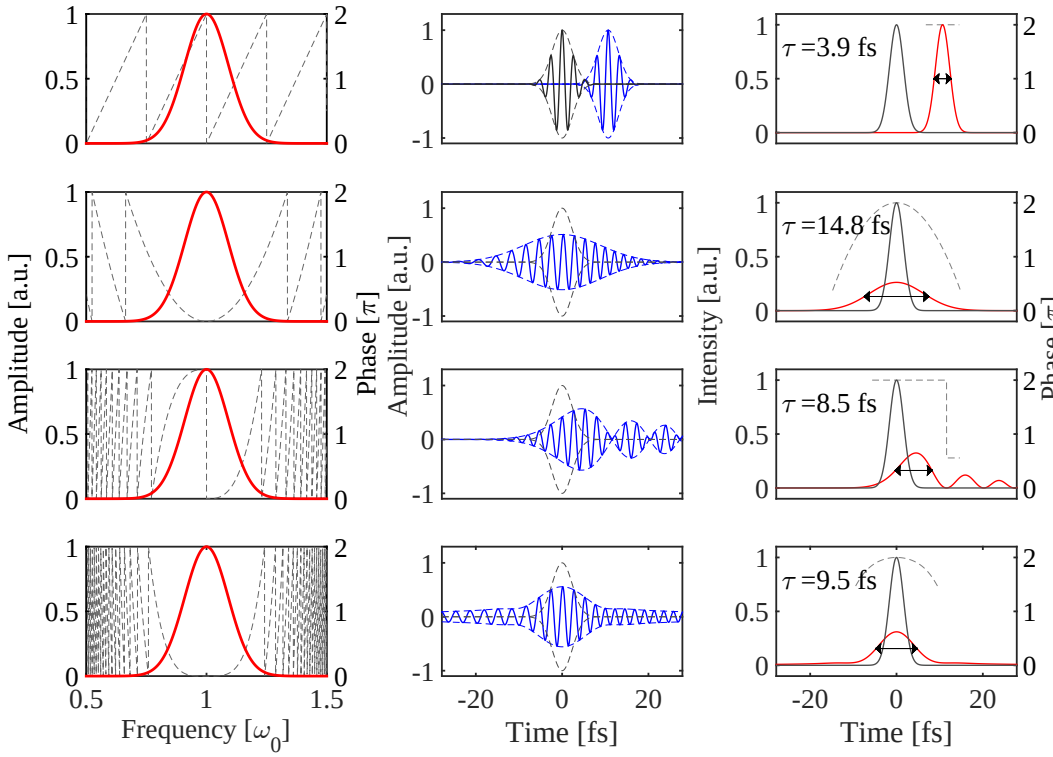

Figure 2.2: The effects of the spectral phase on the time structure of a pulse. The left column shows the spectral amplitude and phase, while the middle column shows the corresponding electric field and envelope in the time domain. The Fourier-transform-limited pulse is shown in gray for comparison. The right column shows the intensity profile of the stretched pulse relative to the transform-limited pulse, and the shift in the temporal phase induced by the nonlinear spectral phase is shown in pale gray.

material will exert a restoration force trying to bring the system back to equilibrium. The result is that, after passing through a glass plate with a thickness of L the electric field will be given by [34]:

$$\mathcal{E}_{\text{out}}(L) = \mathrm{e}^{i\frac{\omega}{c}n_c(\omega)L}\mathcal{E}_0, \tag{2.19}$$

where $n_c(\omega) = n(\omega) + i\alpha(\omega)$ is the complex refractive index. The real part of the refractive index corresponds to the phase shift induced by passing through the material, while the imaginary part corresponds to absorption. Solving the equation of motion for harmonic oscillators yields the complex refractive index in the following form:

$$n_c(\omega) = 1 + \frac{e^2}{2\epsilon_0 m_e}\sum_i \frac{A_i}{\omega_i^2 - \omega^2 + i\gamma_i\omega}, \tag{2.20}$$

where e is the elementary charge, m_e is the electron mass, ω_i may be interpreted as the frequency of the various resonances and A_i is the oscillator strength of these resonances.

Far away from resonances the refractive index is approximately real, and can be rewritten in terms of the wavelength as:

$$n^2(\lambda) = 1 + \sum_i \frac{B_i \lambda^2}{\lambda^2 - \lambda_i^2}. \tag{2.21}$$

The form of the refractive index given Equation (2.21) is normally referred to as a Sellmeier equation. A large web-based database of Sellmeier equations for most materials in the optical to NIR regime can be found in reference [35], while a similar database for refractive index in the XUV regime can be found at in reference [36], which is based on reference [37].

Redefining the wavenumber, k, as the spatial derivative of the phase gives:

$$k = |\mathbf{k}| \equiv \frac{\partial \phi(\omega)}{\partial z} = \frac{\omega}{c} n(\omega), \tag{2.22}$$

which may be Taylor expanded as

$$k(\omega) = k(\omega_0) + \underbrace{\left.\frac{\partial k}{\partial \omega}\right|_{\omega_0}}_{\text{GV}} (\omega - \omega_0) + \underbrace{\left.\frac{\partial^2 k}{\partial \omega^2}\right|_{\omega_0}}_{\text{GVD}} \frac{(\omega - \omega_0)^2}{2!} + \left.\frac{\partial^3 k}{\partial \omega^3}\right|_{\omega_0} \frac{(\omega - \omega_0)^3}{3!} + \cdots, \tag{2.23}$$

where the first term is called the phase velocity of the pulse, the second is the group velocity (GV), and the third term the group velocity dispersion (GVD). A spectral domain where GVD > 0 is called *'normally dispersive'*, while it is called *'anomalous dispersive'* if GVD< 0. It is only in the vicinity of resonances that materials are anomalously dispersive, so the choice of wording stem from the fact that the optical properties of materials were originally investigated in the optical regime, where most materials are normally dispersive, as most resonances are located in either the UV or IR part of the spectrum.

2.1.3 Spatial Properties of Ultrashort Pulses

An ultrashort pulse can generally be described as a paraxial beam propagating along an axis, *i.e.,* a beam where the longitudinal variation of the beam takes place at distances much larger than the wavelength. In such cases it can be shown that (see, for example, reference [16]), the spatial field envelope must satisfy the paraxial Helmholtz equation:

$$\nabla_T^2 \mathcal{E}_0(\mathbf{r}) - i2k \frac{d}{dz} \mathcal{E}_0(\mathbf{r}) = 0, \tag{2.24}$$

where z is the direction of propagation and ∇_T^2 denotes the transverse Laplacian $\left(\frac{d^2}{dx^2} + \frac{d^2}{dy^2}\right)$.

The spatial modes of most lasers can be approximately described by solutions to the paraxial Helmholtz equation known as the Hermite–Gaussian (or simply Gaussian) modes. The longitudinal variation of a Gaussian beam, together with important definitions, is illustrated in Figure 2.3. The lowest-order Gaussian mode is given by:

$$\mathcal{E}_0(\rho, z) = a \frac{w_0}{w(z)} \exp\left(-\frac{\rho^2}{w^2(z)}\right) \exp\left(-i\left[kz + \frac{k\rho^2}{2R(z)} + \Phi_{\text{Gouy}}(z)\right]\right), \tag{2.25}$$

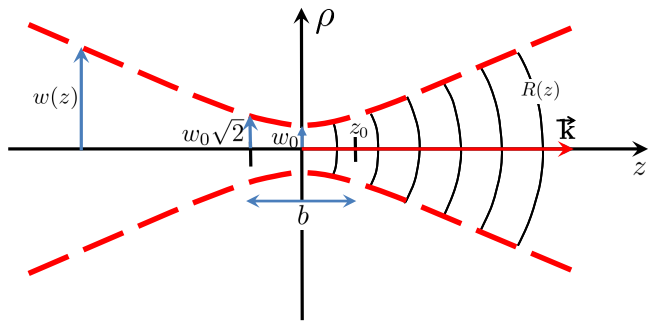

Figure 2.3: Definition of a Gaussian beam.

where

$$R(z) = z\left[1 + \left(\frac{b}{2z}\right)^2\right], w(z) = w_0\sqrt{1 + \left(\frac{2z}{b}\right)^2}, \rho^2 = x^2 + y^2. \tag{2.26}$$

In Equation (2.25) a is the amplitude of the electric field envelope, ρ the radial coordinate, $R(z)$ the radius of wave front curvature, and $w(z)$ is the spot size. The spot size at the focus is called the beam waist and is denoted w_0. The spot size is defined at any given longitudinal position as the transverse distance from the optical axis at which the electrical field (or intensity[5]) has decreased by a factor of $1/e$ ($1/e^2$ for the intensity). The confocal parameter (or depth of focus), b, is considered to be the length of the focus and is given by:

$$b = kw_0^2. \tag{2.27}$$

Half the confocal parameter is called the Rayleigh length z_R.

Finally,

$$\Phi_{\text{Gouy}}(z) = -\arctan\left(\frac{2z}{b}\right) \tag{2.28}$$

is the Gouy phase of the Gaussian beam. The combination of the Gouy phase and the radial phase represents the fact that the beam changes from being spherically converging to spherically diverging as it passes through the focus [38]. The on-axis Gouy phase corresponds to a slow phase shift of $-\pi$ from $z = -\infty$ to $z = \infty$, with the most rapid change occurring close to the focus, where a shift of $-\pi/2$ occurs over the depth of focus.

Fraunhofer diffraction

The propagation of a light pulse as described in Section 2.1 is governed by Maxwell's equations. However, if the electric field distribution in vacuum is known in a plane (x', y', z'), then the corresponding field in any other plane (x, y, z) can be calculated using Kirchhoff's diffraction formalism [39]. The formalism of Kirchhoff is cumbersome and therefore not discussed here. Nevertheless, two limits exist known as Fresnel and

[5] Defined as $I \equiv \frac{c\epsilon_0 n}{2}|\mathcal{E}|^2$.

Fraunhofer diffraction, which significantly simplifies the formalism. Fresnel diffraction describes the changes in the electric field over short distances, where small wave front deformations play important roles, while Fraunhofer diffraction can be used to calculate the change in field distribution over large distances. In practical terms, Fraunhofer diffraction is usually referred to as: being able to calculate the differences between the "near-field" and the "far-field" distribution, where near-field refers to the in-focus distribution, and far-field refers to the distribution far away from a focus. The advantage of Fraunhofer diffraction is two-fold. First and foremost, it reproduces reality well. Secondly, the formalism is computationally simple, since it resembles a Fourier transform for which there are highly optimized computational algorithms. The two-dimensional Fraunhofer diffraction formalism can be written as [40]:

$$\mathcal{E}(x,y,z) = \frac{k}{i2\pi z} e^{-i\left(z+\left\{x^2+y^2\right\}/2z\right)} \int_{-\infty}^{\infty} d\omega_x \int_{-\infty}^{\infty} d\omega_y \mathcal{E}(x',y',0) \mathrm{e}^{i\omega_x + i\omega_x} \tag{2.29}$$

$$\equiv \frac{k}{i2\pi z} e^{-i\left(z+\left\{x^2+y^2\right\}/2z\right)} \mathcal{F}_x \left[\mathcal{F}_y\{\mathcal{E}(x',y',0)\}\right], \tag{2.30}$$

where $\omega_x = k_x x'/z$ and $\omega_y = k_y y'/z$ can be interpreted as spatial frequencies. The diffraction formalisms are derived for monochromatic light, so in the case spatial and temporal pulse structure of a broadband pulse is known in the far-field and information about the near-field structure is desired. One should first perform a frequency decomposition of the pulse, and then use the Fraunhofer diffraction formalism to calculate the near-field distribution of each frequency component. The temporal pulse structure at the focus can then be obtained by an inverse temporal Fourier transform, *i.e.,*

$$\boldsymbol{\mathcal{E}}_{\mathrm{focus}}(x,y,z,t) \propto \mathcal{F}_t^{-1}\left\{\mathcal{F}_{x,y}\left(\mathcal{F}_t\left[\boldsymbol{\mathcal{E}}_{\mathrm{farfield}}(x',y',z',t')\right]\right)\right\}. \tag{2.31}$$

The far-field distribution can be calculated in a similar manner, if the near-field distribution is known. The use of Fourier transforms to link the near-field distribution to the far-field distribution described here, together with the Fourier decomposition between time and frequency described above can be experimentally implemented by the simple use of focusing optics for spatial transforms and gratings for temporal transforms. Although, phase information is lost if all parts of the system perform linearly, as in the case of simple Fourier transforms of linear systems, nonlinear effects can be introduced in one domain or another to extract information about the nonlinear process or pulses. This scheme lies at the heart of nonlinear optics.

2.1.4 Basic Nonlinear Processes

The simplest nonlinear process is second harmonic generation where two photons with the same frequency are converted into a single photon with twice the frequency, *i.e.,* $\omega + \omega = 2\omega$. The process is the result of second-order nonlinear polarization, while the higher-order polarization terms in Equation (2.10) may lead to the production of higher harmonic orders.

Harmonic generation is a special case of sum frequency generation (SFG) between degenerate fields. As the name implies, sum frequency generation takes place when a number of photons with the same or different frequencies ω_i are converted into a single photon with the sum of their frequencies, *i.e.,* $\sum_i \omega_i = \omega$. Difference frequency

generation (DFG) is the counterpart to sum frequency generation. In DFG the resulting photon may have a frequency that is any possible mixture of the frequencies of the input photons. The special case of DFG between nearly degenerate fields is known as optical rectification [41]. As the fields are degenerate, or nearly degenerate, optical rectification creates a very low-frequency field. The most commonly known example of this process is the generation of THz fields in dielectric [42] and metallic media [43], but the technique of CEP stabilization, described in Section 2.2.2, also relies on this.

A type of non-linearity that is important for this work is white light generation (WLG), where a light pulse is spectrally broadened. The most simple form of WLG consists of four-wave-mixing between two degenerate spectral components of the driving pulse with frequency ω. The fields generated will have the frequencies of $\omega + \omega \rightarrow (\omega + \Delta\omega) + (\omega - \Delta\omega)$. WLG can be achieved in two ways, either through plasma formation induced by an intense laser pulse, or through nonlinear motion of the bound electrons, known as self-phase modulation (SPM). SPM leads to symmetric broadening of the pulse, while plasma formation leads to asymmetric broadening skewed towards higher frequencies [44].

The effects of SPM and WLG belong to a group of effects known as self-action effects, since they are nonlinear effects of an ultrashort pulse, imposed on pulse itself through a nonlinear medium. Other types of self-action effects include self-focusing [45, 46], self-steeping [47], and thermal lensing [48].

One usually distinguishes between parametric and nonparametric processes, where a parametric process is a process in which the medium is unaffected after the interaction with the light field, while a nonparametric process refers to a process in which the interaction medium is changed by the process. In other words, a parametric process involves the interaction with virtual levels in the atom, while a nonparametric process involves interaction with real levels in the system (and sometimes also virtual levels).

A special type of DFG is known as optical parametric amplification (OPA) [49]. OPA relies on DFG between an intense high-frequency and a weak low-frequency field and leads to an energy transfer from the intense field to the weak field. During this process, a third field is produced at the difference in frequency between the two input fields. Traditionally, the intense input field is called the pump, the amplified input field is referred to as the signal, while the parasitically generated field is known as the idler [50].

Returning to the DFG process in the case of two collinear beams with frequencies $\omega_1 > \omega_2$ and intensities I_1, I_2, the amount of light generated at $\omega_3 = \omega_1 - \omega_2$ through second-order polarization in a loss-less medium of length L under the un-depleted pump and loose focusing approximations is given by [51]:

$$I_3(L) = \frac{(\chi^{(2)}\omega_3)^2}{2n_1 n_2 n_3 \epsilon_0 c^3} I_1 I_2 L^2 \mathrm{sinc}^2\left(\frac{\Delta k L}{2\pi}\right) \propto I_1 I_2 L^2 \mathrm{sinc}^2\left(\frac{\Delta k L}{2\pi}\right), \tag{2.32}$$

where n_i are the refractive indices at the respective frequencies and Δk is the wave vector mismatch, which ensures momentum conservation, given by:

$$\Delta k = k_1 - k_2 - k_3. \tag{2.33}$$

The quantity $\Delta k L$ is called the phase mismatch, since it is a measurement of the phase difference between the input and output fields. Equation (2.32) is plotted for different wave vector mismatches in Figure 2.4. Two observations can be made in this figure.

(i) If $\Delta k = 0$ the output is maximized and it grows quadratically with L, the process is therefore called phase-matched. (ii) When $\Delta k \neq 0$ the generated signal vanishes at the distance $L_c = \frac{2\pi}{\Delta k}$. L_c is therefore referred to as the coherence length of the process.

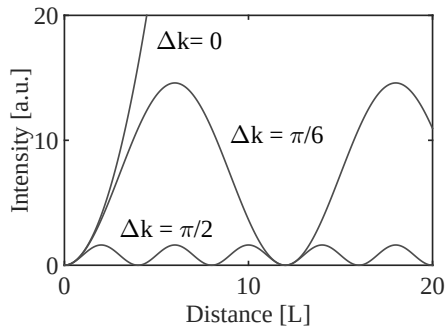

Figure 2.4: Numerical solutions of Equation (2.32).

Phase matching

In principle, all nonlinear processes occur in the medium simultaneously. However, their relative strengths depend on the nonlinear susceptibility tensor and one process can be optimized over the others through the method of phase-matching. Returning to the special case of second-harmonic generation, the wave vector mismatch is given by:

$$\Delta k = 2k(\omega) - k(2\omega) = 2\frac{\omega}{c}n(\omega) - \frac{2\omega}{c}n(2\omega). \tag{2.34}$$

Phase matching is not possible in a medium which is strictly normally dispersive[6](or anomalous dispersive for that matter), hence the generated signal is reduced. One solution is to use a birefringent material, such as beta barium borate (BBO). The refractive index of a birefringent material is dependent on the polarization of the light with respect to the optical axes of the crystal. In the case of beam propagation in a crystal with only one optical axis, light that is polarized perpendicular to the plane containing the wave vector **k**, and the optical axis **o** is called ordinary polarized, while light polarized within this plane is called extraordinary polarized.

The extraordinary polarized light experiences a refractive index n_e, that is dependent on the angle θ between **k** and **o** according to:

$$\frac{1}{n_e^2(\theta)} = \frac{\sin^2\theta}{n_e^2(\theta = 0)} + \frac{\cos^2\theta}{n_o^2}. \tag{2.35}$$

Although the use of birefringent materials allows for phase matching of nonlinear interactions of narrow-band fields, where the phase matching only needs to be fulfilled for one set of frequencies, this is generally not the case for broadband applications.

[6]See Section 2.1.2.

Another complication arises for ultrashort applications known as walk-off. The walk-off effect is due to different group velocities between the pump and signal, and as the pulses have a finite length in space[7], the pulses may not overlap at the end of the crystal if it is too long. Furthermore, in the case of second harmonic generation in a birefringent crystal, as the ordinary axis and the extraordinary axis do not line up the two pulses propagate in slightly different directions, which leads to a angular walk-off.

Both problems can be addressed for certain processes, if the nonlinear interaction is performed with a non-collinear geometry. In the case of DFG between two pulses centered at 800 nm and 400 nm incident on a BBO crystal in a non-collinear geometry with a non-collinear angle of 3.7°, the phase-matching is almost independent of wavelength, and it is therefore possible to achieve very broadband phase matching. Conveniently, this angle almost compensates for spatial walk-off between the pump and signal beams, allowing a very high gain [52, 53]. Both the travelling-wave optical parametric amplifier of superfluorescence (TOPAS), described in Section 2.2.3, and the optical parametric chirped pulse amplification (OPCPA) technique, briefly described in the next section, utilize non-collinear amplification.

2.2 Experimental Techniques for Ultrashort Pulses

In order to perform extreme nonlinear laser physics, intensities around $10^{13-14}\,\mathrm{W/cm^2}$ are needed. The output of an ultrashort oscillator is typically limited to a few nJ, with durations of about 5 fs [17, 54, 55]. In order to reach the intensities required, the oscillator output must either be very tightly focused or the pulses must be amplifed. The most common amplification technique is known as chirped pulse amplification (CPA) and was first applied by D. Strickland and G. Mourou in 1985 [56]. In order to avoid nonlinear effects in the amplification process the ultrashort pulses delivered by an oscillator are chirped to long durations and then amplified using a traditional laser scheme. After amplification the pulses are recompressed to durations close to that of the original pulses. The technique is usually limited by two factors: *(i)* the bandwidth of the system, which usually leads to a minimum recompressed duration of about 30-40 fs, and *(ii)* heating, since amplification relies on traditional laser action. For example, a state-of-the-art Ti:sapphire laser, which operates at 800 nm, is usually pumped by frequency-doubled ytterbium-based lasers at around 515-530 nm. Each pump photon is converted into one signal photon, while the remaining energy is stored in the system in the form of heat. For very high-power applications heating is the limiting factor, which means that such systems have relatively low repetition rates.

The traditional CPA technique has recently been combined with the technique of OPA, resulting in a technique called optical parametric chirped pulse amplification (OPCPA). The OPCPA technique usually utilizes second-order non-linearity together with a chirped seed pulse. By applying the technique in a non-collinear geometry broadband phase matching of the energy transfer from an intense pump beam to the seed beam has become viable.

Parametric processes are instantaneous process in which no energy is stored in the system, thus potentially allowing for higher scalability than traditional laser action, where the gain medium is externally pumped and a light beam is built up slowly, first by spontaneous emission and then by stimulated emission. Some of the most

[7] A duration of 33 fs corresponds to a length of 1 μm at the speed of light in vacuum.

extreme proposed laser systems to date are the European Extreme Light Infrastructure systems [57], which generally rely on parametric amplification schemes. The system used in the study described in Paper **IV** relies on the OPCPA technique.

2.2.1 Laser Systems

Three different laser systems were employed during the course of this work: two based on CPA and one based on OPCPA.

The first CPA-based system is a commercially available Yb:KGW[8] based laser (Pharos, Light Conversion Ltd.), which can deliver 170 fs pulses with a central wavelength of 1030 nm at a tunable repetition rate between 1 and 600 kHz. The system can be operated in two different modes: high pulse energies at a low-repetition-rate (1 kHz), or low pulse energies at a high repetition rate (20-600 kHz). In the low repetition rate mode the average power of the system was limited to 1.5 W, corresponding to 1.5 mJ pulses. In the high-repetition-rate mode the maximal average power scaled linearly with the repetition rate from 3 W at 20 kHz (150 µJ pulses) to 6 W at 100 kHz (60 µJ pulses). At higher repetition rates the system remained limited to an average power of 6 W. This system was used in the studies reported in Papers **I**, **II** and **III**.

The OPCPA system was developed in a collaboration between Lund University and Venteon and is described in detail in reference [58]. The system delivers 10 µJ, 7 fs pulses with a central wavelength around 870 nm, at a repetition rate of 200 kHz. The OPCPA system was used for the experiment described in Paper **IV**. Both the OPCPA system and the Yb:KGW laser were only used as a user for the present work.

The main part of the experimental work was conducted with the second CPA system. The system is located in the Attosecond Laboratory at Lund University and is depicted in Figure 2.5. The system was thoroughly upgraded by Amplitude Technologies during the first six months of this work. In its present form the system consists of a Ti:sapphire oscillator (Rainbow v1, Femtolaser), which, at a repetition rate of 78 MHz, delivers 2 nJ pulses with 800 nm carrier-wavelength and duration <7 fs (corresponding to a spectral width of >300 nm). The pulses are spectrally reduced to 100 nm by external dielectric mirrors, and subsequently stretched to 400 ps using an Öffner triplet type grating stretcher [59]. After stretching, the pulses pass through an acousto-optic programmable dispersive filter (Dazzler, from Fastlite). The Dazzler consists of a birefringent crystal combined with a programmable radio-frequency generator. The Dazzler makes use of the acousto-optic effect (see, for example, [16]). An acoustic wave is sent into the crystal creating a transient grating from which the light pulses from the laser are diffracted. The first-order diffraction is sent for amplification.

The pulses are then pre-amplified to about 250 nJ in a 4-pass ring amplifier before being sent to a regenerative amplifier. The in-coupling to the regenerative amplifier is performed by two Pockels cells, one intra-cavity and one extra-cavity. These Pockels cells reduce the repetition rate to 1 kHz. The regenerative amplifier amplifies the pulses to 0.5 mJ over 13 round trips. An additional Dazzler[9] is placed inside the cavity. The zeroth-order diffraction of this Dazzler corresponds to the beam path of the cavity. The purpose of the second Dazzler will be explained later in this section.

[8] Ytterbium doped potassium gadolinium tungstate crystal.

[9] This Dazzler is usually referred to as a Mazzler, but a Mazzler and a Dazzler differ only in name and usage.

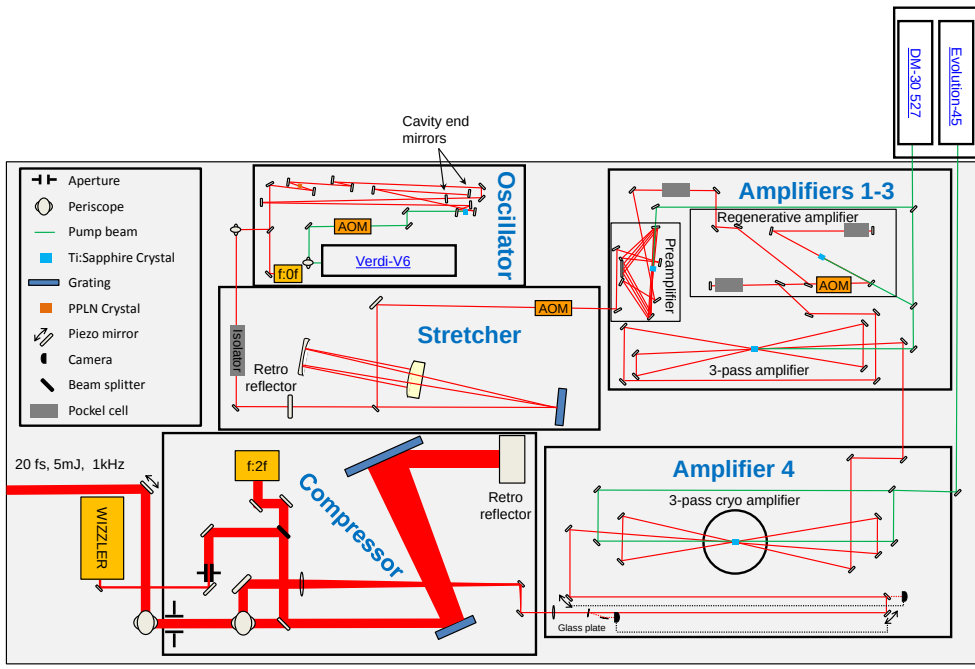

Figure 2.5: A schematic overview of the laser system in the Attosecond Laboratory. The output of the system is 20 fs, 5 mJ pulses at a repetition rate of 1 kHz. Further details of the system can be found in the text.

After leaving the regenerative amplifier the pulses are finally amplified in two 3-pass bow-tie-shaped amplifiers. The second bow-tie amplifier is cryogenically cooled to 123 K to minimize the effects of thermal lensing [60, 61]. The pulse energies after the last two amplifiers are 3 mJ and 10 mJ, respectively. All the amplification stages are pumped at 527 nm using Ti:sapphire crystals as the gain material. The first three amplification stages share a 30 W frequency-doubled Nd:YLF (neodymium-doped yttrium lithium fluoride) laser from Photonics Industries (DM 30-527), while the cryogenically cooled stage is pumped by a 30 W frequency-doubled Nd:YLF laser from Coherent (Evolution–45).

After amplification the pulses are compressed in a grating compressor, resulting in 5 mJ pulses with a near-transform-limited duration of 20 fs, characterized by a commercial pulse-characterization device called a Wizzler from Fastlite [62]. The unconventional short, and near-transform-limited, duration for an amplified Ti:sapphire laser pulse is obtained by combined effort of the two Dazzlers and the Wizzler. As the first Dazzler uses the diffracted beam of a pulse, both the spectral phase and the amplitude can be addressed using this Dazzler. This allows for pre-compensation of the high-order chirp that is accumulated in the amplifier chain, which cannot be compensated for by the grating compressor. The second Dazzler, which is placed inside the regenerative amplifier, counteracts the inherent effect of gain-narrowing in amplifiers (see, for example, reference [63]), by selectively introducing losses into the spectral components with the highest gain in the Ti:sapphire crystal. The Wizzler utilizes a

third-order non-linearity known as cross-polarized wave generation, and combines it with an in-line-generated pulse replica. Overlapping these two pulses in a spectrometer will create a spectral interference signal, which can be used to extract the spectral phase of the original pulse. The extracted phase is then compared to the phase of a transform-limited pulse, creating an error signal that is fed back to the extra-cavity Dazzler, which allows iterative removal of the chirp.

2.2.2 CEP Stabilization

Controlling the CEP of an ultrashort pulse is key in reproducibly controlling electron dynamics on the attosecond timescale by light. CEP stabilization of ultrashort pulses was first proposed and demonstrated in 1999 [64, 65]. There are a number of methods for stabilizing and controlling the CEP of ultrashort pulses exist [50, 64–68]. These can be divided into two categories. The first category of CEP stabilization consists of active stabilization of the entire laser chain [69], while the second category consists of using OPA between two phase-locked fields with different frequencies. The idler beam, which is produced in the OPA process[10], is independent of the carrier envelope offset frequency of the two input fields, provided the signal and pump beams originate from the same source [50, 66, 68]. The latter type of CEP stabilization eliminates the need for active stabilization of the entire laser chain as phase noise is not transferred to the idler [50].

The 1 kHz laser system described in the previous section utilizes both methods, allowing CEP-stable pulses to be obtained from both the direct output of the laser at 800 nm and in the short-wavelength IR (SIR) regime between 1600 and 2500 nm. Combining the two methods the CEP stability of the OPA can be extended to also include the signal beam, which contains the spectral range of 1140 to 1600 nm. Neither the CEP stability of the signal or the idler beam from the OPA were verified in this work. However, the stability of the HHG light[11] produced by the signal beam of the OPA showed a strong correlation with CEP locking of the pump laser for the OPA. The HHG light was significantly more stable, whenever the CEP was locked, leading us to believe that the CEP of the signal was also CEP locked, which in turn means that the idler also must have been CEP locked. Coherent combination of multiple phase-locked outputs of an OPA have recently been used by the group of Baltuška to control and optimize HHG [70].

The direct output of the 1 kHz laser system is actively CEP stabilized by two stages, the details of which can be found in reference [69], but briefly outlined in the following. The CEP drift of the oscillator is measured by an in-line f-to-0f interferometer relying on simultaneous WLG and DFG in a magnesium-oxide doped periodically poled lithium niobate (PPNL) crystal [67]. The process of WLG leads to an octave spanning frequency comb of the fundamental seed pulse, while DFG creates a red-shifted frequency comb. These two frequency combs spectrally overlap in the IR, but with a small offset in frequency for the different parts of the comb. Beating between these two spectral occurs at frequencies corresponding to the repetition rate of the laser, f_{Rep}, an offset frequency, known as the carrier-envelope frequency f_{CEO}, and at the sum and difference frequencies between these two low-frequency fields. The

[10] See Section 2.1.4.
[11] See Chapter 3.

field thus generated can be measured with a photo diode and analyzed with a spectrum analyzer. Feedback to an acousto-optic modulator (AOM) controlling the pump power of the oscillator the frequency f_{CEO} can be locked, and thereby the CEP phase as illustrated in Figure 2.6. The second stage of the CEP stabilization relies on a f-to-2f interferometer [65] placed inside the compressor box, which monitors the CEP of the amplified pulses. CEP drifts of the amplified pulses are compensated for by an additional feedback to the Dazzler placed after the stretcher.

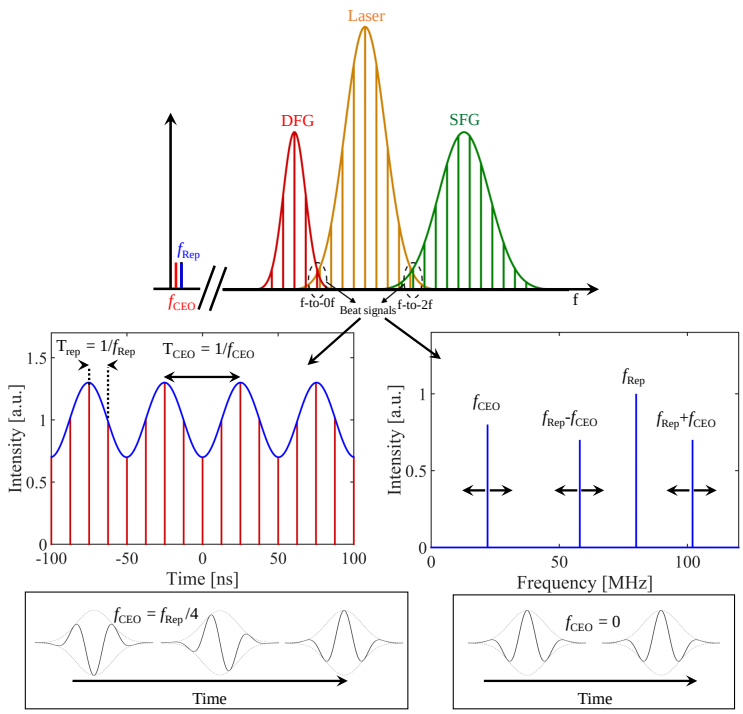

Figure 2.6: Typical CEP stabilization scheme. The top row shows that the frequency comb of the laser and two frequency combs created by DFG and SFG. The laser pulse consists of a frequency comb with frequencies $\mathrm{f}_l = lf_{\mathrm{Rep}} + f_{\mathrm{CEO}}$. A comb generated through SFG will contain frequencies with $\mathrm{f}_m = mf_{\mathrm{Rep}} + 2f_{\mathrm{CEO}}$, while a comb generated through DFG will contain frequencies of $\mathrm{f}_n = nf_{\mathrm{Rep}}$. If the laser spectrum is broad enough the frequency combs will spectrally overlap, and a beat signal can recorded by a photo diode placed behind a narrowband filter. The middle row shows the beat signal in the time domain (left) and in the frequency domain (right). Generally, the carrier-envelope frequency drifts in time, however, this drift can be compensated by an appropriate feedback loop. The bottom row shows a train of few-cycle pulses for which the carrier-envelope frequency is locked to a quarter of the repetition rate (left) and 0 Hz (right). When the carrier-envelope frequency is locked to a fraction $1/q$ of the repetition rate of the laser a CEP shift of $2\pi/q$ between the sequential pulses are obtained, while every pulse is identical if the carrier-envelope frequency is locked to 0 Hz. The carrier-envelope frequency of the laser system described in the text is locked to a quarter of the repetition rate, however, this is not a problem as the amplifier chain operate at 1 kHz.

2.2.3 Travelling-wave Optical Parametric Amplifier of Superfluorescence

The 1 kHz laser system described in Section 2.2.1 was used during this work to pump a commercial OPA, known as a high-energy travelling-wave optical parametric amplifier of superfluorescence (TOPAS). The TOPAS relies on second-order DFG of a high-frequency photon ω_p resulting in two lower frequency photons ω_S, ω_I, where energy conservations requires that $\omega_p = \omega_S + \omega_I$. The three output fields of the TOPAS are referred to as the depleted pump, the signal and the idler.

A schematic of the TOPAS layout is presented in Figure 2.7. The ultrashort pulses delivered by the laser system are split into 4 parts by sequentially placed beam splitters at the beginning of the TOPAS. The least intense pulse is used to generate white light by tightly focusing it into a fused silica plate, resulting in the generation of broadband seed pulses. The seed pulse is chirped to durations of several ps by transmission through a high-GDD glass plate, and subsequently refocused into a BBO crystal, where it acts as a seed for a non-collinear optical parametric amplifier (NC-OPA) with type 2 phase matching[12]. The pump pulse for the NC-OPA is the second weakest pulse, which is also focused into the crystal. The pump pulse is only slightly chirped to around 40 fs.

Since the two pulses have significantly different durations amplification occurs only for the spectral components of the seed pulse that temporally overlap with the pump pulse. The desired amplification spectrum can be adjusted by changing the delay between the two pulses. Furthermore, the crystal is mounted on a rotation stage, such that optimal phase matching can be achieved for the tunability range of the pulses. The carrier wavelength of the signal (the amplified seed) can be tuned between 1140 nm and the degeneracy point of the signal and idler at 1600 nm. The exact bandwidth of the signal depends on the carrier wavelength, but at a carrier wavelength of 1300 nm the bandwidth is approximately 100 nm corresponding to a transform limited duration of ≈ 35 fs (or roughly 8 cycles).

As the NC-OPA is seeded, the propagation direction of the seed prior to the crystal is maintained by the signal after the crystal. Similarly, the depleted pump maintains its directionality. However, the idler, generated by this process, will be both spatially and temporally chirped due to the conservation of momentum. This is not a problem as both the idler and the depleted pump are subsequently dumped.

The signal is further amplified in two single pass collinear OPAs, which are pumped by the two remaining parts of the original pump laser. The amplification medium in both collinear OPAs is also BBO. In both cases a co-propagating idler is produced, which is separated from the signal through the use of a time plate[13] after the first amplifier, and by two Brewster reflections after the second amplifier. The final output of the TOPAS corresponds roughly to a signal pulse of 1 mJ at 1300 nm, an idler pulse of 700 µJ at 2100 nm and a depleted pump beam at 800 nm with a pulse energy of 2 mJ.

[12] The pump and the signal use the ordinary axis of the crystal, while the generated idler uses the extraordinary axis. Different types of phase matching can be found elsewhere, for example, in reference [71].

[13] A birefringent crystal with a large difference between the refractive index of the ordinary and extraordinary polarization. Since the signal and idler are perpendicularly polarized, due to the choice of phase matching, the two pulses are separated in time by roughly 1 ps after transmission through the plate.

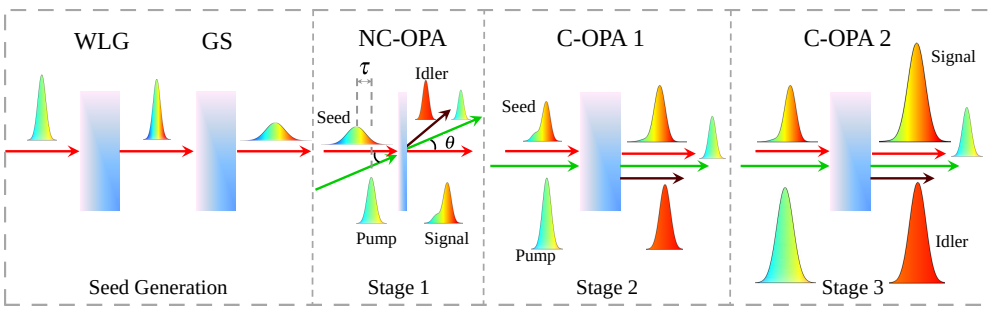

Figure 2.7: Schematic overview of the TOPAS. C-OPA, collinear optical parametric amplifier; GS, glass stretcher; NC-OPA, non-collinear optical parametric amplifier; WLG, white light generation.

Chapter 3

High-Order Harmonics and Attosecond Pulse Generation

The purpose of this chapter is to introduce HHG from a theoretical standpoint. This chapter is structured in the following way. Section 3.1 briefly introduces HHG from a semi-classical point of view known as the three-step model. Section 3.2 develops the explanation of HHG by introducing the quantum mechanical background, which relies on a simplification of the full time-dependent Schrödinger equation known as the strong field approximation (SFA). Section 3.3 introduces the concept of phase-matching in HHG.

3.1 Microscopic Effects of High-order Harmonic Generation

HHG was independently observed by two groups in 1987 [18, 19] when atoms were subjected to strong laser fields. At that time the understanding of nonlinear optics was based on the premises of perturbation theory, in which the efficiency of generating harmonics scales exponentially with the harmonic order, q, *i.e.,*:

$$S_q \propto \frac{1}{q^2}, \tag{3.1}$$

where S_q is the strength of the harmonic signal generated. The first sign that HHG was an entirely new process was indicated by the appearance of a plateau region of equally intense harmonics, as shown in Figure 3.1. It took more than five years to explain the observations, but in the end it was explained by a semi-classical three-step model [72–74]. The three-step model is illustrated schematically in Figure 3.2 (a), and can be described in the following way.

(i) When an atom or a molecule is subjected to a laser field with an intensity greater than $10^{13}\mathrm{W/cm}^2$, one or more electrons may be liberated through the mechanism of tunnel ionization. *(ii)* The liberated electrons will subsequently be accelerated in the combined field of the ion and the laser. *(iii)* Under certain conditions an electron may be driven back to the parent ion after a short excursion, where it may scatter or recombine with the ion. If recombination occurs, an XUV photon is emitted with

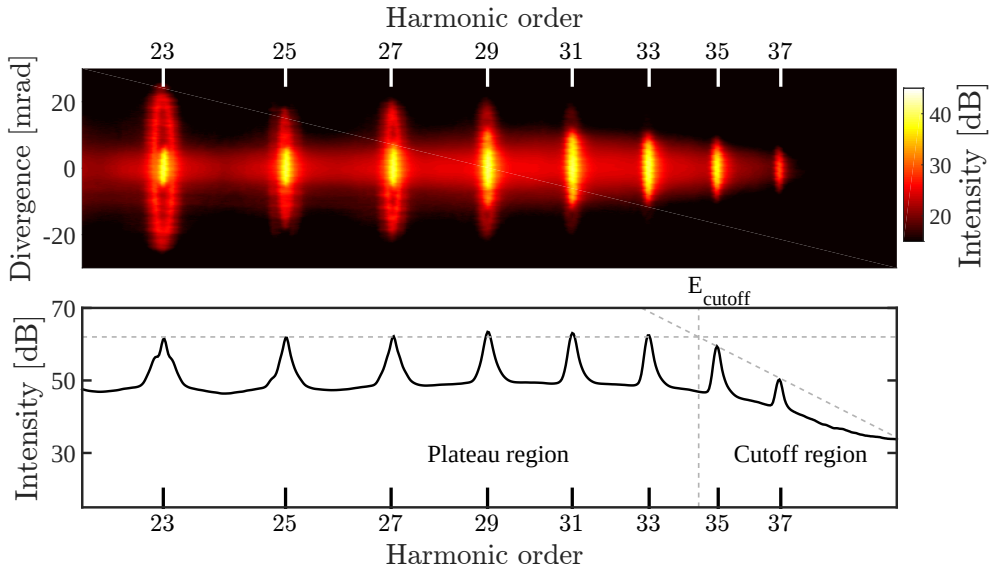

Figure 3.1: Experimental high-order harmonics spectrum generated by a 150 µJ pulse with a carrier wavelength of 1030 nm and a duration of 170 fs. The upper panel shows the spatial and spectral profiles of the harmonics. The lower panel shows the spectrum after spatial integration, which is the typical representation of an HHG spectrum. The cutoff region is indicated. The cutoff energy is defined as the intersection between the plateau region of harmonics with similar strength and the exponentially decaying region.

an energy, E_{XUV}, corresponding to the sum of the kinetic energy of the returning electron, T, and the ionization potential I_p of the system, *i.e.,*

$$E_{\mathrm{XUV}} = T + I_p. \tag{3.2}$$

Within the three-step model ionization is described by tunneling ionization, and recombination occurs if the electron returns to the origin. The position x of a free electron as a function of time t in a linearly polarized electromagnetic field $\mathcal{E}(t) = \mathcal{E}\sin(\omega t)$ with no initial velocity and $x(0) = 0$ can be described by:

$$x(t_i, t) = \frac{e\mathcal{E}}{m\omega^2}\left[\sin(\omega t) - \sin(\omega t_i) - \omega(t - t_i)\cos(\omega t_i)\right], \tag{3.3}$$

where t_i denotes the ionization time. From Equation (3.3) it can be seen that the ionization time is instrumental in deciding whether or not the electron is driven back to the ion. Numerical solutions of the equation can provide a map of ionization times that lead to returning electrons. This can be used to compute the velocity of the returning electrons, and thus their kinetic energy. It can be shown that a multitude of electron trajectories return with similar energies after different excursion times, t_{exc}. These trajectories may be separated into different sets, where the first two sets of trajectories of returning electron are known as the long and the short trajectories,

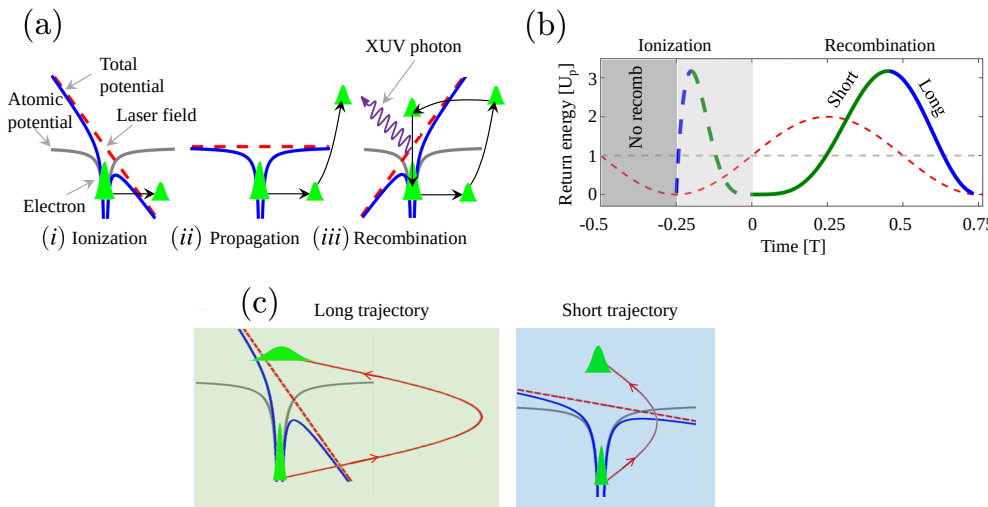

Figure 3.2: (a) Illustration of the three-step model of HHG. (b) and (c) show illustrations of the similarities and differences between the long and short sets of trajectories. (b) The long trajectories are ionized near the peak of the field, and return after an excursion time of almost a cycle. In contrast, the short trajectories are ionized close to the sign change of the field, and return after a shorter excursion time. (c) The maximal spatial displacement from the ion is larger for the long trajectories than the short. In addition, the electron wave packet at the point of return is larger for the long than the short trajectories.

whose excursion times are given by [75]:

$$\begin{aligned} 0\ \mathrm{T} \leq & t_{\mathrm{exc}} \leq 0.65\ \mathrm{T} && \{\text{Short trajectories}\}\ , \\ 0.65\ \mathrm{T} \leq & t_{\mathrm{exc}} \leq\ \mathrm{T} && \{\text{Long trajectories}\}\ , \end{aligned} \tag{3.4}$$

where T is the period of the laser cycle. Similarities and differences between the two first sets of trajectories are shown in Figure 3.2 (b) and (c). The cutoff of the plateau region of HHG occurs at an energy corresponding to the sum of the maximal returning electron energy and the ionization potential, *i.e.,* at:

$$E_{\mathrm{cutoff}} = 3.17U_p + I_p, \tag{3.5}$$

where U_p is the Ponderomotive energy, which is the time-averaged (or quiver) energy of an electron in electromagnetic field, given by:

$$U_p = \frac{e^2\mathcal{E}^2}{4m_e\omega_0^2} \propto \lambda^2 I. \tag{3.6}$$

Harmonics with energies above the classical cutoff of the returning energies can be described by the quantum mechanical equivalent of the three-step model [76], which is the subject of Section 3.2.

As will be described in Section 3.3 phase-matching effects allow us to favorize one trajectory over the other. In practice this is usually used to select the emission from the short trajectories, since it is well collimated and spectrally narrow and therefore well-suited for generation of attosecond pulses [21, 77].

3.1.1 Attosecond Pulses

Because of symmetry, the HHG process repeats every half-cycle of the laser field, emitting an attosecond pulse each time, as shown for the short trajectories in the upper part of Figure 3.3. In the time domain, the CEP of the sequentially emitted attosecond pulses is π-shifted [78]. This π-shift originates from the π-shift of the driving laser. Each of the individually emitted attosecond pulses corresponds to an XUV supercontinuum [Figure 3.2 (b)] with a specific spectral phase, as shown in the lower part of Figure 3.3. For a multi-cycle pulse, interference between these XUV supercontinua leads to the harmonics in the spectral picture. An analogue to this phenomenon can be obtained from the properties of a Fourier transform. The Fourier transform of a periodic function with a single period is poorly defined, thus the spectrum must be broadband. As the number of periods in the periodic function increases, the Fourier transform becomes better defined. In the limit, where every half-cycle is identical, the spectral picture would consist of a series of Dirac delta functions. In reality, the number of contributing half-cycles is limited by the temporal envelope of the driving laser field, resulting in a finite width of the individual harmonics. Various methods of

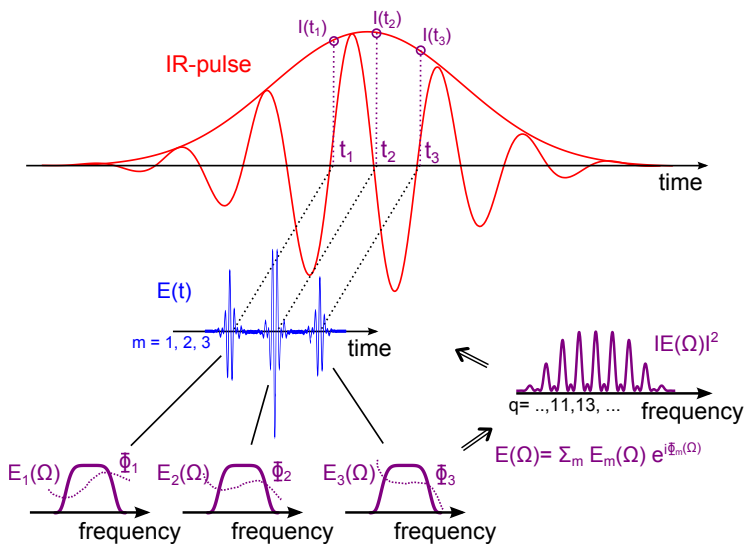

Figure 3.3: Sketch of interference between individual attosecond pulses driven by a few–cycle field. This illustration was taken from Paper **IV**.

experimentally measuring the phase of the XUV field through cross-correlation techniques are discussed in Chapter 6, but it is sufficient here to note that attosecond pulses can be generated as isolated attosecond pulses, referred to as single attosecond pulses (SAPs), or as a series of closely spaced attosecond pulses, *i.e.*, an attosecond pulse train (APT). Generally, APTs are produced by multi-cycle fields, while SAPs can be achieved using fields with near–single-cycle durations.

3.2 The Quantum Description of Light–Matter Interaction

Under the single active electron approximation the Schrödinger equation for an atom in a strong laser field can be written in the length gauge as[1]:

$$[\hat{T} + V(r) + \hat{V}_I(t)]\,|\Psi(t)\rangle = i\hbar\frac{\partial}{\partial t}\,|\Psi(t)\rangle\,, \tag{3.7}$$

where $\hat{T} = -\hat{p}^2\hbar^2/(2m_e)$ is the kinetic energy operator, $V(r)$ is the atomic potential and $\hat{V}_I(t) = e\boldsymbol{\mathcal{E}}(t)\cdot\hat{\mathbf{r}}$ is the dipole operator, which, in the case of linear polarization, takes the form $\hat{V}_I(t) = e\mathcal{E}(t)\hat{z}$, where $\mathbf{z}$ is the direction of polarization.

The strong field approximation introduced by Lewenstein and co-workers in reference [76] relies on a number of assumptions [80], which will be described in detail below.

(i) All other bound states apart from the ground state are ignored, so that the basis consists of a bound state and a set of continuum states.

(ii) The continuum states are unaffected by the atomic potential, $V(r)$.

(iii) The ground state is undepleted by the laser and the continuum states do not couple to each other.

3.2.1 The Strong Field Approximation

(i) All other bound states apart from the ground state are ignored, so that the basis consists of a bound state and a set of continuum states.
Thus, we are looking for a wave function of the form:

$$|\Psi(t)\rangle = |\Psi_B(t)\rangle + |\Psi_C(t)\rangle = c_g(t)\mathrm{e}^{-i(I_p/\hbar)t}\,|g\rangle + \int d^3k c_k(t)\mathrm{e}^{i(E_k/\hbar)t}\,|k\rangle, \tag{3.8}$$

where c_i are the time-dependent coefficients, $I_p = \hbar\omega_g$ is the ionization potential of the ground state and, E_k are the energies of the continuum states.
(ii) The continuum states are unaffected by the atomic potential, $V(r)$. Thus, the continuum states must fulfill the reduced Schrödinger equation

$$[\hat{T} + \hat{V}_I(t)]\Psi_k\,(\mathbf{r},t) = i\hbar\frac{\partial}{\partial t}\Psi_k\,(\mathbf{r},t)\,. \tag{3.9}$$

This form of the Schrödinger equation is most readily solved in the velocity gauge, where analytical expressions, known as the Volkov waves, can be derived: [81, 82]

$$\Psi_k\,(\mathbf{r},t) = \frac{1}{(2\pi)^{3/2}}\mathrm{e}^{i[\mathbf{k}\cdot\mathbf{r} + S(\mathbf{k},\mathbf{A},t,t_0)/\hbar]}, \tag{3.10}$$

where $S\,(\mathbf{k},\mathbf{A},t,t_0)$ describes the quasiclassical action [83] given by:

$$S(\mathbf{k},\mathbf{A},t,t_0) = \frac{\hbar^2}{2m_e}\int_{t_0}^{t} dt'\,[\mathbf{k} + e\mathbf{A}(t')/\hbar]^2, \tag{3.11}$$

[1] The Dirac notation is adopted for this thesis. A detailed description of the notation can be found elsewhere, for example, in reference [79].

for which $\mathbf{k}_c = \mathbf{k} + e\mathbf{A}(t')/\hbar$ is the quantum mechanical equivalent of the canonical momentum and $\mathbf{A}(t)$ is the vector potential

$$\mathbf{A}(t') = -\int_{-\infty}^{t'} dt'' \boldsymbol{\mathcal{E}}(t''). \tag{3.12}$$

Before continuing with the quantum mechanical description of the three-step model, we will examine some important consequences of Volkov waves. The instantaneous frequency of the Volkov waves can be intuitively interpreted as:

$$\omega_{\text{inst}} \equiv \frac{\partial \arg(\Psi_k)}{\partial t} = \frac{1}{\hbar}\frac{\partial S}{\partial t} = \frac{1}{\hbar}\frac{\hbar^2 k_c^2}{2m_e} = \frac{T_{c,\text{kin}}(t)}{\hbar}, \tag{3.13}$$

where $T_{\text{c,kin}}$ is the instantaneous kinetic energy.

The laser field induces a phase shift of a Volkov wave given by:

$$\begin{aligned}\Delta\Phi_{\text{Laser}} &= \arg\{\Psi_k\} - \arg\{\Psi_{k,\mathbf{A}=0}\} = \lim_{\substack{t_0\to-\infty \\ t\to\infty}} \frac{1}{\hbar}\left[S(\mathbf{k},\mathbf{A},t,t_0) - S(\mathbf{k},0,t,t_0)\right] \\ &= \frac{\hbar}{2m_e}\int_{-\infty}^{\infty} dt' \left[2e\mathbf{A}(t')\cdot\mathbf{k} + (e\mathbf{A}(t')/\hbar)^2\right].\end{aligned} \tag{3.14}$$

Under the assumption that the vector potential is linearly polarized along the x-axis, *i.e.,* $\mathbf{A}(t) = (\mathcal{E}_0 a\{t/\tau\}\cos(\omega t), 0, 0)$, we have that the laser pulse is given by $\mathcal{E}(t) = \mathcal{E}_0 a\{t/\tau\}\sin(\omega t)$, where $a\{t/\tau\}$ is a slowly varying envelope function. Following this assumption, one can observe that when averaged over one optical cycle [for which $a\{t/\tau\} \approx a(t_0)$] the first term in Equation (3.14) vanishes and the second term leads to a phase shift of

$$\begin{aligned}\Delta\Phi_{U_p} &= \frac{e^2}{2\hbar m_e}\int_{\text{cycle}} dt' \mathbf{A}(t')^2 \approx a^2(t_0)\frac{e^2\mathcal{E}_0^2}{2\omega^2\hbar m_e}\left[\frac{t}{2} + \frac{\sin(\omega t)}{4\omega}\right]_{-\text{T}/2+t_0}^{\text{T}/2+t_0} \\ &= a^2(t_0)\frac{e^2\mathcal{E}_0^2}{4\omega^2\hbar m_e}\left(1 + \frac{\sin(2\omega t_0)}{4\pi}\right)\text{T} \equiv \frac{U_p(t_0)}{\hbar}\left(1 + \frac{\sin(2\omega t_0)}{4\pi}\right)\text{T},\end{aligned} \tag{3.15}$$

which is known as the Ponderomotive phase shift. As the ground state energy remains constant in this formulation it follows directly that in this version of the SFA the field introduces a phase shift between the ground state and the continuum states given by Equation (3.15). This result is essential for the understanding of the study described in Paper **IX**, in which it was assumed that the highly excited inner valence shell electrons experience a phase shift relative to the ground state corresponding to the Ponderomotive phase shift. The results of Paper **IX** are discussed in more detail in Chapter 6.

(iii) The ground state is undepleted by the laser and the continuum states do not couple to each other, i.e.:

$$c_g(t) \approx 1, \qquad \langle k|\hat{H}_I|k'\rangle = 0, \tag{3.16}$$

where $\hat{H}_I$ is any arbitrary interaction Hamiltonian. It follows from Equation (3.16) that the continuum states are weakly populated and that their coefficients can be approximated using first-order, time-dependent perturbation theory [79, 80]:

$$c_k(t) = \frac{1}{i\hbar}\int_{-\infty}^{t} \langle k_c(t')|\hat{V}_I|g(t')\rangle\, dt', \tag{3.17}$$

where $\langle k_c|$ is a canonical momentum basis function for the system. This approximation is valid if the reason for using SFA is to calculate harmonic spectra in the plateau and cutoff regions. However, in the case of rescattering processes or harmonic spectra near the threshold the where interaction with the ion significantly affects the continuum states a more sophisticated formalism is required for the continuum states.

Using $\hat{V}_I(t') = e\boldsymbol{\mathcal{E}}(t')\hat{\mathbf{r}} = e\mathcal{E}(t')\hat{z}$ the coefficients can be written explicitly as:

$$c_k(t) = \frac{1}{i\hbar}\int_{-\infty}^{t} dt' \mathrm{e}^{-i\frac{S}{\hbar}t'} e\mathcal{E}(t')\,\langle k_c(t')|\hat{z}|g\rangle\,\mathrm{e}^{-i\frac{I_p}{\hbar}t'}. \tag{3.18}$$

We are now fully equipped to write the wave function for the full Schrödinger equation under the SFA, by applying Equations (3.8), (3.10), (3.16) and (3.18).

$$|\Psi(t)\rangle = \mathrm{e}^{-i(I_p/\hbar)t}\,|g\rangle + \frac{e}{i\hbar}\int d^3k \int_{-\infty}^{t} dt' \mathrm{e}^{-i\frac{S+I_p}{\hbar}t'}\,\mathcal{E}(t')\,\langle k_c(t')|\hat{z}|g\rangle\,|k_c(t)\rangle. \tag{3.19}$$

The polarization of a medium was in Chapter 2 defined as the field that describes the density of electric dipoles. On a microscopic level, the polarizability is defined as the expectation value of the operator of the atomic or molecular system. Using these two definitions allows the polarization to be expressed in terms of the microscopic polarizability $\langle\hat{z}\rangle$ of the material:

$$P(t) = \rho_d\,\langle\hat{z}\rangle \equiv \rho_d\,\langle\Psi(t)|\hat{z}|\Psi(t)\rangle\,, \tag{3.20}$$

where ρ_d denotes the number density of microscopic dipoles and Ψ is the wave function.

According to Equation (2.13) the harmonic spectrum can be calculated as

$$\begin{aligned} P(\omega) &= \mathcal{F}_t\{P(t)\} \propto \mathcal{F}_t\{\langle\Psi(t)|\hat{z}|\Psi(t)\rangle\} \\ &= \mathcal{F}_t\{\langle\Psi_B(t)|\hat{z}|\Psi_C(t)\rangle + \langle\Psi_C(t)|\hat{z}|\Psi_B(t)\rangle\}, \end{aligned} \tag{3.21}$$

where continuum–continuum transitions have been omitted as according to assumption *(iii)*.

Writing out Equation (3.21) gives the following expression, which was originally derived in reference [76],

$$P(\omega) = \mathcal{F}_t\left\{\frac{e}{i\hbar}\int_{-\infty}^{t} dt' \int d^3k \overbrace{\mathcal{E}(t')\,\langle k_c(t')|\hat{z}|g\rangle}^{\text{Ionization}} \overbrace{\mathrm{e}^{-\frac{i}{\hbar}\left[S(\mathbf{k},\mathbf{A},t,t')+I_p(t'-t)\right]}}^{\text{Propagation}} \overbrace{\langle g|\hat{z}|k_c(t)\rangle}^{\text{Recombination}} + \text{c.c.}\right\}. \tag{3.22}$$

The various terms of Equation (3.22) have clear physical interpretations, as indicated in the equation. The first term in the integral describes probability of the electron making a transition from the ground state to the excited continuum state in the presence of the driving laser field, at time t', thus creating a coherent wave packet consisting of the ground state and a continuous set of excited states. The second term shows that after ionization, part of the electron travels in the continuum between times t and t', and where it acquires a phase difference relative to the ground state. This phase shift is modified by the instantaneous laser field, thus the evolution happens at the sum of the instantaneous kinetic energy of the excited electron and the binding energy of the bound electron. Finally, at time t the electron wave packet

relaxes back to the ground state and a photon is emitted with the excess energy corresponding to the energy of $E_{\mathrm{XUV}} = I_p + T_{\mathrm{c,kin}}$, where $T_{\mathrm{c,kin}}$ is the instantaneous kinetic energy defined in Equation (3.13). In accordance with the Feynman's path integral formalism the electron in principle takes all paths simultaneously, however, certain pathways contribute more than others to the harmonic spectrum. The pathways with the strongest contributing can be found under the saddle-point approximations, in which the electron returns at to the origin at time t from where it recombines with the ion [76].

3.2.2 Quantum Paths in the Strong Field Approximation

In the saddle-point approximation the solutions to the SFA that result in HHG, correspond to complex times, and it can be shown that the real part of these complex times correspond to the durations of the classical trajectories of the long and short trajectories [83–85]. In the long pulse limit, the time-dependent polarization can be approximated by a discrete set of harmonics of the laser field [85, 86], *i.e.,*

$$P(t) = A(I,t)\exp\left[i\Phi(I,t)\right] \approx \sum_q A_q(I)\exp\left[i\Phi_q(I)\right]\exp\left[iq\omega t\right], \tag{3.23}$$

where $A(I,t)$ and $\Phi(I,t)$ denotes the temporal amplitude and phase, respectively, while $A_q(I)$ and $\Phi_q(I)$ denotes the amplitude and phase of the discrete set, respectively. The spectral phase and amplitude of the harmonics, in Equation (3.23), can be seen as coherent sum of light generated by different trajectories as [85]:

$$A_q(I)\exp\left[i\Phi_q(I)\right] = \sum_{j=\mathrm{traj}} A_q^j(I)\exp\left[i\Phi_q^j(I)\right], \tag{3.24}$$

where A_q^j and Φ_q^j denotes the spectral amplitude and phase of the fields generated by the different trajectories, respectively. Using a Gaussian temporal envelope of the driving laser[2] it is customary to Taylor expand the trajectory dependent dipole phase in terms of the intensity to first order, *i.e.,*

$$\Phi_q^j(I) \approx \Phi_j^q + \left.\frac{\partial\Phi_q^j}{\partial I}\right|_{I_0} I = \Phi_j^q + \alpha_j^q I, \tag{3.25}$$

where α_j^q is known as the trajectory dependent dipole phase and Φ_j^q is a constant phase offset. The trajectory dependent dipole phase of the short trajectories have been studied both theoretically and experimentally for a long time [85, 87], while Paper **III** presents one of the first experimental measurements of the dipole phase of the long trajectories for a broadband energy range. The experiment is further explained in Section 4.3.1.

3.2.3 Electron Correlation Effects

In the previous description of atoms, the single-active-electron approximation was applied. This is of course a simplification. The stationary states of a multi-electron

[2] $I(t) = I_0\exp\left(-t^2/\tau^2\right)$.

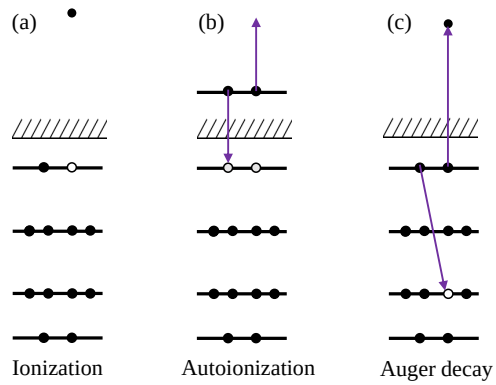

Figure 3.4: Overview of possible effects after the absorption of an XUV photon. (a) A valence shell electron is directly photo-ionized. (b) Two valence shell electrons are simultaneously promoted to a combined bound state above the single-photon ionization energy, which decays through autoionization. (c) A core shell electron is photo-ionized leaving a vacancy in the core, which later becomes occupied by a valence shell electron. A secondary photo-electron is emitted with the excess energy.

system may be represented as a superposition of different electron configuration. These different configurations mix through *configuration interaction* [88].

Configuration interaction leads to phenomena such as autoionization and Auger decay [89]. When an atom is irradiated by an XUV photon with an energy higher than the single electron ionization potential, the atom may be directly ionized, or one or more electrons may be promoted to a (joint) bound state (See Figure 3.4), which may decay through the emission of an electron or the re-emission of an XUV photon. When an electron is emitted after excitation to a bound state, the system is said to have autoionized. Various implications of electron configuration were studied in this work, and are presented in Papers **II**, **VII** and **IX**.

Fano resonances

A Fano resonance describes photo-ionization through the configuration interaction between an excited bound state and a continuum of photo-ionized states [90]. The bound state is embedded in the continuum yielding direct and indirect photo-ionization pathways as depicted in Figure 3.5 (a). The formalism for a Fano resonance will be briefly outlined below, using the notation of Fano. The full formalism can be found in the original work [90]. Mathematically the wave function for the system can be written:

$$|\Psi_E\rangle = a\,|\psi\rangle + \int dE' b_{E'}\,|\psi_{E'}\rangle, \tag{3.26}$$

where $|\psi\rangle$ describes the bound state with amplitude a, and $|\psi_{E'}\rangle$ the continuum states with amplitudes $b_{E'}$. The amplitudes can be found by applying the time-independent Schrödinger equation, $E\,|\Psi_E\rangle = H\,|\Psi_E\rangle$, and expanding the system on the basis

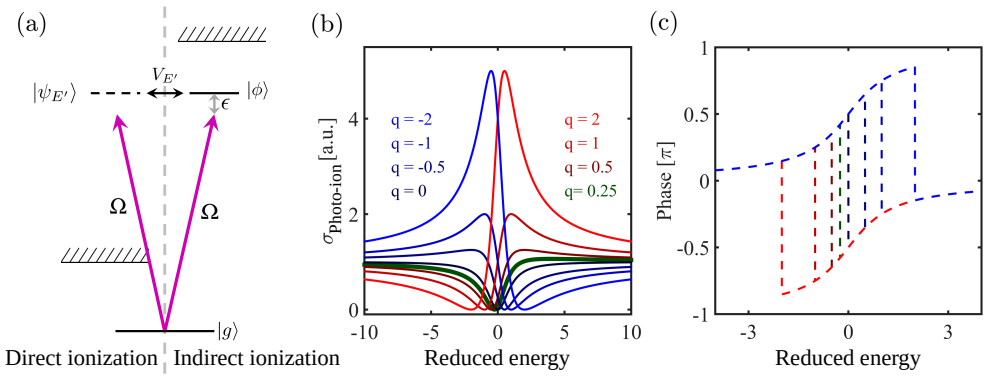

Figure 3.5: Overview of the concept and consequences of a Fano resonance. (a) Energy diagram of a Fano resonace. (b) Relative photo-ionization cross-section shift as a function of E and q (See text for details). (c) Phase shift as a function of E and q the color code is similar to (b).

formed by $\langle\psi|$, $\langle\psi_{E'}|$. This yields a set of equations for the amplitudes:

$$E_\phi a + \int dE' V^*_{E'} b_{E'} = Ea, \tag{3.27}$$

$$V_{E'} a + E' b_{E'} = E b_{E'}, \tag{3.28}$$

where $V_{E'}$ denotes the configuration interaction and E_ϕ the discrete energy level. The solution for the continuum amplitudes [Equation (3.27)] can be written in the form:

$$b_{E'} = \left[\frac{1}{E - E'} - z(E)\delta(E - E')\right] V_{E'} a, \tag{3.29}$$

where $\delta(E - E')$ denotes the Dirac delta function, and $z(E)$ is a real quantity given by:

$$z(E) = \frac{E - E_\phi - F(E)}{|V_E|^2}, \tag{3.30}$$

where $F(E)$ is the *principal part (P)* of the continuum energy integral over the singularity represented by the bound state, *i.e.*,

$$F(E) = P \int dE' \frac{|V_{E'}|^2}{E - E'}. \tag{3.31}$$

Using Equation (3.29) together with the ortho-normalization criterion gives the total wave function:

$$|\Psi_E\rangle = \frac{1}{\pi V^*_E} \sin(\Delta) |\Phi\rangle - \cos(\Delta) |\psi_E\rangle, \tag{3.32}$$

where $|\Phi\rangle$ is an admixture state generated by mixing the bound state with the continuum states, *i.e.*,

$$|\Phi\rangle = |\psi\rangle + P \int dE' \frac{V_{E'} |\psi_{E'}\rangle}{E - E'}, \tag{3.33}$$

and, finally, Δ is a phase-shift induced by the configuration interaction:

$$\Delta = -\arctan\left[\pi/z(E)\right]. \tag{3.34}$$

Introducing the reducing energy parameter[3] ϵ, and Fano's asymmetry parameter q, allows the change in photo-ionization cross-section due to the interaction with the bound state to be written:

$$\frac{\sigma_{\text{pert}}}{\sigma_{\text{unpert}}} = \frac{|\langle\Psi_E|T|i\rangle|^2}{|\langle\psi_E|T|i\rangle|^2} = \frac{(q+\epsilon)^2}{\epsilon^2+1}, \tag{3.35}$$

where T is the dipole transition operator, σ_{unpert} is the cross-section without the bound state, and σ_{pert} is the cross-section with the bound state. In Equation (3.35) the reduced energy is defined as:

$$\epsilon = \frac{E - E_\phi - F(E)}{\pi|V_E|^2}, \tag{3.36}$$

and the parameter q is given by

$$q = \frac{\langle\Phi|T|i\rangle}{\pi V_E^* \langle\psi_E|T|i\rangle}. \tag{3.37}$$

The relative change in photo-ionization cross-section can be written as a sum of three easily interpretable terms:

$$\frac{\sigma_{\text{pert}}}{\sigma_{\text{unpert}}} = \underbrace{1}_{\text{Continuum}} - \underbrace{\frac{1}{1+\epsilon^2}}_{\text{Lorentzian}} + \underbrace{q\frac{q+2\epsilon}{\epsilon^2+1}}_{\text{Cross term}}, \tag{3.38}$$

The first term can be associated with the direct excitation into the continuum, while the second term describes the Lorentzian lineshape of absorption by a bound state, which does not interact with the continuum, thus preventing photo-ionization. Finally, the third term describes the interaction between the continuum and the excited bound state. The representation in Equation (3.38) highlights the physics which can be extracted from Fano's formalism. If the electron configuration interaction between the two configurations did not exist, the photo-ionization cross-section would merely be reduced by the existence of the bound state in the continuum by the absorption probability of that state. Instead the interference between the two configurations, represented by the cross term, leads to an asymmetric profile.

The complex amplitude of the relative change in the transition matrix element may be written:

$$\frac{\langle\Psi_E|T|i\rangle}{\langle\psi_E|T|i\rangle} = \frac{q+\epsilon}{i+\epsilon}, \tag{3.39}$$

from which the phase shift due to the resonance can be computed:

$$\Delta = -\arg\left\{\frac{q+\epsilon}{i+\epsilon}\right\}. \tag{3.40}$$

[3]Note that in other parts of this thesis ϵ denotes ellipticity. However, in order to keep the notation of Fano, the symbol is different here. For the same reason T will be used to represent the dipole transition operator below.

The relative change in photo-ionization cross-section for Fano resonances with different asymmetry parameters in plotted in Figure 3.5 (b), while the relative phase shift is plotted in (c). The Fano profiles were studied in three different ways in the present work. The way in which an off-resonant Fano resonance could influence high-order harmonic generation from different trajectories through the AC Stark effect is reported in Paper **II**. This experiment is explained in more detail in Section 4.3.3. Measurements of the phase shift caused by a Fano resonance in two-photon ionization are described in Paper **VII**, providing the first published phase-measurement of a Fano resonance. The details of this experiment are described in Section 6.1.2. Finally, a phenomenon known as free induction decay was studied in the XUV in the vicinity of a Fano resonance (Paper **IX**). In this study, the fact that the probability of the configuration interaction scales with the principle quantum number, n , as n^{-3} was used, while the dipole transition remains constant with respect to n [91]. The decrease of the autoionization probability with n causes relaxation by dipole transition to be dominant path at high n, which allows us to use Fano resonances with high n numbers to control light in the XUV. This concept is further explained in 6.2.2.

3.3 Macroscopic Effects of High-order Harmonic Generation

Until now, HHG has only been described in a single-atom picture. In reality, macroscopic effects play an important role in shaping the spectrum of the macroscopic pulse, as illustrated in Figure 3.6 (a). The two main macroscopic effects are phase matching and re-absorption. In the case of HHG, phase matching takes the form:

$$\Delta k_\Omega \equiv qk(\omega) - k(\Omega) = q\frac{\omega}{c}n(\omega) - \frac{\Omega}{c}n\left(\Omega\right), \tag{3.41}$$

where q is the nonlinear harmonic order for which $q\hbar\omega = \hbar\Omega$ corresponds to the requirement of energy conservation. Approximate expressions for the refractive indices in the XUV can be found in reference [36]. The noble gases of argon, neon, xenon and krypton were used in the present work. The imaginary and real part of their refractive indices are plotted in Figure 3.6 (b) and (c), respectively. It can be seen that the real part of the refractive index is generally smaller than 1 in the XUV region. In contrast, the refractive index is generally larger than 1 in the optical regime[4], which means that the process is poorly phase-matched ($\Delta k > 0$) in a neutral gas. However, phase matching may still be achieved under certain conditions, yielding a strong XUV pulse, due to various corrections to the actual refractive index, which will be described in the following.

3.3.1 First-order Corrections to the Phase Matching

Geometric Phase

As discussed in Section 2.1.3, a Gaussian beam undergoes a rapid phase shift[5] near the focus. This shift occurs for both the driving laser and the generated XUV beam. This purely geometric phase shift leads to modification of the wave vector mismatch

[4]This is not shown here.
[5]Known as the Gouy phase.

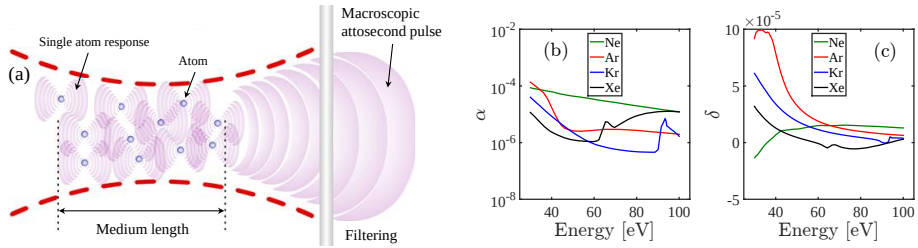

Figure 3.6: (a) Schematic overview of macroscopic effects in HHG. This illustration was adapted from [92]. (b) Imaginary part of the refractive indices in the XUV for xenon, argon, neon and krypton (c) The shift from a refractive index of 1, *i.e.*, $n = 1 - \delta$. The data presented in (b) and (c) are for a pressure of 1 bar and were acquired from reference [36].

of:

$$\Delta k_{\Omega}^{\text{Gouy}} = q\frac{-2/b_{\omega}}{1+\left(\frac{2z}{b_{\omega}}\right)^2} - \frac{-2/b_{\Omega}}{1+\left(\frac{2z}{b_{\Omega}}\right)^2} \approx 2\left(\frac{1}{b_{\Omega}} - \frac{q}{b_{\omega}}\right) \quad \text{for } z \ll \left\{\frac{b_{\omega}}{2}, \frac{b_{\Omega}}{2}\right\}, \tag{3.42}$$

where b_{ω} and b_{Ω} is the depth of focus of the fundamental and harmonic, respectively. As the depth of focus scales linearly with the wave vector [Equation (2.27)] the Gouy phase leads to a negative contribution to the wave vector mismatch near the focus. The contribution to the wave vector mismatch from the Gouy phase decreases outside the focal plane (where $z \neq 0$) as illustrated in Figure 3.7.

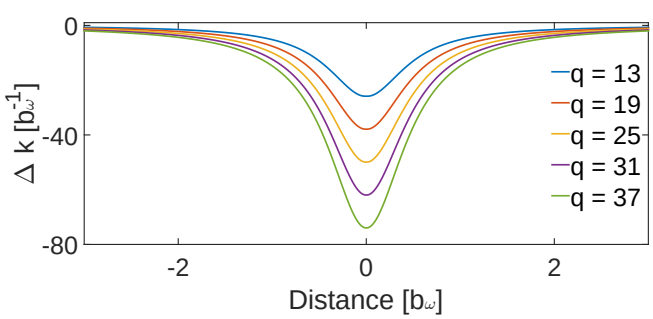

Figure 3.7: Relative wave vector mismatch introduced by the Gouy phase.

Ionization

As the first step of the three-step model relies on ionization the generation medium will inevitably be ionized during the generation process. This results in a number of free charges in the form of ions and free electrons, which causes the electric response of the medium to change towards that of a conducting material. This leads to a decrease in the electric permittivity, and thereby the refractive index. As electrons are much lighter than ions they provide the largest contribution to the conductivity. The decrease in refractive index is greater for lower frequencies than for higher ones, similar to the way in which the Ponderomotive energy depends on the frequency.

For low concentrations of free electrons the plasma induced-dispersion results in a wave vector change of [39]:

$$\Delta k_{\Omega}^{\text{plasma}} = -\frac{q\omega}{c}\frac{\omega_p^2}{2}\left[\frac{1}{n_0\left(\omega\right)\omega^2} - \frac{1}{n_0\left(\Omega\right)\Omega^2}\right] \approx -\frac{q\omega_p^2/\omega}{2cn_0}\left[1-q^{-2}\right], \tag{3.43}$$

where n_0 is the refractive index without free charges and $\omega_p = \sqrt{\rho_e e^2/(2m_e\epsilon_0)}$ is the plasma frequency, where ρ_e is the free electron density. The density of free electrons can be calculated in a suitable manner[6] using the ADK[7] [94, 95] or PPT[8] [96] models, or through full solution of the time-dependent Schrödinger equation. As is apparent from Equation (3.43), the plasma always leads to a negative contribution to the wave vector matching.

Dipole Phase

During the HHG process the electron acquires a nonlinear phase given by Equation (3.25). This phase is transferred to the XUV light during the recombination step of HHG. This shift only affects the harmonics, while the driving laser is unaffected. Derivation of the phase with respect to the propagation direction of the field, shows that the dipole phase leads to wave-vector mismatch given by

$$\Delta k_{\Omega}^{\text{dip,traj}} \approx -\alpha_{\text{traj}}\frac{\partial I(z)}{\partial z} \qquad \begin{cases} < 0 & \text{if } z < 0, \\ > 0 & \text{if } z > 0. \end{cases} \tag{3.44}$$

As indicated above, the sign of the wave vector mismatch depends on whether or not the HHG process occurs before (z < 0) or after (z > 0) the focus. The shift also depends on both the harmonic order, and the trajectory [87] (Paper **III**). The dipole phase constitutes the main contribution to the phase matching, which allows us to select contributions from mainly the short trajectory for studies presented in Papers **I**–**IX** by placing the gas jet after the focal plane of the laser. In order to the study the long trajectories in Papers **II** and **III**, the gas jet is placed at the focus, where both trajectories can be fairly well phase-matched.

Pressure Dependence

The empirical Sellmeier equations for the refractive index n_0 are generally acquired for a specific combination of pressure and temperature, p_0 and T_0. The refractive

[6] Reference [93] provides a good overview of the validity range of various models.
[7] Ammosov–Delone–Kraĭnov.
[8] Perelomov–Popov–Terent'ev.

index can then be determined at other pressures. The refractive index was originally defined as $n^2 = 1 + \chi$, where χ denotes the susceptibility, which is proportional to the number density of atoms, N_a. In an ideal gas the number density is given by:

$$N_a = \frac{p}{k_b T}, \tag{3.45}$$

where T the temperature, p is the pressure, and k_b is the Boltzmann constant. Combining Equation (3.45) with the definition of the refractive index gives the pressure and temperature dependent refractive index [44, 97]:

$$\frac{n_0^2 - 1}{n^2 - 1} = \frac{p_0 T}{p T_0}, \tag{3.46}$$

where n denotes the refractive index at pressure p and temperature T, and n_0 denotes the refractive index given by the used reference, which was recorded at a pressure p_0 and a temperature T_0. The scaling of the refractive index provided by Equation (3.46) is valid in the low-pressure regime of HHG[9], but is slightly modified at high pressures by an effect known as the Clausius–Mossotti relation after its discoverers [98]. The Clausius–Mossotti relation describes a local electric field correction due to the polarization of nearby atoms. The above discussion on the pressure dependence of the refractive index can also be applied to the plasma contribution, providing an additional tuning parameter for phase-matching together with the focal position and the intensity.

Phase-matching Equation for HHG

The phase-matching of HHG can thus be expressed as in the following equation:

$$\Delta k_\Omega^{\mathrm{tot}}(p,z,I) = \underbrace{\Delta k_\Omega^{\mathrm{neutral}}(p,I)}_{>0} + \underbrace{\Delta k_\Omega^{\mathrm{plasma}}(p,z,I)}_{<0} + \underbrace{\Delta k_\Omega^{\mathrm{dip,traj}}(z,I)}_{\propto \mathrm{sign}(z)} + \underbrace{\Delta k_\Omega^{\mathrm{Gouy}}(z)}_{<0}, \tag{3.47}$$

where the amplitude of the first two components can be tuned through the pressure. The last three components depend on z either directly (the last two terms) or indirectly, through the ionization rate in the case of the plasma term. The intensity (I) of the driving laser affects the first three terms by: depletion of the ground state (the first term), changing the ionization rate (the second term) and direct coupling to the dipole phase (the third term).

In experimental conditions where $\Delta k_\Omega = 0$ the produced HHG signal will grow quadratically with both the length of the medium[10] and the generation pressure[11]. The quadratic pressure scaling comes from the electric susceptibility tensor, which scales with the number density of the gas (as described above), and thereby the pressure. Consequently, experimental conditions where the HHG yield scales quadratically with the pressure is called phase-matched HHG, while one may say that the phase-matching conditions improves, if the HHG yield scales faster than quadratically with

[9] Generally around 10 mbar, but also in the few bar regime used in the studies presented in Papers **I-IV**.

[10] Similarly to Equation (2.32) for second order DFG.

[11] Strictly speaking this is a very unlikely event as the first two component of Equation (3.47) would have to perfectly balance each other as the pressure is changed.

the pressure, and the phase-matching conditions diminishes, if the scaling is less than quadratically with the pressure. Even under perfect phase-matching conditions the HHG yield is ultimately limited, due to re-absorption of the XUV light [99].

Chapter 4

Experimental Attosecond Sources

HHG was described from a theoretical point of view in the previous chapter. In this chapter HHG will be discussed from experimental point of view. The chapter consists of three sections. The first section briefly describes the XUV spectrometer that was used to record most of the HHG spectra presented in this work. The following two sections describes HHG the three laser systems presented in Chapter 2. Cases in which the seemingly simple theories presented in the previous chapter diverge significantly from the experimental observations will be discussed, highlighting the importance of complementing theory with experimental studies.

4.1 Imaging Spectrometer

Most of the harmonic spectra presented in this thesis were recorded using a home-built, flat-field imaging spectrometer[1] based on a grating with variable line spacing[2] [100, 101] and a 78 mm diameter micro-channel plate with an attached phosphor screen[3]and a camera[4]. The grating, which is placed on both a rotational[5] and a translational positioner[6], diffracts and refocuses the XUV in the horizontal direction, while the vertical direction is left unaffected. The vertical axis thus provides the spatial profile of the XUV light, while the horizontal axis provides the spectral content. The MCP has a cesium iodide coating to enhance the detection efficiency in the vacuum ultraviolet regime [102]. Finally, the grating can be shifted out the direction of the

[1] See Paper **I** for additional details.

[2] Two gratings from Hitachi were employed during this work: grating 001-0639 and grating 001-0640. The first has a nominal line spacing of 600 lines/mm, while the second has 1200 lines/mm. The first grating was used for vacuum ultraviolet detection in the range of 10-60 eV, while the other was used for the detection of XUV light in the range of 20-120 eV.

[3] Custom product, Photonis.

[4] Allied Vision Technologies, Pike F-505B.

[5] Smaract, SR-3610-S-HV.

[6] Smaract, SLC-2460-S-HV.

beam propagation allowing the XUV to be sent directly to a XUV camera[7] for flux calibration. The imaging spectrometer was built during the first six months of this work, and was used in the studies described in Papers **I**, **II**, **III**, **IV**, **IX** and **VIII**, as well as for recording HHG spectra using the TOPAS. The spectrometer is illustrated in Figure 4.1.

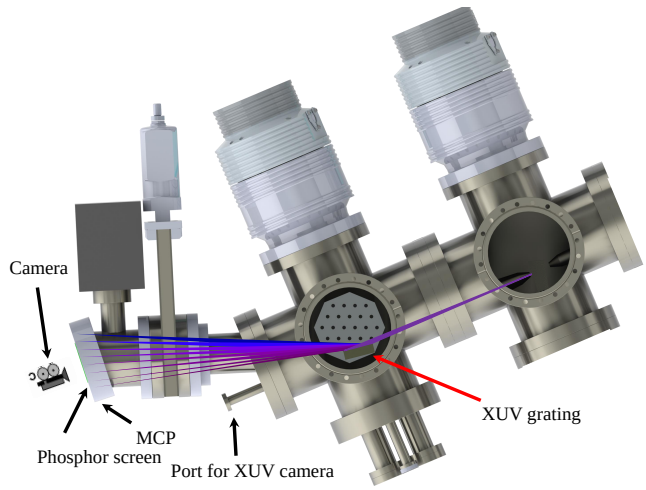

Figure 4.1: The XUV spectrometer used in this work.

4.2 1 kHz High-order Harmonic Generation

The workhorse for attosecond experiments in Lund has for a long time been the 1 kHz laser system described in Section 2.2.1. A recent trend in the attosecond community has been to improve the tunability of the harmonic, and thereby attosecond, sources [103, 104]. Figure 4.2 illustrates two different methods of doing this. The first way, presented in the left column, consists of tuning the carrier wavelength of the driving laser. In this case, the carrier wavelength is produced by the TOPAS (see Section 2.2.3) and tunability is obtained by rotating the nonlinear crystals inside the OPA. Harmonics are shown for four different driving wavelengths. The second method of controlling the spectrum of the produced harmonics, presented in the right column, consists of changing the gas pressure inside the generation cell. The spectral regime of HHG can also be tuned by changing the intensity of the driving laser, leading to a blue shift of the IR pulse, and thus the harmonics [105]. In the present work, the first technique was mainly used to obtain tunable harmonics, since the other techniques is less controllable. The harmonics produced by tuning the carrier wavelength around 800 nm laser is presented in Section 6.1.2, and were used for the studies described in Papers **VII** and **IX**.

[7] Andor, iKon-L DO936N-M0W-BN.

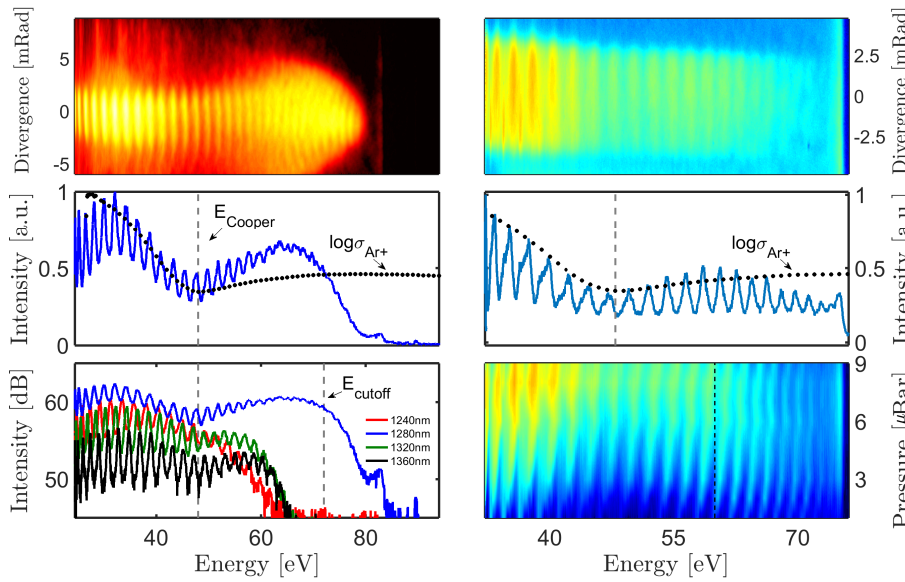

Figure 4.2: Tuning harmonic sources. The top row shows the spatial and spectral profiles of harmonics produced in argon with driving wavelengths of 1280 nm (left) and 800 nm (right). The pulses have durations of roughly 35 fs (for the 1280 nm pulse) and 20 fs (for the 800 nm pulse). The middle row shows a spectral line-out at a divergence angle of 0 mrad. The logarithm of the photo-ionization cross-section of argon (from Ref. [106]) is indicated by the dotted line for comparison. The reason for making this comparison will be given in Section 4.3.3. The bottom row shows various methods of tuning the wavelength of the XUV frequency comb. The left panel shows the effect of tuning the carrier wavelength of the driving laser using the TOPAS between 1240 nm and 1360 nm. The right panel demonstrates the effect of changing the pressure of the generation medium.

4.2.1 Non-collinear High-order Harmonic Generation

The pulses delivered by the 1 kHz system have a duration of around 20 fs corresponding to roughly 7.5 cycles of the carrier wave. This is too long for SAP generation. In order to produce SAPs with this system, these pulses were spectrally broadened in a hollow-core capillary. The broadband pulses were subsequently compressed to a duration of 3.2 fs, corresponding to ∼1.2 cycles, using the combination of dual-angle chirped mirrors from Ultrafast Innovations, a water cell, and a pair of wedges for fine tuning of the dispersion [107]. The few-cycle pulses were characterized by the D–scan technique developed by Miranda and co-workers [108]. Such short pulses are, in principle, short enough to produce SAPs by themselves, but in the present work (Paper **VIII**) they were used in a proof-of-principle experiment for non-collinear optical gating (NOG) [109]. Optical gating techniques [110–112] are generally used to produce SAPs when the pulse from the driving laser is too long for direct generation of SAPs. The methodology used in the study described in Paper **VIII** consisted of

crossing two few-cycle NIR fields at a non-collinear angle. Far away from temporal overlap between the two fields, each field is itself capable of producing harmonics, in its propagation direction. In regions of temporal overlap between the two fields light is instead emitted at the intermediate angle. This is shown in Figure 4.3.

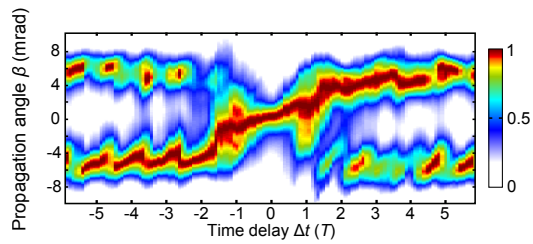

Figure 4.3: The spectrally integrated XUV signal as a function of time delay between two few-cycle fields at a non-collinear crossing angle. Far from temporal overlap, two XUV beams are produced at divergence angles corresponding to ±5 mrad. At temporal overlap light is emitted at a divergence angle of 0 mrad. This figure was adapted from Paper **VIII**.

4.3 High-Repetition Rate High-order Harmonic Generation

Although the flux of XUV light produced by HHG is generally very low compared to that achievable at large scale facilities such as synchrotrons and free-electron lasers [26, 113], the XUV pulse energies are actually too high for some kinds of experiments such as certain coincidence based measurements [6] and surface science imaging measurements [114, 115] and the XUV pulse energies must be reduced even for 1 kHz laser attosecond sources[8].

[8] In surface science experiments, space-charging effects caused by the emission of multiple electrons per shot can cause blurring of the image [116]. In coincidence experiments, the count rate should be on the order of 1 event per shot, so that a double event can be interpreted as a coincidence, otherwise covariance analysis may be needed instead of true coincidences [117].

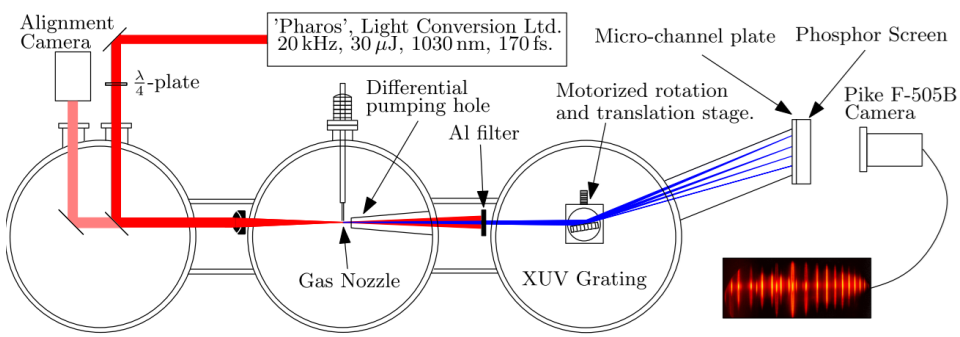

Figure 4.4: The experimental setup constructed for high-repetition-rate HHG. The setup was used in the studies reported in Papers **II**, **III** and **IV**. Paper **I** provides a detailed explanation of characteristics of the setup.

It has long been a goal of the Lund Attosecond Physics Group [118, 119] to combine an attosecond source with a surface science imaging tool known as a photo-emission electron microscope (PEEM) [120], in a technique called AttoPEEM in order to allow real-time measurements of surface plasmon oscillations [3]. The PEEM was used in Paper **X** together with the TOPAS[9] for a proof-of-principle experiment to image plasmonic resonances at the main telecommunication wavelength of 1550 nm. The measurements presented in Paper **X** are only still-frame pictures, however, it may be possible to obtain time-resolved measurements of the surface plasmons using pump-probe[10] experiments with attosecond pulses.

Paper **I** presents a setup for high-repetition-rate HHG. The setup, which is shown schematically in Figure 4.4, consists of the XUV spectrometer presented in Section 4.1, combined with a high-repetition-rate laser source, described in Section 2.2.1, and an open-ended continuous gas jet. In order to achieve the required intensities for HHG the laser is tightly focused by a 10 cm achromatic lens. At low pulse energies the phase-matching pressure [Equation (3.47)] is higher than that with standard pulse energies [121]. In this setup the phase matching occurs at around 2-5 bar. The scheme presented in Figure 4.4 was also used in the studies reported on in Papers **II** and **III**. These two experiments will be explained at the end of this chapter.

Paper **I** additionally presents the characteristics of the HHG source as a function of both the repetition rate of the laser system and the choice of generation medium (argon and neon). Unfortunately, it has subsequently been discovered that the values given in the paper is overestimated, due to wrong information about the quantum efficiency of the XUV camera [119]. The overestimation depends on the photon energy: for 50 eV photons the reported flux is overestimated by a factor 20, while the overestimation is a factor 6, in the case of 20 eV photons. An erratum to the published article is currently being prepared.

Optical Parametric Chirped Pulse Amplification

After the initial demonstration of the high-repetition rate HHG setup, all the equipment, apart from the laser, was moved to the new OPCPA system[11], where it was intended for use in pump-probe experiments with SAPs and the PEEM. Paper **IV** describes the initial testing of HHG with the system. The dynamics of few-cycle pulses in HHG was also explored. Figure 4.5 shows the highlight of this experiment. The experiment is explained using multi-pulse interference, described in Section 3.1.1. Unfortunately, the average power of the OPCPA was somewhat too low for pump-probe experiments. The system has subsequently been upgraded, and a new attosecond setup constructed. As I was not involved in either part, this is described further in thesis.

4.3.1 Quantum Path Interferences by Chirped Pulses

We now return to the experiments conducted with the Pharos laser. As discussed above (Section 3.2.2) the harmonics in the plateau region are generated by several electron trajectories, which have different dipole phases. However, the emission is

[9] See Section 2.2.3.
[10] See the beginning of Chapter 5.
[11] See Section 2.2.1.

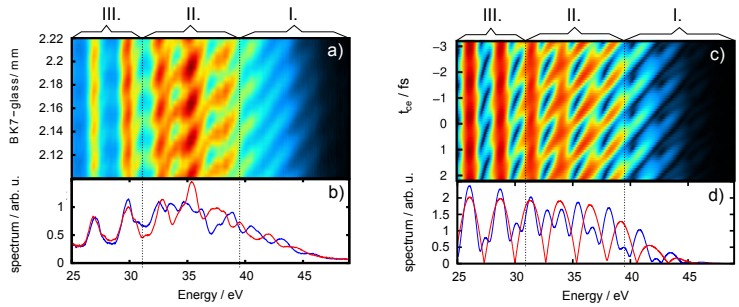

Figure 4.5: CEP dependent HHG for a few-cycle driving laser. (a) and (b) show experimental data obtained with the OPCPA system described in Section 2.2.1. (c) and (d) show numerically calculated data. (a) and (c) show the on-axis spectrum as a function of CEP of the driving laser. In (b) and (d) the harmonics spectra with a change in CEP of $\pi/2$ are compared. Three regions of interest can be identified. (I) Only a few half-cycles (2-3) contribute to these harmonics, and the harmonic spectra consequently shift from even to odd harmonics depending on the CEP. (II) A larger number of sub-cycles contribute to this spectral region, and the harmonics split up and shift in energy depending on the CEP. (III) A large number of sub-cycles contribute to these harmonics, and the CEP consequently only affects the amplitude of the harmonics, while the photon energies of the harmonic remain roughly constant. From region (III) it is clear that the CEP of a laser also affects long pulses, although to a lesser extent than short pulses. The figure was reproduced from Paper **IV**.

generally dominated by contributions from the first two quantum trajectories (the short and long trajectories). It is well-known that in this region the dipole phases are much larger for the long trajectories than for the short trajectories [85], but the exact numbers are generally unknown. In order to determine the dipole phases of this set of trajectories we performed an experiment[12], where HHG was optimized to have strong contributions from both sets of trajectories. This was done by placing the gas jet in the focal plane of the laser and adjusting the experimental parameters accordingly, as described in Section 3.3. A typical far-field spatial–spectral profile of the harmonics, under these conditions, has already been presented in the previous chapter (Figure 3.1). Here an enlarged view of a particular harmonic is presented in Figure 4.6 (a). The spatial–spectral profile of the harmonic clearly exhibits a ring-like structure with a filled central part. This profile arises as a consequence of the larger dipole phase of the long trajectories relative to that of the short trajectories [122]. According to Equation (3.25) the spatial and time dependence of the dipole phase can be written as:

$$\Phi_q^j(r,z,t) \approx \Phi_j^q + \alpha_j^q I\,(r,z,t)\,. \tag{4.1}$$

As apparent from this expression, the spatial and temporal phase of the light generated by the two trajectories will follow the intensity profile of the driving laser. At the same time, the amplitude of the emission will follow the intensity profile to some power, which depends on the harmonic order [Paper **III**]. Assuming that the generation pulse is Gaussian both in time and space, the emission will also be described by a Gaussian amplitude envelope with a Gaussian phase. Taylor-expanding the phase

[12] Which is presented in detail in Paper **III**.

around the center of the pulse in both time and space, shows that only even order terms contribute[13]. Thus, the emission can be seen as Gaussian pulse with a nonlinear phase with even order terms. A temporal Fourier transform of such a pulse will be symmetrically broadened compared to a transform-limited pulse, as discussed in Section 2.1.1. Similar to the temporal Fourier transform will the spatial Fourier transform of the near-field distribution be symmetrically broadened in the far-field compared to a near-field with no high-order nonlinear spatial phase. Since $|\alpha^q_{\text{long}}| \gg |\alpha^q_{\text{short}}|$ the broadening is larger for emission caused by the long trajectories. Emission from the two sets of trajectories can thus be achieved by spatial–spectral discrimination. Due to spatial-temporal coupling the broadening of the emission of the long trajectories emerges as a ellipse in the spatial–spectral measurement.

The method of spatial separation between emission caused by the two trajectories was verified by changing the chirp of the driving laser field as presented in Figure 4.6 (b) and (c). Interference fringes can be observed in lineouts for regions where emission caused by both trajectories overlap, both spectral [Figure 4.6 (b)] and spatial [Figure 2 in Paper **III**]. In regions, where only the long trajectories contribute [Figure 4.6 (c)] no interference fringes can be observed. The dipole phases were extracted from the measurement by numerical calculations of the interference pattern caused by two Gaussian pulses with different wavefronts, due to the different dipole phases [Equation (3.23)].

The results for the dipole phase of the long trajectories presented in Paper **III** agree well with recent measurements presented for a particular harmonic in reference [123], and a broadband range of harmonics in reference [124].

4.3.2 High-order Harmonic Generation from Elliptically Polarized Fields

So far, only HHG from linearly polarized light has been considered. However, HHG is not limited to being driven by linearly polarized light. The most predominant effect of elliptical polarization is a significant fall in efficiency of the HHG [125], due to a reduction in probability of the electron returning to the parent ion, thus causing a reduction in the recombination probability. This reduction is often understood as being caused by a drift of the electron wave packet after ionization along the minor axis of the electrical field, as schematically illustrated in Figure 4.9. However, the drift, which is due to the phase shift between the two components of the elliptically polarized field, may be partially compensated for by quantum diffusion of the electron wave packet, which allows part of photo-ionized part of the electron wave packet to return to the origin and allows for recombination in slightly elliptical fields. It is often assumed that the transverse drift depends only on the excursion time, which leads to that the conclusion the long trajectories should be significantly more dependent on ellipticity than the short trajectories[14]. This assumption also leads to the interpretation that for the short trajectories the sensitivity to ellipticity increases with the harmonic order, since their excursion times increase with harmonic order. Similarly, this assumption leads to the interpretation that the long trajectories should decrease in sensitivity to ellipticity as a function of harmonic order, since the excursion time is inversely related

[13] Since only the even order derivative of a Gaussian is non-zero at the peak.
[14] See Figure 3.2 (b).

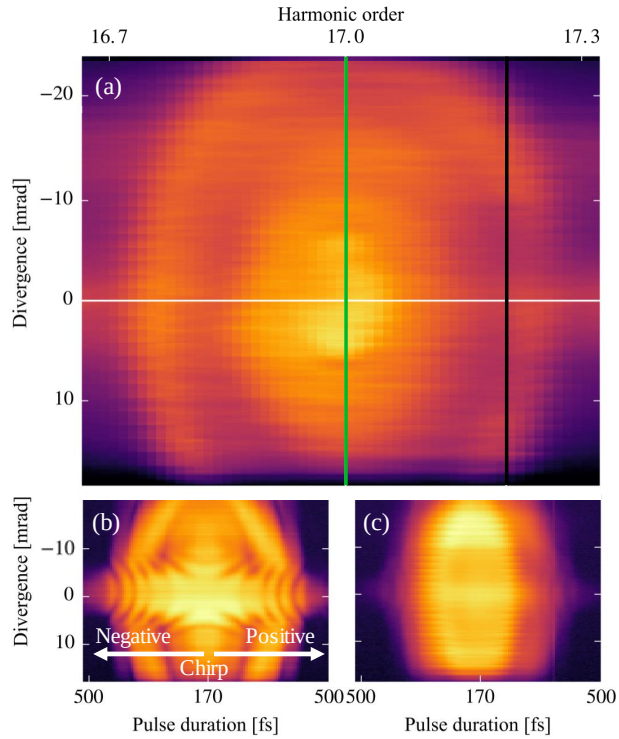

Figure 4.6: (a) Spatial–spectral profile of a harmonic optimized to have contributions from both the short and long trajectories. The emission at the center is caused by both trajectories, while the off-axis emission is mainly caused by the long trajectory [122]. (b) Spectral lineout along the green line in (a) as a function of chirp of the driving laser. (c) Similar to (b), however, along the black line in (a). This figure was adapted from Paper **III**.

to the harmonic order for this set of trajectories. The experimental results presented in Figure 4.8 and Paper **II** show that the last interpretation is not true.

The introduction of ellipticity significantly complicates the possibility of modeling the system; instead of solving the one-dimensional time-dependent Schrödinger equation, a three-dimensional variant is needed for quantum mechanical calculations [126]. Similarly, a three-dimensional version of the SFA is required rather than the one-dimensional variant described in Section 3.2.1. In addition, as will be described in the next section, the single-active-electron approximation breaks down for certain harmonics, which additionally complicates the calculations. Therefore, a more crude approach was adopted to the problem in Paper **II**, where the classical Newtonian equations of motion for an electron in a strong field were solved, with initial conditions set by a quantum mechanical analysis. An elliptical field may be written in the following form:

$$\mathcal{E}(t) = \mathcal{E}/\sqrt{1+\varepsilon^2}[\sin(\omega t); \varepsilon\cos(\omega t)], \tag{4.2}$$

where $0 \leq \varepsilon \leq 1$ denotes the degree of ellipticity, for which $\varepsilon = 0$ and $|\varepsilon| = 1$ denote

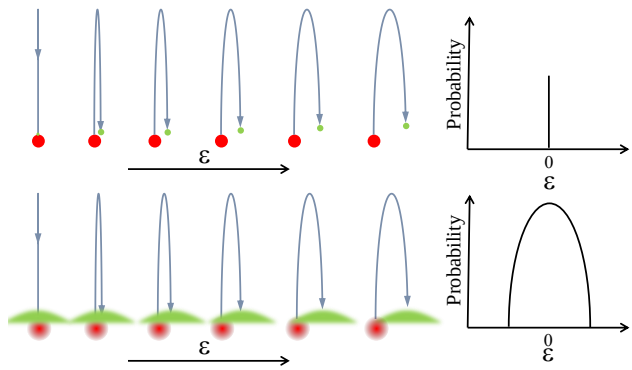

Figure 4.7: Schematic illustration of the transverse drift of an electron in an elliptically polarized field, without quantum diffusion (above) and with quantum diffusion (below).

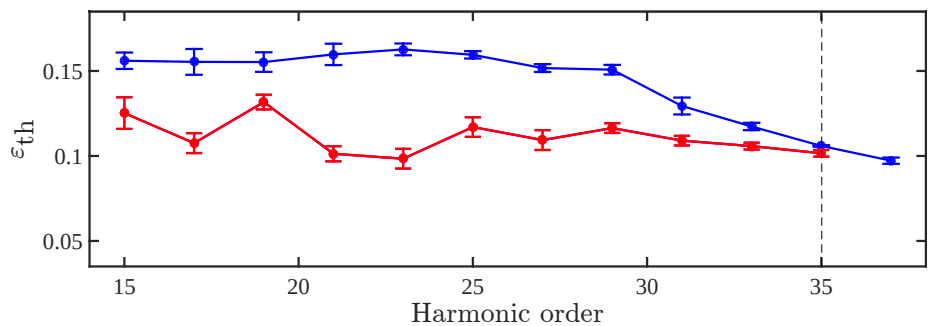

Figure 4.8: Experimental threshold ellipticity, $\varepsilon_{\mathrm{th}}$, of short (blue) and long (red) trajectories as a function of harmonic order. The threshold ellipticity is defined as the ellipticity at which the harmonic intensity has fallen by factor of two compared with the intensity at linear polarization. The dashed line at harmonic 35 indicates the cutoff harmonic. This Figure was reproduced from Paper **II**.

linear and circular polarization, respectively. In analogy with Equation (3.3), the position of an electron as a function time $\mathbf{r}(t)$ in an elliptical field can be calculated as [127]:

$$\mathbf{r}(t) = \mathbf{r}_i + (t - t_i)\mathbf{v}_i + \frac{e\mathcal{E}}{m_e\omega^2\sqrt{1+\varepsilon^2}} \begin{bmatrix} \sin(\omega t) - \sin(\omega t_i) - \omega(t - t_i)\cos(\omega t_i) \\ \varepsilon[\cos(\omega t) - \cos(\omega t_i) + \omega(t - t_i)\sin(\omega t_i)] \end{bmatrix}, \quad (4.3)$$

where $\mathbf{r}_i$ and $\mathbf{v}_i$ denote the initial position and velocity, respectively.

Numerical solutions of Equation (4.3) are presented in Figure 4.9 for different ionization times and initial velocities. It can be observed that ellipticity prevents the electron from returning to the origin if $\mathbf{v}_i = 0$, as the electron accumulates a small uncompensated drift along the minor-axis of the electrical field. However, when the electron is allowed to have a small initial velocity along the minor axis (the green curve in the upper panel) the electrons occasionally return to the origin.

Equation 4.3 can be used to find the return time of an electron, which is ionized

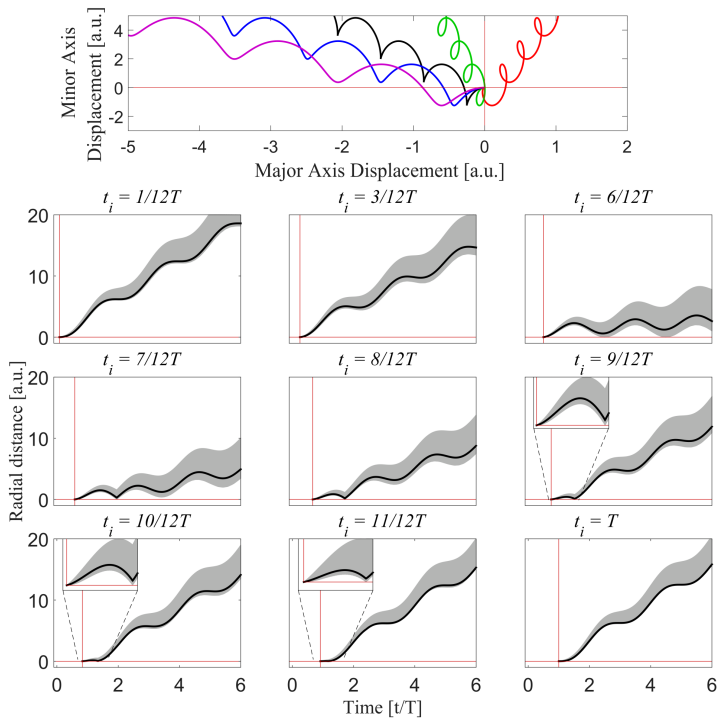

Figure 4.9: Numerical solutions of Equation (4.3) for an ellipticity of 0.3 for various transverse initial velocities. The top panel shows a plot of the displacement along the major and minor axes of the electrical field as a function of time for an ionization time $t_i = 7/12T$. The lower panels show the radial distance from the origin as a function of time for different ionization times. The black curves correspond to an initial velocity of 0.

at a given time by a field with a given ellipticity. Having found the return times, the velocity, and thus the energy, of the returning electron can be determined. Figure 4.10 shows a two-dimensional map of return energies as a function of ellipticity and ionization time. It can be seen from the figure that, for a given degree of ellipticity, two sets of ionization times lead to returning electrons, similar to the short and long trajectories of linear polarization discussed in Section 3.1. As the ellipticity increases the cutoff energy decreases (the peak field strength is decreased), and the ionization time of the cutoff is also shifted to earlier times, as observed in the right-hand figure. This means that the simple analysis of excursion times for the two sets of trajectories under linear polarization breaks down. Additional complexity aries from the fact that the distribution of the initial velocity depends on the ionization time, and the overall instantaneous ionization rate also depends on time.

The origin of an initial velocity may be understood from Heisenberg's uncertainty principle;. At the time of ionization, the otherwise spherically symmetric atomic potential is strongly perturbed by the external laser field, creating a preferred tunneling position, since the position is well-defined (Δx is small) the directionality is not (Δp is large).

The distributions of initial velocities given in Paper **II** were calculated by com-

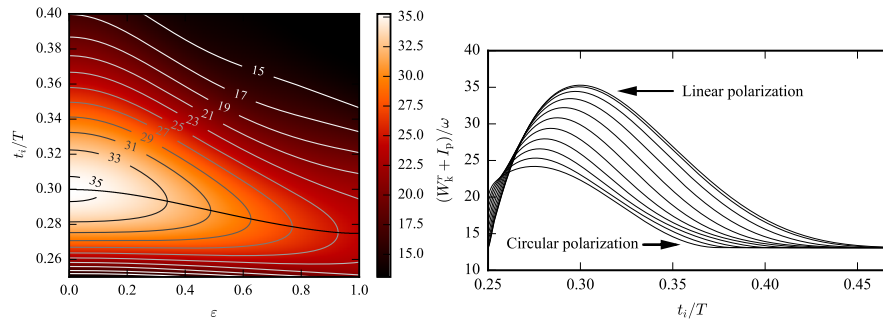

Figure 4.10: Left: Return energy map as a function of ellipticity and ionization time. Right: Change in excursion time for the two sets of trajectories as a function of ellipticity. This figure was adapted from Paper **II**.

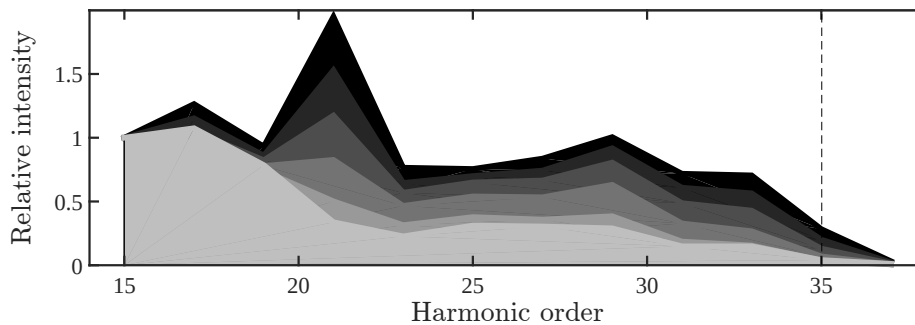

Figure 4.11: A spatially and spectrally integrated harmonic spectrum as a function of ellipticity. The color scale indicates different degree of ellipticity from black ($\varepsilon = 0$) to light gray ($\varepsilon = 0.25$) in steps of 0.05. This figure was reproduced from Paper **II**.

bining the instantaneous tunnel ionization rate in elliptical fields given by the ADK-model [94] with their angular distribution given by reference [95]. The extended three-step model for elliptically polarized fields reproduces the general tendencies with respect to ellipticity fairly well. However, certain harmonics stand out as clearly stronger than others under linear polarization, while the enhancement vanishes as the ellipticity is increased as shown by high-harmonic (HH) 21 in Figure 4.11. This is not reproduced by the model, instead we interpret this to be an effect of resonantly enhanced harmonic generation, which will be further covered in the next section.

4.3.3 Resonant Harmonic Generation

The harmonic spectra presented in Figure 4.2 illustrate the importance of atomic structure in shaping the harmonic spectrum. Prior to the end of the plateau region a clear minimum is observed around roughly 45 eV. Similar shapes have been reported in a number of publications regarding HHG in argon [104, 128], as well as in krypton [129]. The shapes can be explained by minima in the photo-ionization cross-section known as Cooper minima [130]. The Cooper minimum in argon is due to a node in the radial

part of the photo-ionized electron involved in the $3p \rightarrow kd$ ionization, which causes a sign change in the radial overlap integral representing the dipole transition $\langle kd|\hat{z}|3p\rangle$. The position of the node of the d-wave depends on the energy of the photo-ionized electron, and at a specific energy, the two contributions (inside and outside the node) cancel out, resulting in a minimum. The recombination dipole moment is non-zero due to the contribution of the s-wave ($ks \rightarrow 3p$), which is otherwise dominated by the d-wave [130]. The shape of the HHG signal presented in Figure 4.2 can be understood as the combined effect of the influence of a channel with a strong Cooper minimum at $\sim 45\,\text{eV}$ and one without. In the following it will be discussed how the effect of various electron configurations may cause the narrowband shaping of the harmonic spectrum at linear polarization presented in Figure 4.11.

Narrow-band resonantly enhanced HHG was first observed by Toma and co-workers in 1999 [131] as an enhancement of a particular harmonic in argon, while Ganeev and co-workers have extensively investigated resonance behavior in metallic vapors [132]. In our experiments the harmonic energies were well-defined and HH21 was significantly detuned from any known dipole allowed transition in argon. The shaping was thus interpreted as the effect of a dynamically Stark-shifted resonance. As discussed above[15], interactions between different electron configurations may lead to a narrow-band resonance known as a Fano resonance. The high oscillator strength for the transition to the autoionizing state may lead to enhancement of the particular harmonic. In our measurements, the harmonic energy is 1.4 eV detuned from the autoionization energy so this interpretation requires the state to be significantly shifted downwards in energy. A dynamic shift of the resonance energy should depend on the field strength at both the ionization time and the return time, which will be very different for short and long trajectories that lead to plateau harmonics.

The results of the experiment presented in Paper **II** indeed show a clear difference between the long and short trajectories. Enhancement is seen for the long trajectories once the overall intensity exceeds a certain level, while the short trajectories, which probe lower instantaneous intensities at the ionization time, do not exhibit any sign of enhancement at linear polarization as shown in Figure 4.12. In contrast, to the ionization step the recombination step occurs at higher intensity for the short trajectories than for the long trajectories, thus we interpreted the results presented in the paper as caused at the ionization step.

The effect is observed in the ellipticity measurement (Figure 4.11), since the dynamical Stark shift is affected as the ellipticity of the driving laser field is changed in, at least, two ways when ellipticity is introduced, while the pulse energy is kept constant. The first change is due to a drop in the peak field strength, which in the limiting case of a circular polarization leads to drop of peak intensity by a factor of two. In addition, to the drop in peak intensity, the proportionality factor with the intensity of the Stark shift is changed [133].

[15] See Section 3.2.3.

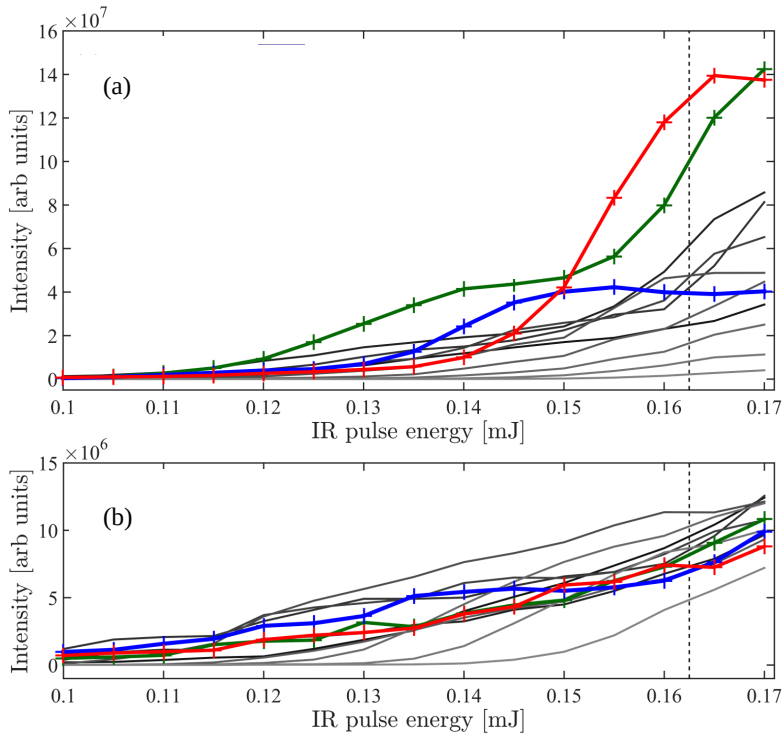

Figure 4.12: Trajectory resolved spatially and spectrally integrated harmonics as a function of pulse energy of the driving laser. (a) Harmonics produced by the long trajectories. (b) Harmonics produced by the short trajectories. Harmonic 17 is shown in green, 21 in red, and 23 in blue. The remaining harmonics are shown in a color scale from black (harmonic 15) to light gray (harmonic 37) with increasing order. The behavior of harmonic 21 is explained in the text, while the details of harmonic 23 and 17 is described in Paper **II**. This figure was reproduced from Paper **II**.

Chapter 5

Attosecond Interferometers

A *pump-probe* scheme is usually utilized in attosecond time-resolved experiments. In the simplest kind of pump-probe experiments, two pulses are used. The first pulse, denoted the pump, is used to start a rapidly evolving process. After a short time delay a second pulse, denoted the probe, is used to terminate the process and create a readout signal. The readout signal depends on the exact delay between the two pulses. In order to study dynamics on the attosecond timescale, attosecond precision is required in the pump-probe delay. This high precision in the delay is usually achieved by the use of interferometers [134–138]. In most cases, one of the pulses is an attosecond pulse (either a SAP or APT) generated through the process of HHG, while the other pulse consists of a copy/fraction of the VIS/NIR pulse used to drive the HHG process. However, several groups are working towards XUV/XUV pump-probe experiments [139–141]. The present work was focused on pump-probe experiments with XUV/NIR pulses.

There are two main kinds of attosecond interferometers. The first utilizes the entire NIR laser pulse to drive the HHG. The NIR and XUV pulses are subsequently spatially separated and delayed with respect to each other by, for example, a two-component split mirror. In the second kind of interferometers the pump and probe pulse are separated prior to attosecond pulse generation. This method allows higher controllability of the individual pulses than with in-line[1] interferometers, but at the cost of the stability of the setup.

During this work two attosecond interferometers of the second type were used. The first setup was constructed for the first XUV/NIR cross-correlation experiments conducted in Lund [142], and although the setup has been upgraded many times over the years, the basic design has remained the same since the first attosecond experiments using the RABBITT technique were performed in 2005 [143]. The setup performed very well for the first decade of attosecond experiments, although reducing interferometric instabilities has been a constant struggle. Therefore a new setup was constructed as part of the present work. Albeit the conceptional design existed before I joined the group, I contributed considerably in all other phases of the construction of this setup, from finalizing the design to building, testing and implementing the

[1] The first kind of interferometers.

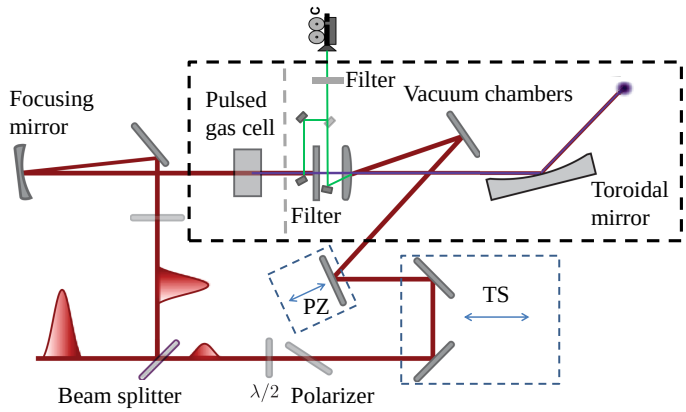

Figure 5.1: PZ, Piezoelectric Translation Stage; TS, Mechanical Translation Stage. This figure was adapted from [31].

setup. The construction of this setup should be considered the main engineering achievement of this work. The original setup was used in the studies described in Papers **V** and **VI**, while the preliminary data for the experiment reported in Paper **VII** were acquired using the original setup. The new setup was used to record the final data used for Paper **VII**. The new setup was also used for the studies presented in Papers **VIII** and **IX**. The original setup is briefly introduced in the next section, and various design criteria for a new setup are discussed. The new setup is presented in Section 5.2.

5.1 The Original Setup

The original setup, which consists of a Mach-Zehnder-like interferometer, is schematically depicted in Figure 5.1. The pulses from the 1 kHz laser system, described in Section 2.2.1, are split into two by a 70/30 beam splitter and sent into two interferometer arms, referred to as the pump and probe arms. After the beam splitter, the pump arm is focused into a 3 mm, long open-ended pulsed gas cell by a gold-coated, off-axis parabolic mirror with a focal length of 44.5 cm. Attosecond pulse trains are produced inside the gas jet, which is operated at 1 kHz and synchronized with the arrival of the laser pulses, through the process of HHG. After generation, the NIR pulses are removed using appropriate metallic filters. For the prototypical case of harmonics produced in argon, aluminum filters are typical used due to their suitable transmission window from 14–73 eV, their low cost, and high durability. Finally, the pump arm is recombined with the probe arm by transmission through the hole of a holey mirror[2]. After recombination the two beams are refocused into the attosecond experiment chamber.

The probe beam arrives at the recombination mirror as shown in the figure. As the beam is collimated at the recombination mirror a convex mirror is used to match the wave fronts of the two beams, so that they have a common focal plane. Two translation

[2]A holey mirror is a mirror with a hole drilled through it. The hole was located at the center in all studies described in this thesis.

stages are placed in the probe arm; a mechanical stage which is used to find the rough position of temporal overlap between the two pulses and a piezo electric stage for the attosecond temporal resolution. The intensity of the probe beam is controlled by a half-wave plate and a pair of reflective polarizers[3]. Most of the interferometer is placed inside a vacuum chamber to avoid undesired nonlinear self-action effects when focusing the laser beams, and due to the strong absorption of XUV light by air.

The two arms of the interferometer are actively stabilized using the spatial interference between the leakage of the probe beam through the recombination mirror and a pick-off of the pump beam prior to filtering, as described in Paper **VI**. In the present case the stabilization beams were passed through a narrow-band 800 nm interference filter and then crossed at a small angle on a camera chip. The crossing of the two beams creates a spatial interference pattern [144] that depends on the wavelength and phase-delay between the two beams. A computer is used to perform a spatial Fourier transform of the pattern to extract the phase, which is then used as a feedback signal to the piezoelectric stage.

In the study described in Paper **VI**, pressure stabilization of the generation medium was also implemented, which relies on feedback between the pressure gauge and the piezo-electric controller for the gas jet.

5.1.1 Design Considerations for Attosecond Interferometers

The active stabilization schemes implemented in the original setup described in Paper **VI**, significantly improved the stability of the setup, but a number of fundamental problems still remain.

The main problem with the setup is that the two interferometer arms are not parity balanced in terms of mirror reflections and focusing elements, and thus that beam pointing fluctuations at the input of the setup affects the two arms differently. Focusing a beam flips the parity of both transverse directions, while a reflection only flips the parity in the plane of incidence. Therefore, if the difference in the number of focusing elements in the two arms is an odd number, the difference in the number of reflections should also be an odd number in both transverse dimensions, which is not the case in the original setup, where compensation is only made in the horizontal direction. A better solution is to use a symmetric number of focusing optics in both arms eliminating the need for compensation with unpaired mirrors entirely [145].

In addition, such a setup should be as small and compact as possible, in order to minimize the effects of vibrations[4]. A symmetric design would also be beneficial in this case, so that large-scale vibrations affect the interferometers equally. It is also desirable to have the whole setup inside a vacuum chamber in order to minimize airflow in the beam paths, which might otherwise influence the stability.

One issue associated with actively stabilized interferometers is the relative drift between the main interferometer and the stabilization interferometer. This problem is more severe, and is generally unavoidable, but could be minimized by reducing both the number of components not shared between the two interferometers. The last source of instability that should be addressed in a new setup is the fact that heating of optical components, mainly due to absorption of the laser in the various components, leads

[3] Schematically shown as transmission through a single polarizer in the figure.

[4] Unless the purpose of the interferometer is to measure vibrations, as in the case of the LIGO interferometers [146].

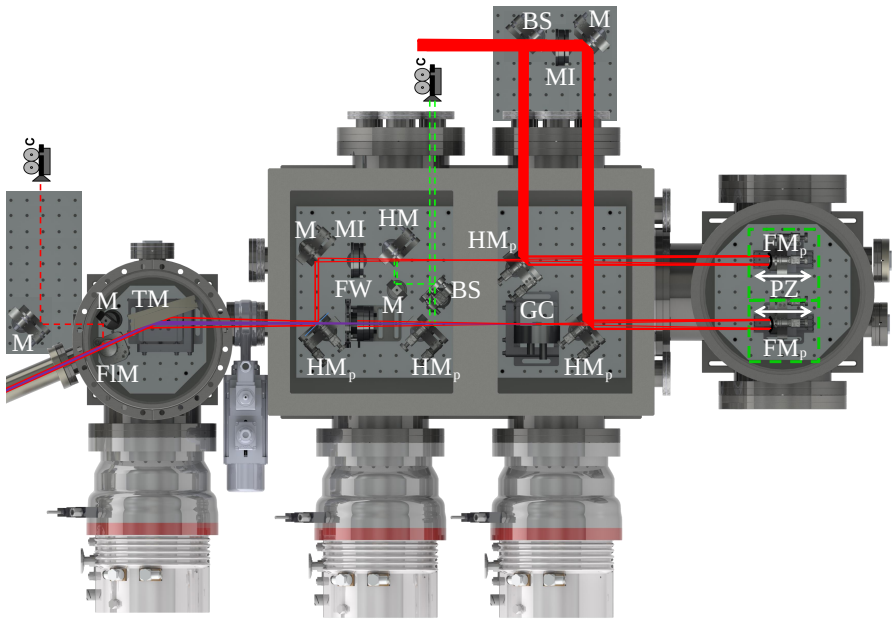

Figure 5.2: Schematic overview of the new setup. BS, beam-splitter; FlM, flip mirror; FM, focusing mirror; FW, filter-wheel with motorized iris; GC, generation cell; HM, holey mirror; M, mirror; MI, motorized iris; TM, toroidal mirror. The subscript p denotes mirror mounts with picomotors attached.

to a change in the relative arm lengths, as the optical components expand. Generally, this drift vanishes after a few hours of constant exposure to the laser. However, the effect can be minimized by reducing the number of optical components with heavy heat load. In the present case, the removal of the polarizers used for attenuation of the probe field, and the replacement of metallic mirrors with dielectric one might have been an option. However, as the new setup should accommodate for experiments using ultrashort laser pulses with very different carrier wavelengths[5], the use of dielectric mirrors was not a practical option as dielectric mirrors with low dispersion are usually limited to bandwidths around 100 nm.

5.2 The New Setup

After having identified the shortcomings of the original setup and the desired features of a new system, a new setup was designed. The result is presented in Figure 5.2. The new setup also resembles a Mach Zehnder type interferometer, where most of the components are placed inside vacuum chambers. Three separate chambers are used, a rectangular box chamber with a separation wall in the middle, and two cylindrical chambers. Each chamber is pumped by a separate magnetically levitated turbo-pump[6] to minimize the vibrations.

[5] See Section 2.2.1 and 2.2.3.
[6] HiPace 700, Pfeiffer Vacuum.

The laser pulses delivered by the system are split directly in front of the vacuum chamber into the two interferometer arms. Inside the vacuum chamber the pump arm is first folded by a holey mirror with a 2.5 mm hole. After the folding mirror, the pulse is focused at 0° incidence angle by a spherical mirror with a focal length of 40 cm back through the hole of the holey mirror. After passing through the hole the beam enters the generation gas cell[7], where HHG takes place. The folding mirror creates a doughnut-like spatial shape of the far-field distribution of the NIR laser pulse. This shape allows us to remove the majority of the NIR laser after generation by a motorized iris[8] placed far enough from the focal plane. A negligible part of the NIR laser pulse is transmitted through the iris, due to a diffraction phenomenon known as Poissons's spot [147]. A filter wheel[9] is mounted on the backside of the iris allowing for spectral selection of the XUV beam, and in order to allow for temporal recompression of the attosecond pulses [29]. Finally, the pump beam arrives at the recombination mirror, where it is recombined with the probe beam by being transmitted through a 4 mm hole. The probe beam has an almost identical path to the recombination mirror, as shown in the figure. The main difference is that the focusing mirror is 50 cm for this beam rather than 40 cm, and no filter wheel is used, since harmonics are not produced in this arm. However, a motorized iris, placed in the far field, is still used to controllable attenuate the probe beam.

After recombination, the two beams are focused into the experimental chamber by a toroidal mirror. A flip-in mirror placed after the toroidal mirror is used to monitor the spatial overlap of the two refocused NIR beams.

The two focusing mirrors are placed on linear stick-slip piezoelectric translation stages with built-in sensor units from Smaract[10], the probe mirror is additionally placed on a high-precision piezoelectric stage from Piezosystems Jena[11]. The identical piezoelectric stages from Smaract are used to optimize the focusing plane[12] and find the temporal overlap between the two pulses. The high-precision piezoelectric stage below the focusing mirror of the probe is used for delay scans up to 400 fs. By moving one of the Smaract stages delay scans with delays exceeding 400 fs is also possible. Furthermore, a number of mirrors inside the vacuum chamber are equipped with picomotors to allow for in vacuum operation.

Two 6 mm holes in the wall between the two parts of the rectangular chamber are used for the transmission of the light pulses, while allowing differential pumping. In operation mode, the generation part of the rectangular chamber has a background pressure around $5 \cdot 10^{-3}$ mbar, while the pressure in the recombination part of the chamber is 2-3 orders of magnitude lower.

The setup is actively stabilized in a similar manner to the original setup. The main difference is that a co-propagating frequency-stabilized helium neon laser[13] is used for stabilization.

The setup was designed for use with pulses delivered directly by the laser system, pulses that have been spectrally broadened and compressed to durations below 4 fs,

[7] GR020, Attotech.
[8] SID-0-22-S-HV, Smaract.
[9] Custom component, Smaract.
[10] SLC-2445-S-HV, Smaract.
[11] PX 100 CAP vacuum, Piezosystems Jena.
[12] For phase-matching purposes in HHG.
[13] R-32734, Newport.

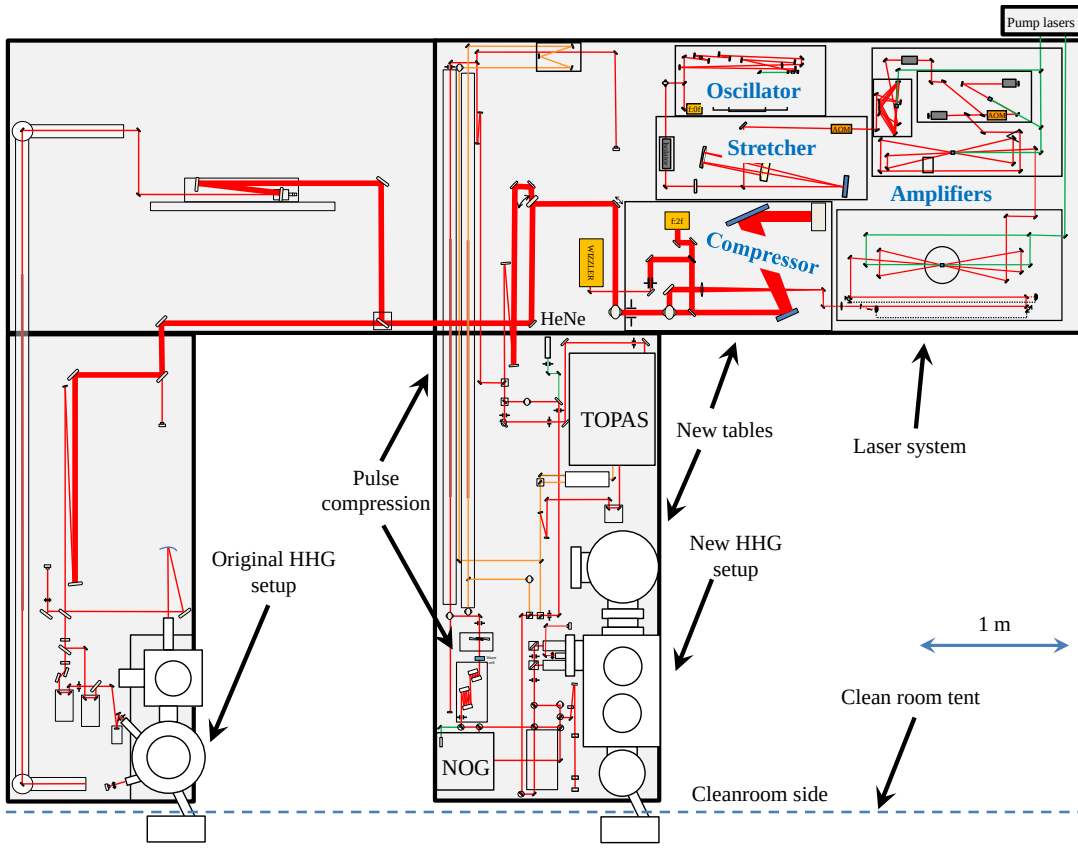

Figure 5.3: Schematic overview of the Attosecond Laboratory showing current and planned activities as of June 2015.

as described in Paper **VIII**, as well as narrow-band and compressed pulses from the TOPAS [148]. In order to meet all these requirements, the setup was designed to use all reflective optics made from metallic mirrors, which exhibit higher achromaticity than dielectric mirrors. The toroidal mirror had a platinum coating, while the remaining mirrors had silver coatings. In most experiments the entrance beam splitter to the setup was therefore also a holey silver mirror, but in some experiments a normal beam splitter was used.

5.2.1 Improvement of the Lab Environment

A large part of improving the interferometric stability of the system was upgrading the environment of the laboratory. A large group effort sought to achieve this during the time of the laser upgrade. In addition to the procedures described in reference [69] a number of other improvements were made. Two new optical tables were purchased, and stiffly connected in order to minimize relative spatial drifts between them. As shown in Figure 5.3, the upgraded laser system was placed on the first table, and the new attosecond setup was assembled on the second table, while the pump lasers

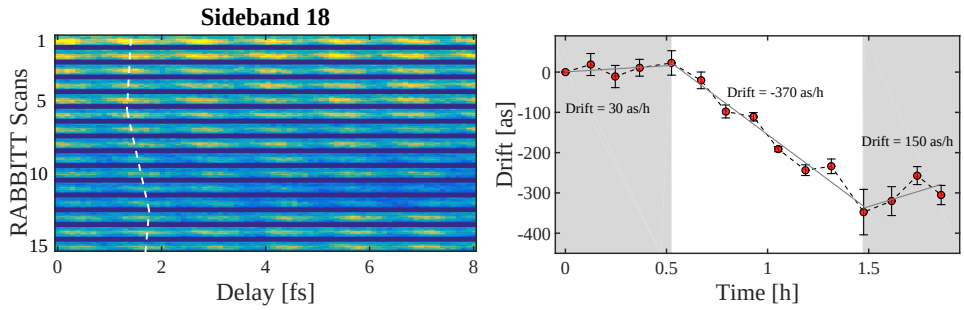

Figure 5.4: Performance of the new setup. The left panel shows raw data for sideband 18 as a function of pump-probe delays for 15 consecutive RABBITT scans. The right panel shows the extracted temporal drift of the setup. The presented data shows the average of the drift measured using sideband 16, 18 and 20 as well as the corresponding standard derivations.

were placed on a separate table. In addition, the heavy load heat sources, such as the current and temperature control units for the pump lasers were moved to an adjacent room, where a centralized vacuum system was also installed. Airtight table covers were placed on the tables in order to minimize fluctuations of the airflow in the optical paths, which can interfere with the CEP of few-cycle pulses. Cleanroom fans were installed above the optical tables and a cleanroom tent was installed to improve the cleanliness of the lab, to better regulate the temperature, and to create a lab space with laminar air flow. The fans were set to run at a low speed to minimize the effects of acoustic noise. Finally, a local Ethernet network was installed, and control computers were moved to a neighboring room to allow for remote operation of the attosecond experiments, removing the necessity of being in the room where when experiments with the highest need of stability were being run.

5.2.2 Performance of the New Setup

The harmonics produced with the new setup were already presented in the previous chapter[14]. The high harmonic cut-off for argon using 800 nm pulses with this system[15] indicates that the focusability of the laser pulses is not heavily affected by the doughnut-like shape of the farfield distributions, due to the folding on holey mirrors. In contrast, the reduction in spherical aberration, due to the 0° incidence angle on the focusing mirrors, seems to more than compensate for the loss of the central part of the beam. Ray-tracing simulations using FRED[16] have verified this [145].

In order to quantify the interferometric performance of the new setup a number of consecutive RABBITT scans were performed, as shown in the left-hand side of Figure 5.4. The RABBITT technique will be described in more detail in Section 6.1.1. The important aspect here is that it is an interferometric cross-correlation method, which depends on the temporal delay between a NIR pulse and an XUV pulse.

Performing the same measurement repeatedly provides a figure of merit for the reproducibility and thus the stability of the setup. In the ideal case, the horizontal

[14] See Figure 4.2.
[15] Presented in Figure 4.2.
[16] A commercial software commonly used for Ray-tracing.

oscillations in the figure would be perfectly aligned. However, a small uncompensated drift is observed as indicated by the white dashed line in the left-hand side of the figure.

By comparing the phase of the modulation it is possible to extract information on the drift between the two interferometer arms. The right-hand side of the figure shows the uncompensated drift as a function of time, extracted from three different XUV photon energies simultaneously. For the first half hour of the measurement, where the system performs optimally, the average drift is only ≈ 30 as per hour. This can be compared to the best performance of the original setup, which had an uncompensated drift of ≈ 800 as per hour, as discussed in Paper **V**.

The region of high instability is probably due to instability of the source, which is indicated by the large variations in signal strength of the RABBITT trace. Furthermore, active stabilization of the generation pressure had not been implemented at the time of this measurement.

5.2.3 Limitations and Possible Further Improvements

The active stabilization scheme is ultimately limited by the frame rate of the camera at $\approx$150 Hz and the response time of the piezoelectric stages, which is 70 ms for the Jena piezosystem and 30 ms for the Smaract stages.The temporal delay detection scheme could be significantly improved in terms of speed by, for example, the technique of homodyne detection, as described in reference [137]. However, the bottleneck of the stabilization system would still be the control of the piezoelectric stages. Nevertheless, homodyne detection would allow for pulse-to-pulse tagging of the pump-probe delay, as the technique can be performed at MHz rates using field-programmable gate arrays [149].

The setup was originally optimized to perform as a high-stability interferometer for RABBITT-type experiments and traditional transient absorption-type experiments[17], where a delay scan range of a few hundreds of femtoseconds between the two arms would be more than sufficient. A delay change of 200 fs only amounts to a movement of the probe focusing mirror of 30 µm, which is at least an order of magnitude shorter than the Rayleigh length. Delay scans of this length by translation of the focusing mirror therefore have minimal impact on the probe profile in the interaction plane of the setup. However, the discovery of controlled free induction decay presented in Paper **IX**, and discussed in Chapter 6, has revealed the possible need to extend the delay scans to several picoseconds. An upgrade of the setup would therefore require decoupling of the focusing optics from the delay mechanism for long delays.

[17] See Section 6.2.

Chapter 6

Applications of Attosecond Pulses

After the introduction of both the attosecond sources in Chapter 4 and the attosecond interferometers in Chapter 5, we are now fully equipped to perform attosecond pump-probe experiments. This chapter presents the two different types of attosecond pump-probe experiments performed during this work. The first part of this chapter presents how one may extract photo-ionization time delays through photo-electron spectroscopy. The second part of the chapter presents work on photon absorption spectroscopy, which recently has received a great deal of attention in the attosecond community, due to the complementary information to photo-electron spectroscopy about complex systems provided by the technique.

6.1 Attosecond Time Delays

When a photon is incident on an atom, the process of photo-ionization may occur if the photon has an energy E higher than the ionization potential I_p. In this case, the photo-electron produced will have a kinetic energy of [150]:

$$T = E - I_p. \tag{6.1}$$

Although the mechanism of the production of photo-electron and an ion is generally well-known, the dynamics of the process is still not clear. For example, how do the electrons reorganize after the initial excitation? How long time does the reorganization take? What happens if the system is subjected to a second photon, before reorganization is complete? Is the electron ionized directly after the absorption of the photon, or does it take some time before the electron is ejected? One of the main goals of attosecond physics is to try to answer these types of questions for atoms as well as more complex systems. In the following time delays in photo-ionization will be discussed.

The concept of time delays in quantum mechanics was first introduced by Eisenbud in 1948 [151, 152]. Eisenbud proposed that the energy derivative of a phase shift could be interpreted as a quantum mechanical time delay. Based on the interpretation of

Eisenbud, Wigner created a formalism for determining time delays in scattering processes. In the framework of scattering, the time delays were defined as the derivative of an asymptotic phase shift between an incoming and an outgoing spherical wave representing a particle interacting with a scattering potential compared to that of a particle not interacting with a potential.

The asymptotic phase shift can be interpreted as a change in the local velocity of the particle in the vicinity of a potential. In the case of an attractive potential, the local velocity will be increased as the particle approaches the potential minimum, while it will be reduced after the particle has passed the minimum of the potential, where the force is antiparallel with the direction of propagation. In the absence of external forces, the particle returns to its initial velocity far away from the potential.

In the quantum mechanical picture the induced phase shift can be written [30]:

$$\delta(E) = \frac{1}{\hbar} \lim_{x\to\infty} \int_{-\infty}^{x} dx' \left[p(x) - p_0\right], \tag{6.2}$$

where $p(x)$ and p_0 are the local and asymptotic momentum, respectively.

Based on the interpretation of Wigner and Eisenbud the delay can be written as:

$$\tau_W(E_0) = \hbar \left.\frac{\partial \delta}{\partial E}\right|_{E_0}, \tag{6.3}$$

which is often referred to as the Wigner time delay. In the case of photo-ionization time delays, there is only an outgoing spherical wave, which leads to a phase shift of half of the scattering phase [30].

6.1.1 Time Delay Techniques

As the time delay originates from the phase shift of an electron wave packet, direct measurements of photo-ionization time delays without a reference clock would be meaningless. Therefore, attosecond physics instead deals with relative delays. A relative photo-ionization time delay was first observed in a tungsten crystal, where a difference in time delay of 110 as was measured between the emission of photo-electrons from localized valence electrons and those that are ionized from the delocalized conduction-band [2]. Relative delay measurements were subsequently extended to atoms [4, 5], while delays in molecules have yet to be observed [153]. The first delay measurements in atoms were based on a comparison between inner-valence and outer-valence shell electrons in neon [4] and argon [5].

All these measurements depend on cross-correlation, frequency-resolved optical gating (X-FROG [155]) measurements between a NIR and an XUV pulse [156]. In the time delay measurements in tungsten and neon mentioned above, the X-FROG experiment relied on a strong-field effect known as attosecond streaking [22], while the time delays in argon were measured using the RABBITT technique [21], which is the subject of the next section.

In attosecond streaking, the measurement consists of recording the momentum distribution of photo-electrons ionized by a SAP in the presence of a strong few-cycle NIR probe. The acquired distribution depends on the vector potential of the NIR pulse at the time of ionization, thus creating a map between time and photo-electron energy. The streaking spectrum may be approximated by the SFA, where the ionization step

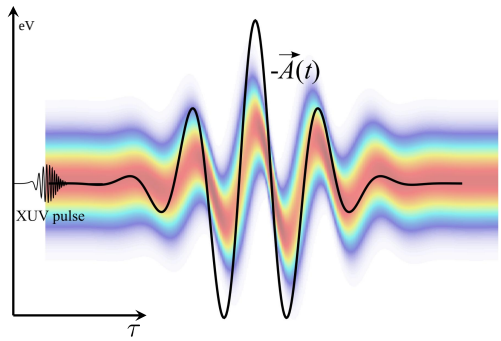

Figure 6.1: Simulated photo-electron distribution as a function of pump-probe delay in the case of attosecond streaking without the effects of atomic structure.This figure was adapted with permission from [154].

is the absorption of an XUV photon. An iterative algorithm called frequency-resolved optical gating for complete reconstruction of attosecond bursts (FROG-CRAB) was developed in 2005 to reconstruct both the NIR and XUV fields [157]. Figure 6.1 shows a simulated streaking spectrum using the SFA scheme. The delay measurements described in references [2, 4] were performed by comparing streaking spectra from photo-ionization of different shells, such that the photo-electron distributions did not spectrally overlap. Any difference in the shape of the two photo-electron spectra were then interpreted as being caused by differences in the atomic, or band structure, of the target. In streaking, the laser induced delay and the ionization delay, *i.e.,* the Wigner delay, can be added independently [158, 159]:

$$\tau_{\text{Streak}} = \tau_W + \tau_{\text{Laser}}\,, \tag{6.4}$$

however, τ_{Laser} must be extracted numerically. The laser-induced delay is conventionally called the continuum–continuum delay, τ_{cc} [30], or Coulomb–laser coupling, τ_{CLC} [159]. The streaking method and the FROG-CRAB algorithm are in principle not limited to few-cycle pulses together with SAPs. However, due to convergence problems of the algorithm, very long and stable delay scans are needed for long pulses [154].

RABBITT

In the limit where the light fields are weak, the system can be described using second-order perturbation theory, such that the final momentum distribution can be approximated by a sum of interfering two-photon transitions. A specific case is known as reconstruction of attosecond beating by interfering two-photon transitions (RABBITT) [21]. In RABBITT the two mixed fields are an APT and a NIR probe field with an intensity of about $10^{11}\,\text{W/cm}^2$. In the frequency regime of an APT the pulse can be represented as an XUV comb consisting of high-order harmonics of the driving laser[1]. The width of the individual harmonics is inversely related to the number of attosecond pulses in the APT. In the long pulse limit, the APT spectrum can be represented by an XUV comb of odd harmonics with discrete energies. The probe field

[1] See Chapter 3.

used in RABBITT is a copy of the field used to produce the APT, such that the emission or absorption of a NIR photon together with the absorption of an XUV photon will lead to photo-electron energies corresponding to an even number of fundamental frequency photons, *i.e.,* a kinetic energy of:

$$T_{q\pm1} = E_{\mathrm{XUV}} \pm E_{\mathrm{IR}} - I_p = \hbar\Omega_q \pm \hbar\omega - I_p = (q \pm 1)\,\hbar\omega - I_p, \tag{6.5}$$

where I_p is the ionization potential of the target. In RABBITT these photo-ionized electrons are referred to as sidebands, since they only occur when there is temporal overlap between the two interaction fields[2]. As is apparent from Equation (6.5),

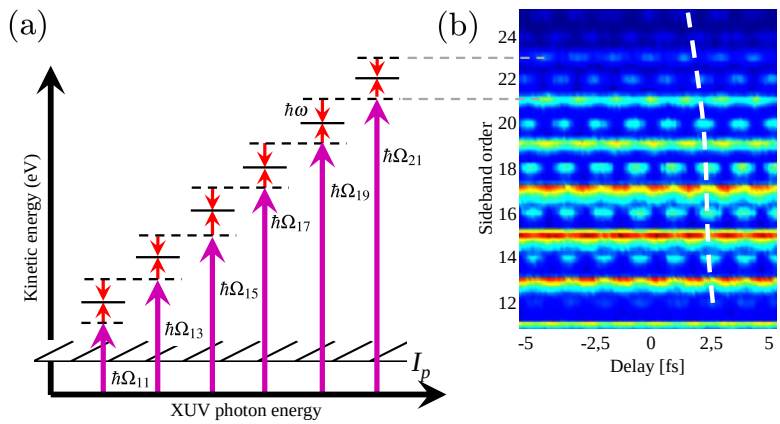

Figure 6.2: (a) Schematic energy diagram of two-photon processes leading to sidebands in the photo-electron spectrum. Quantum path interference leads to modulations in the intensity of the sidebands. (b) Typical experimental RABBITT spectrogram from argon (from Paper **V**) as a function of photo-electron energy and the delay between the NIR field and APT. The offsets of the modulations of the various sidebands contain information about both the APT and the atomic structure. The white dashed line indicate the maximum of the various sidebands showing the chirp of the photo-ionized wave packet.

two different quantum paths can lead to the same photo-electron energy, namely the absorption of two consecutive harmonics followed by stimulated emission of a NIR photon for the more energetic XUV photon, and absorption of a NIR photon for the less energetic photon. This concept is schematically illustrated in Figure 6.2 (a) for typical harmonic orders. The probability of either event occurring depends on the phase delay between the XUV and NIR fields, and the intensity of the photo-electron sideband therefore depends on the XUV–NIR delay τ. Figure 6.2 (b) shows an experimentally measured photo-electron spectrogram of argon taken (from Paper **V**) as a function of the time delay between the two pulses. The sideband intensity can be written as a function of the XUV–NIR delay [21, 160]:

$$S_q(\tau) = \alpha_q \left[(1 - \beta_q) + \beta_q \cos\left(2\tau\omega_{\mathrm{IR}} + \Delta\phi_q + \Delta\phi_q^{\mathrm{int}}\right)\right], \tag{6.6}$$

where α_q describes the delay-averaged amplitude of the sideband, and $|\beta_q| \leq 1$ is a measure of the relative strength of the two quantum paths leading to the sideband. a_q

[2]This is not strictly true; in the case of resonant effects sidebands may occur after temporal overlap between the two fields, as long as the excited resonance has not decayed when the second pulse arrives.

depends on the spectral profiles of both the XUV and NIR light, as well as on the two-photon transition matrix element. $\Delta\phi_q = \phi_{q-1} - \phi_{q+1}$ represents the phase difference between the two harmonics involved in the two-photon transition, and $\Delta\phi_q^{\text{int}}$ represents an intrinsic phase shift due to the complex part of the two-photon transition, *i.e.,* the shift caused by the atom itself. In RABBITT, it is usually assumed that the pulses are so long that the temporal envelope of the laser field does not change over duration of the RABBITT trace, and the physics is then contained within the phase of the sideband. By differentiation of the phase of the sideband can be written:

$$\arg\left(S_q\right) = 2\omega_{\text{IR}}\left(\tau + \tau_q + \tau_q^{\text{int}}\right), \tag{6.7}$$

where τ_q^{int} represents the intrinsic time delay, which in atoms corresponds to the Wigner delay, τ_W, described above, and τ_q is the group delay of the attosecond pulse train where:

$$\tau_q = \frac{\phi_{q-1} - \phi_{q+1}}{2\omega}. \tag{6.8}$$

The group delay is conventionally referred to as the atto-chirp.

The RABBITT technique was first applied by Paul *et al.,* in 2001 [21] to measure the duration of the APT, as implied by the name. In the original work the intrinsic shift, due to the spectral response of the atoms, was numerically calculated. However, as is apparent from Equation (6.7), the intrinsic shift manifests itself directly in the RABBITT trace and, thus it is accessible by comparing different spectral regimes using the same harmonics, as demonstrated by Klünder and co-workers in argon [5].

The RABBITT technique has a number of advantages over the streaking technique, the first and most important being its the practical implementation. The experimental generation of SAP are much more difficult than APTs, since a CEP-stable few-cycle laser is a prerequisite for the production of SAPs. CEP stability of the laser is difficult to achieve and even harder to maintain when coupled together with the need of a few-cycle duration. Traditional high-power laser few-cycle pulses usually require various spectral broadening techniques, such as filamentation or the use of hollow-core fibers, which may distort the CEP stability. An alternative method of generating SAP is the use of direct amplification in a broadband high-power OPCPA system, which also maintains CEP stability. However, this type of lasers are still very experimental and require a great deal of maintenance[3].

The second advantage of the RABBITT is the reduced intensity of the probe field, which reduces the amount of undesired side-effects, such as distortion of the atomic cloud, *i.e.,* induced polarization of the core electrons, which allows for a more direct interpretation of the measurement. Finally, as sidebands are only populated by two-photon transitions, detection can, theoretically[4], be almost background free.

The RABBITT technique does, however, have at least two limitations. If the probe field (also known as the dressing field) is too strong, second-order perturbation theory is no longer valid, and in such cases the sidebands may be populated by higher-order transitions rather than only second-order ones, which clouds the phase extraction. An experimental rule-of-thumb method of determining whether the probe field is too intense, is to compare the delay-averaged photo electron intensity between a sideband and a harmonic. If the sideband intensity is greater than half the intensity of the

[3] See Chapter 2 and reference [58].

[4] Although, experimentally very difficult.

harmonic, the probe intensity is usually too high [161]. The second issue with the RABBITT technique is that it measures the average phase of the sidebands.

The Attoclock

In the attosecond time delay measurements discussed above, the reference clock was the ionization time of different electron shells. However, another method has been demonstrated to have attosecond time resolution, namely the attoclock, which is concerned with ionization time delays in the tunneling regime [162]. The attoclock employs elliptically polarized NIR pulses with well-defined instantaneous polarization, as the reference clock for strong-field ionization. The angular distribution of the photo-ionized electrons is then compared with the instantaneous polarization state of the electrical field, in order to determine an absolute reference for the ionization time. Measurements with the attoclock are very similar to the measurements presented in Paper **II** with the exception of the detection scheme. In the present work (Paper **II**), harmonics produced by the returning electrons were observed and information was extracted on sub-cycle effects by comparing the results for different trajectories, while Eckle *et al.,* measured the non-returning electrons and extracted information on the ionization [162].

6.1.2 Time Delay Measurements

The RABBITT technique is usually applied in Lund, due to the ease in interpreting the results, the possibility of studying the response in the XUV, and the lower requirements on the experimental measurements compared to the streaking technique. Experimental RABBITT measurements were conducted the present work using the two attosecond interferometers presented in Chapter 5, together with a magnetic bottle electron spectrometer (MBES), which is shown schematically in Figure 6.3. The

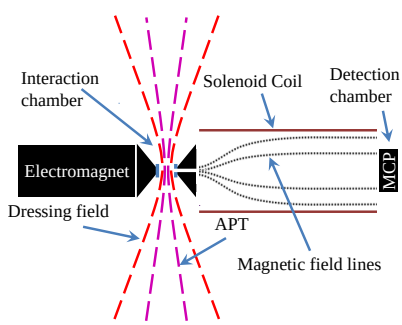

Figure 6.3: Schematic overview of the MBES used measurements with for the RABBITT technique. APT, attosecond pulse train; MCP, micro-channel plate.

MBES is a so-called time of flight (TOF) spectrometer, and is used to record the TOF of the electron wave packet ejected from photo-ionized atoms. The MBES consists of an interaction chamber and a detection chamber, connected by a 0.8 m long flight tube. In the interaction chamber, the two light pulses are crossed with a continuous gas jet supplied from above through a needle valve. Photo-ionization occurs in the

gas jet, where the photo-electrons are created. The emitted electrons are drawn towards the detection chamber by a strong electromagnet ($\sim$ 1T) with two conical polar plates[5], which concentrate the magnetic field into the interaction region. A solenoid coil enclosing the flight tube creates a slowly varying magnetic field along the direction of the detector, such that the of electron emitted at different angles have parallel paths after a distance of a couple of millimeters. The signal is detected by a MCP and a time-to-digital converter acquisition card integrated in a computer. The time-to-digital converter compares the time between a trigger supplied by a photo-diode in the laser chain and the time the electron impacts on the MCP. Two Helmholtz-coils around the flight tube compensate for the earth's magnetic field.

Using the magnets the MBES is able to collect photo-electrons in a solid angle of 2π steradians for energies up to 30 eV. Electrons with higher kinetic can be collected if they are ejected at a smaller angle, or by applying static potentials to electrodes attached to the polar plates.

Temporal Walk-off Effects in High-order Harmonic Generation

The RABBITT technique measures the average microscopic response of the interaction medium. However, this response is affected by macroscopic features, such as the density of the gas, the interaction fields, and the ionization level, much like the HHG process itself.

Let us consider the effects of gas density, for instance. The various atoms in the gas together with the probing field may lead to a local microscopic dipole moment, which leads to a change in the local field [98]. This local field correction, called the Clausius–Mossotti relation, affects the atoms and thus the extracted RABBITT phase. In the RABBITT technique it is generally assumed that the interaction medium is so dilute that macroscopic effects are negligible. However, in the following section, it will be shown that this is not always the case, and macroscopic effects must sometimes be taken into account.

The driving laser used for HHG generally has a different group velocity from that of the harmonics produced, as discussed in Section 3.3. This leads to temporal walk-off between the two pulses as the pulses drift apart over the generation medium. Temporal walk-off was briefly discussed in Section 2.1.4 in the context of low-order nonlinearities for ultrashort pulses, but the principle is the same for HHG. In the present work (Paper **VI**) the temporally induced shift of the attosecond pulse train produced in argon relative to the driving field over the generation medium was investigated.

The shift is characterized as a function of the pressure in the HHG generation gas cell using the RABBITT technique and a second gas jet inside the MBES. The active stabilization of the original attosecond interferometer was used for the first time in these measurements, and it was demonstrated that variations in the generation pressure can lead to a drift in the extracted RABBITT phase. This drift was explained in terms of phase matching[6] together with absorption using a one-dimensional propagation model. Figure 6.4 shows a comparison between the experimental data and the numerical model, where clear qualitative agreement can be seen between the model and the experiment over the energy range studies, except for sideband 16. However, it

[5] Plates with high magnetic permeability.
[6] See Section 3.3.

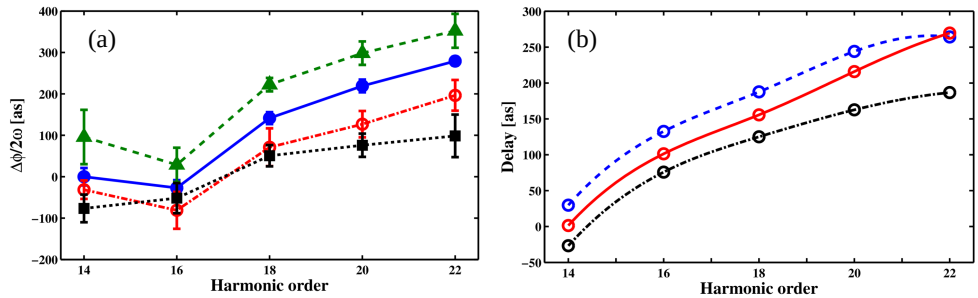

Figure 6.4: Temporal walk-off effects in HHG as a function of gas pressure and harmonic order. (a) The experimentally extracted attochirp for sidebands 14-22 at different background pressures in the generation chamber using the RABBITT technique. The pressures correspond to 1.5 µbar (green), 2.5 µbar (blue), 3.5 µbar (red) and 4.5 µbar (black). (b) The results of a numerical one-dimensional propagation model based on the wave vector mismatch between the generation pulse and the harmonics generated at pressures of 27 mbar (blue), 44 mbar (red) and 80 mbar (black). (Data taken from Paper **VI**.)

is very difficult to measure the exact pressure inside the gas cell, so the model utilizes the estimated phase-matching pressure. The anomaly for sideband 16 is due to a narrow resonance in argon. This is discussed in Paper **VII** and Section 6.1.2. The results of this study show that variations in the density of the generation medium may lead to a shift of the detected phase as the APT is delayed with respect to the probe field, which highlights the importance of having a stable source of APTs. Furthermore, when comparing the behavior of different systems, as discussed in the following section, an unstable source may misinterpreted as an intrinsic phase shift. Pressure instability in the detection medium is probably less of a problem in RABBITT measurements, as both the probe intensity and the gas density are usually at least 2 orders of magnitude lower than in the generation chamber[7].

Photo-ionization of Noble Gases

In the previous section, the impact of macroscopic effects on time delay measurements was discussed, but measurements of the complex part of the matrix element for various transitions, which was previously in-accessible in direct measurements, is a core interest of the attosecond community. The RABBITT technique provides access to the phase of two-photon transition matrix element, which depends strongly on the angular channels of both the intermediate and final states. Within the dipole approximation, which is generally valid for the NIR to XUV regime [163], the two-photon transition can be described by two consecutive single-photon transitions, which adheres to the dipole transition rules[8] illustrated in Figure 6.5 for s and p electrons. The two-photon

[7] In these measurements, the gas in the interaction chamber of the MBES is usually kept at a background pressure of around 10^{-6} to 10^{-5} mbar using a continuous gas jet, while the pressure in the generation chamber is maintained at around 10^{-3} mbar using a pulsed gas jet.

[8] Under the single-active-electron approximation the rules are $\Delta l = \pm 1, \Delta m = \{0, \pm 1\}$ [88].

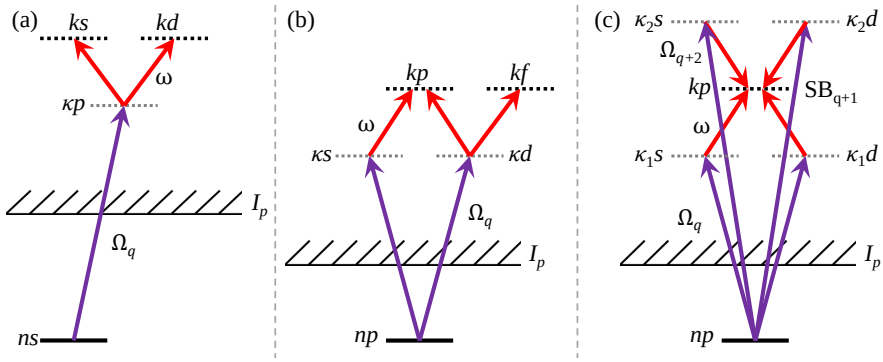

Figure 6.5: (a,b) Angular ionization channels for two-photon transitions of (a) ns and (b) np electrons. κ denotes intermediate continuum states, while k denotes the final continuum states. (c) RABBITT scheme with multiple intermediate angular channels with the same final channel.

transition may be written in closed form as [164]

$$M_q(k) = -i\mathcal{E}_\omega \mathcal{E}_\Omega \lim_{E\to 0^+} \sum_{\kappa\ell'}^{f} \frac{\langle k\ell'' | \hat{d} | \kappa\ell' \rangle \langle \kappa\ell' | \hat{d} | g\ell \rangle}{E_g + \Omega - E_{\kappa\ell'} + iE}, \tag{6.9}$$

where $\langle g|$ and $\langle k|$ denotes the initial and final states with angular channels ℓ and ℓ'', while $\langle \kappa|$ denotes all possible intermediate states with the corresponding angular channels ℓ'.

In the case of an s electron, the final states do not overlap, as shown in Figure 6.5 (a), so while the two angular channels of the outgoing electrons may be delayed with respect to each other, they do not interfere, and their phases can be handled separately. The complexity of the problem increases significantly already for p electrons where several intermediate channels lead to the same final channel, as shown schematically in Figure 6.5 (b). In this case, the various intermediate channels will acquire different phases, and the final electron wave-packet will thus contain information from both ionization pathways, which will interfere, as illustrated for the case of RABBITT in Figure 6.5 (c). The strength of the modulation depends on the branching ratio of the various single-photon transitions.

The impact of angular channels on the photo-ionization time delays for helium, argon and neon were investigated in the present work (Paper **V**). The stabilized interferometer was required as the experiment consisted of repeating the same measurements a number of times and extracting the relative phase shift between the different atoms. Time delays in argon have been extensively studied previously by the Lund group [5, 31], so argon was used as the reference gas, as shown in Figure 6.6 (a). The measured relative time delays are shown in Figure 6.6 (b).

In the ideal case, an angularly resolved photo-electron emission spectroscopy tool[9] could be used to acquire time delays, as the angular channels of the final states can be separated. However, all the time-delay measurements presented in Paper **V** were

[9]Such as a velocity mapping imaging spectrometer (VMIS) [165] or a cold target recoil ion momentum spectrometer (COLTRIMS) [166].

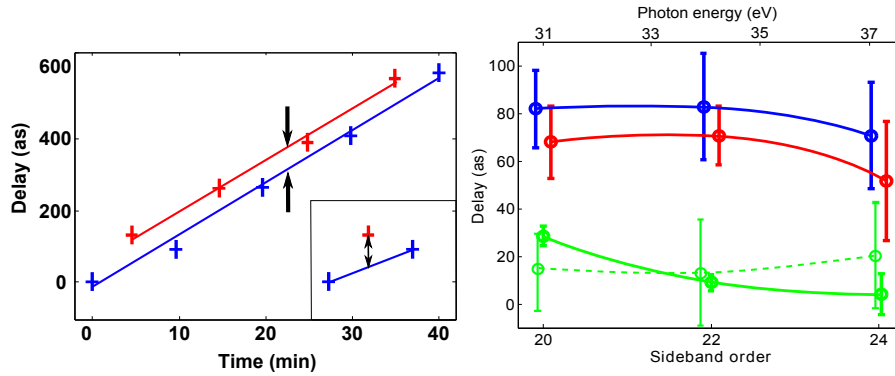

Figure 6.6: (a) Uncompensated temporal drift of the original setup measured by comparing the phase of consecutive RABBITT scans in argon and neon. The curves show the extracted phase of sideband 22 for argon (blue) and neon (red) for a number of consecutive scans. (b)Comparison between the measured photo-ionization time delays between Ar–He (green), Ar–Ne (red) and Ne–He (blue). These figures were reproduced from Paper **V**.

conducted using an angularly integrated TOF with a 2π collection angle, as described in Section 6.1.2. The angular information is therefore embedded in the experimental data, and a number of theoretical models were tested against the measurements.

Paper **V** was published back-to-back in J. Phys. B. with a similar study carried out by DiMauro's group [167]. Direct comparisons were made between different gases in the present measurements, while the study presented in reference [167] relied on theory to extract the relative shifts. Their study also covered a much wider photo-electron energy range than that reported in Paper **V**.

Recently the U. Keller group have compared the photo-ionization time delays between argon and neon in the same spectral regime as in Paper **V** using the streaking method with coincidence detection using a mixture of argon and neon gas inside a COLTRIMS [159, 168]. Their results indicated a slightly shorter relative time delay between the two gases, than in the RABBITT measurements presented in Paper **V**.

Photo-ionization Near an Autoionizing Level

In the preceding sections, systems where photo-ionization is dominated by ionization of the outermost valence electron were investigated. However, as discussed in Section 3.2.3, the various electrons of an atom couple to each other. This occurs also in two-photon ionization, in particular, near resonances. In the study presented in Paper **VII** we investigated how the phase of the $3s^{-1}4p$ Fano resonance in argon varies as a function of energy. The RABBITT technique, in principle, probes the average phase of a sideband, so in order to measure the phase shift across the resonance the tunability of the laser system was applied. As demonstrated in Figure 6.7 changing the carrier frequency of the laser allows us to change the central frequency of the various harmonics, which consequently means that we can tune the energy of the sidebands as well. When the laser system is tuned to a carrier wavelength of 780 nm, HH17 spectrally overlaps with the resonance energy as can be observed in right hand side of the figure.

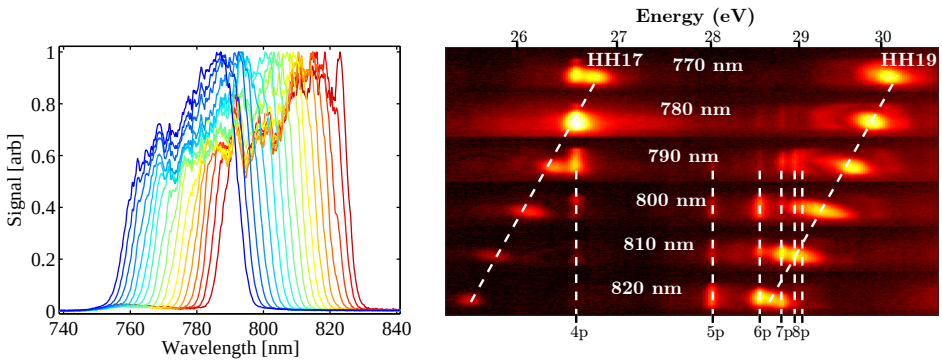

Figure 6.7: Left: Tunability of the spectral bandwidth of the 1 kHz laser. The various colors represent different settings of the two Dazzlers in the laser chain (see Section 2.2.1.). Right: HHG spectra for generation in argon at about 30 eV for various tunabilities of the laser system. The harmonic spectra were measured using the imaging spectrometer presented in Section 4.1.

Tuning the driving laser wavelength affects both the microscopic response and the macroscopic response in HHG, this leads to a change in both the GD and GDD of the attosecond pulse. In addition to the changed dispersion of the pulses, the ionization rate inside the generation medium is changed, which causes a minor change in the blue-shift of the harmonics. Proper care therefore has to be taken when comparing the RABBITT spectrograms for different carrier wavelengths.

When solving the Schrödinger equation for two-photon ionization near the Fano resonance in argon using angular basis functions, two intermediate continua channels[10] arise that couple with the autoionizing resonance as illustrated in Figure 6.8 (a). The two channels have different coupling strength with the bound state, while the excitation of the two channels depend on the branching ratio of the system [169, 170]. The various intermediate channels through the resonance lead to three different final state channels, which should be incoherently added up to describe the full two-photon transition. In order to gain insight into the physics of the system, a rotation of the basis functions were performed following the approach given in the second part of Fano's original work (reference [90]). Using the rotated basis functions, the system can be described by two intermediate channels, where the first channel consists of a continuum which interacts the bound state, while the other channel consists of continuum channel which does not interact with the bound state. Following the notation of Section 3.2.3 the total ionization cross-section relative to the unperturbed continuum can be written as:

$$\frac{\sigma_{\text{pert}}}{\sigma_{\text{unpert}}} = |\alpha|^2 \left(1 - \frac{1}{1+\epsilon^2} + q\frac{q+2\epsilon}{\epsilon^2+1}\right) + |\beta|^2 \left(1 - \frac{1}{1+\epsilon^2}\right), \tag{6.10}$$

[10] The $3p^{-1}\kappa s$ and $3p^{-1}\kappa d$ channels.

where α and β depends on the branching ratio between the excitation of the interacting continuum and the non-interacting continuum.

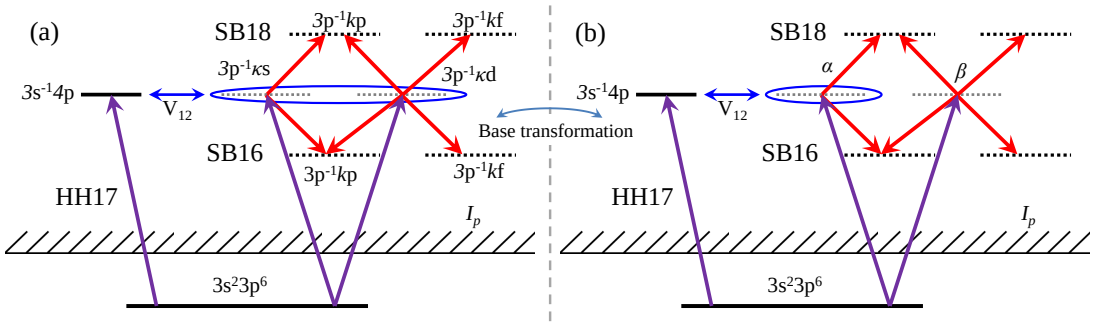

Figure 6.8: Left: Angular channels for the Argon $3s^{-1}4p$ Fano resonance. Two different intermediate channels that both couple two a bound state lead to a complicated measurement of the final two-photon transition. Right: The Fano resonance represented in a rotated basis system, where the intermediate channels can be separated in a channel that interacts with the bound state, and one that does not. The rotated basis function leads to simpler interpretation of the two-photon transition element as described in the text.

The complex amplitude of the relative two-photon transition matrix element is also modified by the non-interacting channel, and it can be written as:

$$M_{\text{total}} = M_{\text{interacting}} \frac{q+\epsilon}{i+\epsilon} + M_{\text{non-interacting}}, \tag{6.11}$$

where $M_{\text{interacting}}$ and $M_{\text{non-interacting}}$ are the matrix elements of the two channels, respectively. Inspection of Equation (6.11) reveals that the non-interacting continuum leads to a deviation from the phase shift of π caused by a single channel Fano resonance. This deviation depends on the branching ratio of the two channels. For the article the branching ratios were calculated using *ab-initio* calculations [171].

A final complexity in comparing the experiment with theory arises from the finite widths of the sidebands alongside the spectral resolution of the electron spectrometer, which lead to a smoothing of the measured phase shift of the resonance. The full theoretical calculations presented in the paper take all of these effects into account. The sidebands of the measured RABBITT trace is shown in the left hand side of Figure 6.9, while the right hand side presents the results of a numerical model by the group of F. Martin [172]. The theoretical model clearly reproduces the experiment fairly well, and it was found that $q = 0.25$, in accordance with earlier work [170], and that the phase shift is around 0.6 rad.

This experiments presents the first published measurement of a phase shift of a Fano resonance. However, unpublished work by the group of P. Salières uses the phase extraction of Fano resonance in helium to examine the temporal structure of the excitation of an autoionizing resonance [173]. In that work the measurement was performed in a technique they call Rainbow RABBITT [173]. The Rainbow RABBITT utilizes broadband harmonics together with narrow-band NIR probe field in an electron spectrometer with high spectral resolution, this allows for spectrally resolved phase extraction across a narrowband resonance without tuning the wavelength of the carrier wave.

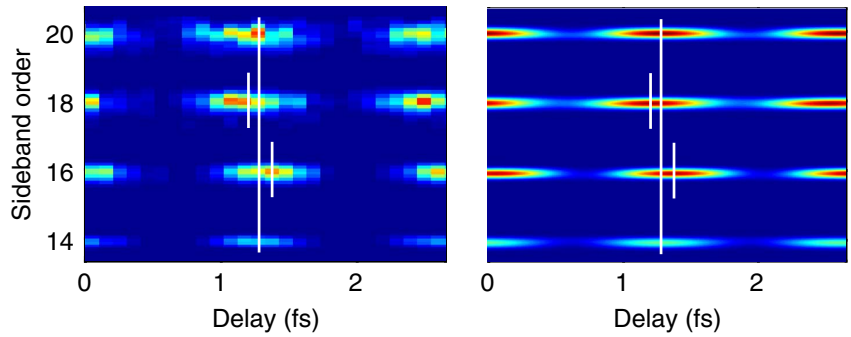

Figure 6.9: Left: Experimental sidebands from the RABBITT trace for two-photon ionization of Ar using a driving laser with carrier wavelength of 780 nm and its high-order harmonics. Right: Corresponding numerical calculation of the RABBITT trace of the sidebands. The calculations utilizes a resonant two-photon ionization model, which is described in details in [172], and is outlined in the text. The figure was reused from Paper **VII**.

6.2 Attosecond Transient Absorption

So far, this chapter has been concerned with observations of electrons in studies of light matter interactions on the attosecond timescale for the purpose of determining time delays. However, a recent trend within the field of attosecond science is to study the XUV light transmitted through a medium under the presence of a strong laser field rather than the emitted electrons [174–180]. The technique, which is called attosecond transient absorption spectroscopy (ATAS), is an extension of femtosecond transient absorption used in femtochemistry [181], into the time domain of electron motion. Femtosecond transient absorption was first demonstrated in 1988 by Mathies *et al.* [182], and has been an essential tool for probing and understanding dynamic configurational changes in, for example, core-shell electronic structures of molecules [183]. Femtosecond transient absorption was extended to include table-top HHG sources as described in [184], and into the attosecond regime in 2010 by Goulielmakis *et al.* as described in [174], who demonstrated the possibility of to measure the electronic evolution of the system.

Photon spectroscopy provides complementary information to photo-electron spectroscopy about light–matter interactions. Photo-electron spectroscopy obviously requires ionization of the system, while this is not necessary for photon absorption spectroscopy. In the previously discussed example of a Fano resonance of argon, the destructive interference between a closed channel and two open channels led to a minimum in the photo-ionization probability. The same resonance was studied using ATAS in 2010 by Wang *et al.* [175]. In the ATAS experiment, it was revealed that if the dressing field is sufficiently strong, it is possible to change the spectral lineshape of the Fano profile into a Lorentzian profile through phase modulation of the electron wave packet. This concept was further developed by Ott. *et al.* [176, 185], who demonstrated that a precisely chosen dressing field makes it possible to modify the spectral–profile back and forth between Lorentzian and Fano profiles. These experiments of [175, 176, 185] can be described by a phenomenon called free induction decay (FID), the details of which will be discussed in Section 6.2.1.

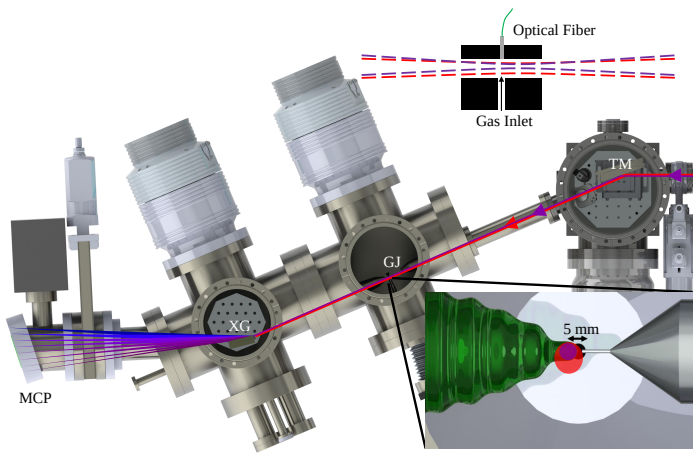

Figure 6.10: Schematic overview of the transient absorption chamber. inLund GJ, gas jet; MCP, micro-channel plate; TM, toroidal mirror; XG, XUV grating.

Transient absorption chamber

A transient absorption chamber was constructed as part of this work in order to perform ATAS-typed experiments. A schematic of the setup is shown in Figure 6.10. Light pulses delivered by the new attosecond interferometer presented in Chapter 5 are refocused into the chamber by a toroidal mirror. The interaction cell consists of a gas cell, which is very similar to the one in the generation chamber[11]. The main difference is that an optical fiber can be mounted perpendicular to the direction of propagation of the laser pulses on this gas cell. The optical fiber is used for observations of fluorescence in the VIS–NIR regime. In addition, the fiber provides the possibility to find the temporal overlap between the pump and probe arm at the point of interaction through the use of spectral interferometry[12]. The XUV spectrum transmitted after the interaction region is measured using the imaging spectrometer described in Section 4.1. The transient absorption chamber is separated from both the XUV spectrometer and the toroidal mirror chamber by blind flanges with 5 mm diameter holes for transmission of the light pulses. These small holes allow for differential pumping between the chambers. For all transient absorption experiments described in this thesis the chamber was docked behind the new attosecond interferometer described in Section 5.2.

6.2.1 Free Induction Decay

An ensemble of atoms exposed to a short, coherent light pulse will respond collectively. If the frequency of the light roughly corresponds to the frequency of a bound-to-bound

[11] GR020, Attotech. In the drawing the gas cell is shown as a gas jet in the cross-section view, this is merely for visualization purposes.

[12] Strictly speaking, the method only provides the temporal overlap between the two NIR pulses (the probe and the NIR pulse used for HHG before removal by the motorized iris and filters). However, since the XUV is phase-locked, but slightly delayed, to the pump NIR this provides a good approximation to the real temporal overlap between the XUV–NIR pulses.

state transition in the atoms, some of the atoms will be excited. The system may therefore be thought of as a series of oscillating dipoles. As the atoms are coherently excited by the same pulse the dipoles will be phase locked, and they may continue to oscillate coherently for a time, T_{FID}, which is comparable to the radiative lifetime of the upper state. If the excitation pulse is shorter than the coherence time the dipole will still emit light after the excitation pulse has passed. In this case the resulting forward-scattered light is known as optical free induction decay (or simply free induction decay) (FID) [186, 187]. This forward-scattered light has the same spatial properties as the excitation pulse, but the phase of the emission is shifted by π. The overlap between the two fields will therefore yield the normal absorption spectrum observed in optical spectroscopy.

FID was originally proposed by Bloch in 1946 in terms of a "spin echo" of nuclear magnetic resonances subjected to a strong magnetic field [188]. Bloch predicted that the spin of a nuclear magnetic resonance subjected to a short strong magnetic field will precess and a create a superposition state with a total relaxation time, which may be in anywhere in the range of microseconds to several seconds depending on the material. If the excitation pulse is sufficiently short, the superposition state can cause a nuclear induction field that can be measured after the excitation pulse. The prediction of Bloch was observed 4 years later by Hahn [189], and have since been instrumental in the development of many applications. The most commonly known direct application of Hahn's and Bloch's work is the magnetic resonance imaging (MRI) technique used in most hospitals nowadays. MRI relies on high-precision measurements of the relaxation time of the magnetic induction. As the relaxation time is highly compound selective the method allows for discrimination between tumors and normal tissue [190]. Reference [191] provides an excellent historical overview of the development of MRI.

In contrast to the early work on FID, the present work (Paper **IX**) is concerned with FID in the optical to the XUV regime using coherent laser sources. FID is usually described through a two-level system coupled with Maxwell's equations known as the Maxwell–Bloch formalism [187]. Mathematically, a two-level system can be written:

$$|\Psi\rangle = \left(\cos\frac{\theta}{2}|g\rangle + \mathrm{e}^{i\phi}\sin\frac{\theta}{2}|e\rangle\right)\mathrm{e}^{i\phi_0}, \tag{6.12}$$

where $|g\rangle$ and $|e\rangle$ denotes the ground state and excited state, respectively. θ and ϕ are real numbers, where θ is a measure of the relative population of the two states and ϕ is a measure of their relative phase. Finally, ϕ_0 is a global phase, which can be ignored in a true two-level system, as it does not impact the physics. In order to derive the Maxwell–Bloch formalism the density operator $\hat{\sigma}$ is often introduced as:

$$\hat{\sigma} = \Sigma_i p_i |\psi_i\rangle\langle\psi_i|, \tag{6.13}$$

where $|\psi_i\rangle$ is a set of basis vectors and p_i is their corresponding populations with $\Sigma_i p_i = 1$. The time-evolution of the density operator is given by:

$$\frac{\mathrm{d}\hat{\sigma}}{\mathrm{d}t} = \frac{1}{i\hbar}\left[\hat{H},\hat{\sigma}\right], \tag{6.14}$$

where the brackets denotes the commutator between the Hamiltonian, $\hat{H}$, of the system and the density operator. The Hamiltonian for a two-level system interacting

with a quasi-resonant electromagnetic field with frequency ω and strength $\mathcal{E}_0$ can be written in the Length gauge explicitly as:

$$\hat{H} = \hbar\omega_0 \left|e\right\rangle \left\langle e\right| - e\hat{z}\mathcal{E}_0 \cos\left(\omega t\right), \tag{6.15}$$

where ω_0 denotes the difference in angular frequency between the two states. The detuning between the frequency of the field and the frequency of the transition is denoted $\Delta = \omega - \omega_0$. Inserting Equation (6.15) into Equation (6.14), and using Equation (6.13) yields a set of coupled equations known as the Bloch equations:

$$\frac{\mathrm{d}\sigma_{ee}}{\mathrm{d}t} = i\Omega\cos\left(\omega t\right)\left[\sigma_{eg} - \sigma_{ge}\right], \tag{6.16a}$$

$$\frac{\mathrm{d}\sigma_{gg}}{\mathrm{d}t} = -i\Omega\cos\left(\omega t\right)\left[\sigma_{eg} - \sigma_{ge}\right], \tag{6.16b}$$

$$\frac{\mathrm{d}\sigma_{ge}}{\mathrm{d}t} = i\omega_0\sigma_{ge} - i\Omega\cos\left(\omega t\right)\left[\sigma_{ee} - \sigma_{gg}\right], \tag{6.16c}$$

where $\sigma_{ij} \equiv \left\langle i\right| \hat{\sigma} \left|j\right\rangle$, and the Rabi frequency $\Omega \equiv \left\langle e\right|\hat{z}\left|g\right\rangle / \hbar\mathcal{E}_0 \cos\left(\omega t\right) \equiv \Omega_{\mathrm{re}} + i\Omega_{\mathrm{im}}$. The Bloch equations can be represented geometrical through the introduction of a quantity known as the Bloch vector, $\mathbf{R} \equiv (u, v, w)$ [192]. The components of the vector are given by:

$$u = \left(\sigma_{ge} + \sigma_{eg}\right), \tag{6.17a}$$

$$v = i\left(\sigma_{ge} - \sigma_{eg}\right), \tag{6.17b}$$

$$w = \left(\sigma_{gg} - \sigma_{ee}\right). \tag{6.17c}$$

The first two components describe the coherence between the two levels, while the third component describes the population. The vector will have a length of 1, if the system is in a pure superposition state. In this case the vector will point to the surface of sphere known as the Bloch sphere as depicted in Figure 6.11, if the system is one of the eigenstates of the system the vector will point upwards or downwards along the w-axis accordingly. When the system is in a mixed state the total coherence of the system is not known, thus the Bloch vector is shorter than 1. As the two states have different energies u and v will depend on time, and the Bloch vector will precess around the w axis, if decoherence effects and decays are ignored. For visualization reasons it is therefore sometimes easier to use a rotating reference frame, which takes the trivial phase-evolution between the two states into account. In the rotating reference frame the time-evolution of the Bloch vector in an external field is:

$$\frac{\partial\tilde{\mathbf{R}}}{\partial t} = \mathbf{\Omega} \times \tilde{\mathbf{R}}, \tag{6.18}$$

where $\tilde{\mathbf{R}}$ denotes the Bloch vector in the rotating reference frame and $\mathbf{\Omega} \equiv \{-\Omega_{\mathrm{re}}, \Omega_{\mathrm{im}}, \Delta\}$. As previously discussed the system can be affected by external conditions such as collisions. These changes can be categories into two classes: effects that causes depopulation of the upper state, which occurs at a characteristic time T_1, and effects that causes the coherence of the system to be lost, which occurs at a characteristic time T_2. Including these two groups of effects the time-evolution of the Bloch vector can be written [193]:

$$\frac{\partial\tilde{\mathbf{R}}}{\partial t} = \mathbf{\Omega} \times \tilde{\mathbf{R}} - \left(\frac{1}{T_2}u, \frac{1}{T_2}v, \frac{1}{T_1}\left(w - w_0\right)\right), \tag{6.19}$$

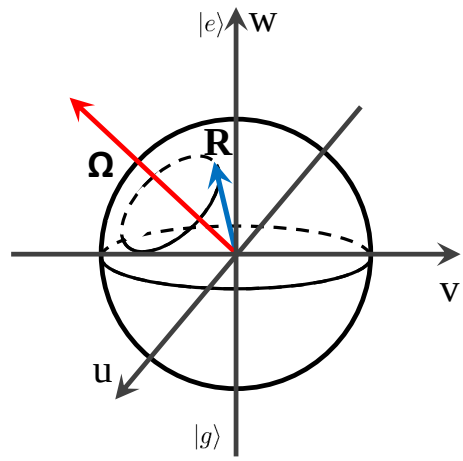

Figure 6.11: Illustration of the Bloch sphere. The state of a pure two-level system is represented by the Bloch vector R from the origin to the surface of the sphere. A mixed state, for which the coherence is less known, can be represented with by a Bloch vector inside the surface of the sphere. Application of a non-resonant field with a Rabi frequency Ω causes the Bloch vector precess around the rotation vector $\mathbf{\Omega}$.

where w_0 is the thermal equilibrium state. In the present case of transitions in the XUV: $w_0 \approx -1$ according to the Maxwell–Boltzmann distribution. This representation of the time-evolution of the Bloch vector explains why T_1 is often called the longitudinal relaxation time and T_2 the transverse relaxation time.

The total electromagnetic field interacting with the system can be described as a superposition field between the driving field $\mathcal{E}_{\text{Las}}$, an optical nutation field $\mathcal{E}_{\text{ON}}$, and a free induction field $\mathcal{E}_{\text{FID}}$. In other words the total field is given by:

$$\mathcal{E} = \mathcal{E}_{\text{Las}} + \mathcal{E}_{\text{ON}} + \mathcal{E}_{\text{FID}}. \tag{6.20}$$

Optical nutation describes atoms or molecules, which are far off resonance with the driving field, and which are suddenly shifted into resonance by an appropriate mechanism, for example, an applied Stark field. In the case of ATAS experiments optical nutation may occur at temporal overlap between the pump and probe fields. The addition of the optical nutation field complicates the analysis of an experiment. This is one of the reasons the measurements presented in Paper **IX** were performed after temporal overlap.

The Bloch equations are traditionally coupled with Maxwell's equations in an one-dimensional propagation model, where the Bloch equations are used as a source term. This was first performed by Scully and co-workers [187]. Scully *et al.*, used this method together with the approximation $|\mathcal{E}_{\text{Las}}| >> |\mathcal{E}_{\text{On}}| + |\mathcal{E}_{\text{FID}}|$ to derive an analytical expression for the first optical FID measurement by Brewer and Shoemaker presented in reference [186]. The experiment consisted of an ensemble of atoms subjected to a continuous wave laser. At a specific time a constant Stark field was applied, which changed the frequency of the FID signal to a different frequency than that of the laser, thus creating a background free measurement of the FID emission. The full analytical expression is given in reference [187], while here only the time dependence of the signal

is given:

$$\mathcal{E}_{\mathrm{FID}} \propto \exp\left\{-\left[\frac{1}{T_2}+\left(\frac{T_1}{T_2}\mathcal{E}_0^2+\frac{1}{T_2^2}\right)^{1/2}\right]t\right\} \equiv e^{-t/\tau_{\mathrm{FID}}}. \tag{6.21}$$

It is evident from Equation (6.21) that both T_1 and T_2 play important roles in the decay time, τ_{FID}, of FID signals. As the FID signal is generated by N phase-locked dipoles the intensity of the light scales quadratically with the ensemble size, *i.e.,*

$$S_{\mathrm{FID}} \propto N^2. \tag{6.22}$$

The analysis above becomes more complicated in a dense gas as the FID signal may excite other atoms, which creates a secondary FID signal, which again may excite other atoms and so forth. Each sequential FID signal is phase shifted by π with respect to the previous FID signal. For experiments concerning excitation with attosecond pulses, the sequential FID signal can be described as resonant pulse propagation, which leads to a temporal tail of XUV light with frequencies corresponding to transitions frequencies [178, 194]. In addition to the resonant pulse propagation effect other effects may occur in a high density gas such as superradiance [195] or superfluorescence [196]. Generally, the terminology of these effects is very much debated, and a number of different definitions exist [187, 195–199]. In the present work the following definitions will be used.

Superradiance may occur when a system is excited by a coherent pulse into an entangled state, which has a macroscopic dipole moment. When the ensemble decays a superradiant pulse is emitted, this effect is different from FID as the system is entangled, such that decay of one atom affects the others. Under certain conditions a FID signal may therefore be superradient, but it does not necessarily has to be. Two types of superradiance exist, the first one called Dicke superradiance may occur when the wavelength of the photon is much larger than the interatomic separation, while the second may occur when the ensemble is much larger than the wavelength of the photon [199].

Superfluorescence may occur when an atom within an ensemble of uncorrelated excited atoms decays to the ground state by spontaneous emission of a photon, which then causes stimulated emission of other atoms, thus creating a buildup of a macroscopic pulse. Due to the coherent nature of both superradiance and superfluorescence the macroscopic buildup of both effects scale quadratically with the number density of excited atoms in the ensemble, hence a measurement of the time integrated intensity of all effects will be indistinguishable, if the pressure is the varied parameter. However, as superfluorescence is started by spontaneous emission of a randomly oriented dipole it may occur in any direction, thus when averaged over a large number of pulses the superfluorescent emission should be isotropic, this was not observed in the experiments described in the next section, so the impact of superfluorescence should be minimal in our experiments. Discrimination between normal FID and superradient FID should be achieved by performing a measurement of the decay rate of the signal. Measurement of the decay times were not in the scope of the present work, thus we were unable to determine whether or not the controlled FID described below was subjected to superradiance.

6.2.2 Controlled Free Induction Decay

The work presented in Paper **IX** was initially inspired by work presented by Chini and co-workers presented in reference [200]. In that study the experiment consisted of HHG from a few-cycle pulse in argon. The study was focused on what happens at photon energies near the transition energies between the ground state and the bound-state manifold below the first ionization potential. It was observed by Chini *et al.* that at photon energies corresponding to these transition energies the XUV light was enhanced, creating a series of narrowband structures in the near-continuum XUV spectral profile. These narrowband structures showed a similar, but slightly larger, divergence angle than the remaining XUV light that was produced in the experiment (through HHG). Repeating the experiment in our laboratory with few-cycle pulses[13] [see Figure 6.12 (a)] showed similar behavior when transmitted through a second gas cell filled with roughly ten times higher pressure of argon [see Figure 6.12 (b)]. Careful investigation of the generated XUV spectrum [Figure 6.12 (a)] directly reveals some narrowband structures, however, they are much more pronounced after transmission through the second cell. The bandwidth of the structures indicate that the that the XUV light of these frequencies are significantly longer than the few-cycle driving laser. The results here are in full agreement with the results presented by Chini *et al.,* which also showed that the signal near the resonances was more favorable at higher pressures than the phase-matching pressure for HHG.

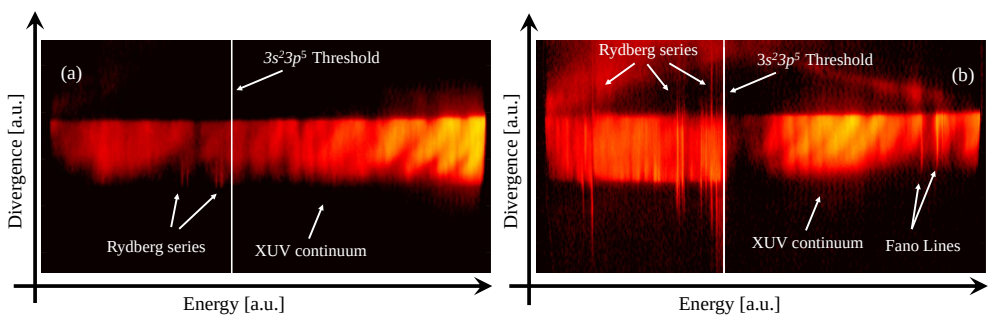

Figure 6.12: (a) Spatial–spectral profile of the XUV light produced by HHG in argon by a 4 fs pulse. (b) Spatial–spectral profile of the XUV light from (a) after transmission through a gas cell filled with high-pressure argon. The exact pressures in the cells are difficult to estimate, but the background pressure in the generation chamber [(a)] was 1.5 µbar, while the background pressure in the transient absorption chamber [(b)] was 20 µbar. The color scales in (a) and (b) are not the same.

In order to further investigate the narrowband structures in a pump-probe scheme we turned to the long driving pulses supplied directly by the laser. The carrier wavelength of the pulses was tuned, so that the photon energies of particular high-order harmonics would overlap with specific transitions in argon. Paper **IX** presents two sets of experiments of narrowband photon energies resonances near both the $3s^23p^5$ continuum and the $3s^13p^6$ continuum.

For addressing states near the $3s^23p^5$ continuum the carrier wavelength was set to 780 nm, while it was set to 820 nm for addressing states near the $3s^13p^6$. The

[13] Those that were used for the NOG experiment described in Section 4.2.1 and Paper **VIII**.

attosecond interferometer was aligned such that the pump and probe pulses would co-propagate after recombination. However, with a small offset in space, *i.e.,* in a non-concentric co-propagating geometry. Figure 6.13 presents the type of the spatial–spectral profile that was observed as a function of pump-probe delay τ.

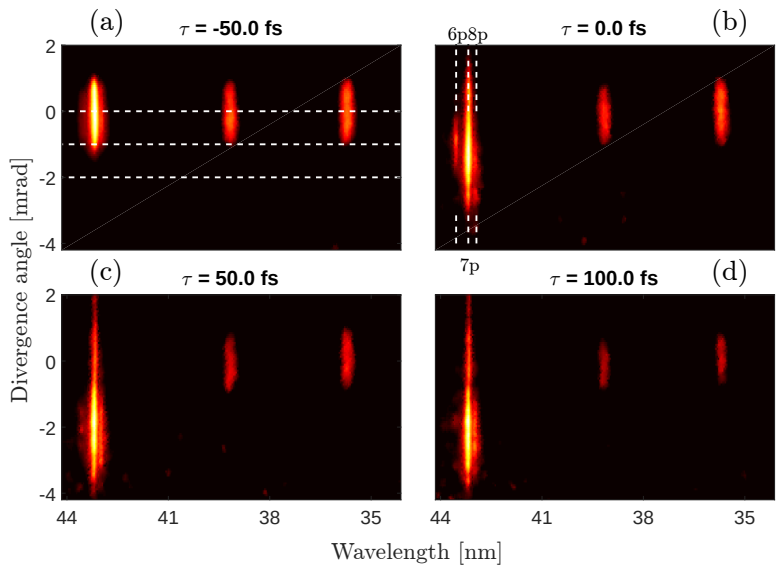

Figure 6.13: Spatial–spectral profile of XUV light produced in argon by HHG of a 30 fs pulse with a carrier wavelength of 820 nm and then subsequently sent through a argon filled gas cell as a function of pump-probe delay τ. Negative delays correspond to the NIR probe pulse precedes the XUV pulse. The horizontal dashed lines in (a) indicate three different divergence angles, while the vertical dashed lines in (b) indicate the XUV photon energies corresponding to the $3s^2 3p^6 \rightarrow 3s^1 3p^6 n(s,d)$, $n = \{6, 7, 8\}$ transitions. This figure was reproduced from Paper **IX**.

When the NIR precedes the XUV pulse by 50 fs [Figure 6.13 (a)] the XUV spectrum would resemble a simple absorption spectrum. However, at photon energies corresponding to bound state transition energies showed the same narrowband structures in the spatial–spectral profile of the transmitted XUV light as observed with short driving pulses. For example, the structures below the first ionization potential showed a larger divergence than the excitation pulse, while at photon energies near the resonances embedded in the continuum the narrowband structures had exactly the same divergence angle as the divergence angle of the XUV pump pulse [see Figure 6.12 (b).]. Going towards temporal overlap between the pump and probe pulse [Figure 6.13 (b)], the XUV light near the structures start to become deflected in a different angle than the incident XUV light. The deflection angle of the narrowband XUV light was increased as the probe pulse was further delayed with respect to the pump pulse, until a saturation occurs 30-40 fs after temporal overlap. At larger delays the deflection angle remained the same as shown in Figure 6.13 (c) and (d), however, the intensity of the deflected beam was slightly reduced. It rapidly became clear that the deflection of the XUV beam was dependent on the peak intensity of the NIR pulse, the pump-probe

delay and the spatial overlap of beams at the foci of the beams inside the transient absorption chamber.

To my knowledge no-one had previously predicted nor observed this phenomenon, so initially the outcome of the experiments came as a large surprise. It was obvious from the beginning that observation was due to a wave front rotation, but the origin of this rotation was not clear and a large number of different explanations were proposed. It was not until the idea of spatially dependent perturbed FID, described in the following and in Paper **IX**, a feasible explanation was put forward.

The XUV pulse creates a coherent excitation of the ensemble, which, in the case of narrowband harmonics, can be described as a two level system, which in turn can be described using the Maxwell–Bloch formalism. When the NIR significantly precedes the XUV excitation pulse the system behaves as unperturbed FID and the phase evolution between the ground state and the excited state is given by the energy difference between the two levels as described above. However, if the NIR laser pulse arrives after the XUV pulse, but within the decay time of FID signal, the system is perturbed. The perturbation results in a repulsion of the two energy levels through the Stark effect, which then results in a phase shift. Mathematically the phase shift induced by a DC-Stark effect can be calculated using second-order perturbation theory as [133]:

$$\Delta\varphi_{\mathrm{Stark}} = \int \mathrm{d}t \frac{\Delta E_{\mathrm{Stark}}}{\hbar} = \int \mathrm{d}t \left(|\mathcal{E}_{\mathrm{IR}}|^2 \frac{|\langle e|e\mathbf{r}|g\rangle|^2}{E_{ge}} \right) /\hbar, \tag{6.23}$$

where $\mathcal{E}_{\mathrm{IR}}$ denotes the field strength of the Stark field, and denotes the field free transition energy. Generalizing the expression in Equation (6.23) to strong ultrashort pulses with multiple interacting states is a non-trivial task, which require solutions of the time-dependent Schrödinger equation. Coupling this solution with propagation effects can be done using the Maxwell–Schrödinger formalism [201] rather than the Maxwell–Bloch formalism. However, such solutions are complicated and better left for specialists. In Paper **IX** we apply a simplification offered by the SFA approximation, described in Section 3.2.1, instead of full quantum mechanical calculations. The highly excited states were treated as free electrons for which the phase modulation relative to the ground state induced by the laser field can be calculated using Equation (3.14), *i.e.,* as:

$$\Delta\Phi_{\mathrm{Laser}}(x,y,z) = \frac{\hbar}{2m_e} \int_t^\infty \mathrm{d}t' \left[2e\mathbf{A}(t',x,y,z) \cdot \mathbf{k} + (e\mathbf{A}(t',x,y,z)/\hbar)^2 \right]. \tag{6.24}$$

where t denotes the time of excitation of the wave packet, *i.e.,* the end of the XUV pulse. As clearly apparent from this expression the phase shift of the excited ensemble depends on the both the spatial and temporal overlap between the two light pulses. The spatial dependent phase shift leads to a wave front rotation. The change of wave vector can be approximated in one dimension by using the finite difference method as:

$$\Delta\mathbf{k} = \frac{\Delta\Phi}{\Delta x}\hat{\mathbf{x}} \equiv \frac{\Delta\varphi(x_2) - \Delta\varphi(x_1)}{x_2 - x_1}\hat{\mathbf{x}}, \tag{6.25}$$

where Δx denotes the separation between two points, x_1 and x_2, which are subjected by two different phase shifts of $\varphi(x_1)$ and $\varphi(x_2)$. Finally, $\hat{\mathbf{x}}$ is the unit vector for the direction of the change, which is perpendicular to the original propagation direction.

Since the wave vector change is perpendicular to the propagation direction we can calculate the angle of the wave front rotation as:

$$\theta = \arctan \frac{|\mathbf{\Delta k}|}{|\mathbf{k}_0|}. \tag{6.26}$$

Combining Equations (6.25) and (6.26) the required phase shift for a wave front rotation of an angle θ can be determined:

$$\Delta\Phi = \Delta x |\mathbf{k}_0| \tan\theta. \tag{6.27}$$

In Figure 6.14 the mechanism of controlled FID is phenomenologically shown.

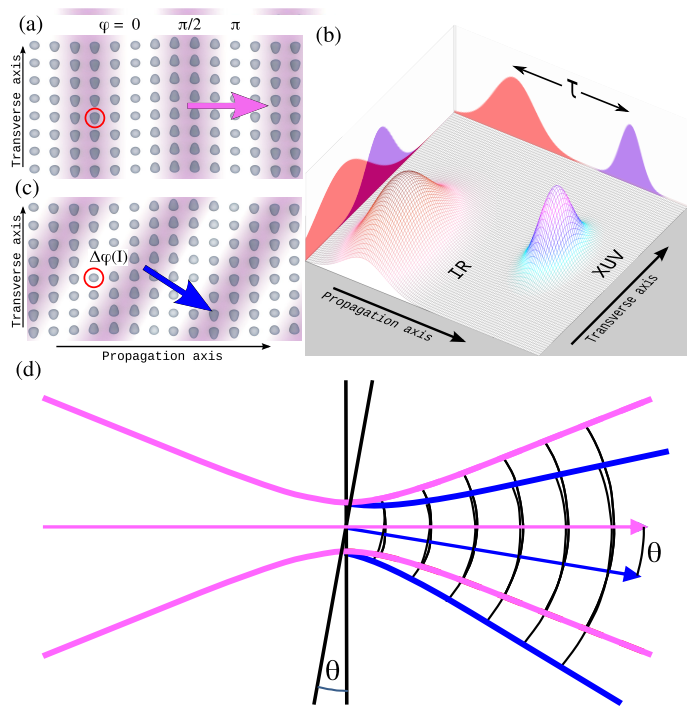

Figure 6.14: Overview of controlled FID. (a) The longitudinal and transverse dependent phase of the FID after excitation by the XUV pulse. Interference between the individual dipoles inside the ensemble leads to a macroscopic pulse propagating in the forward direction, as indicated by the purple arrow. (b) After a short time delay τ the ensemble is subjected to a strong non-concentric IR pulse. (c) The IR pulse induces a spatial dependent phase shift of the dipoles within the ensemble. (d) The spatial dependent phase shift causes the wave front of the macroscopic FID pulse to be changed by an angle of θ. This figure was reproduced from Paper **IX**.

Chapter 7

Summary and Outlook

Over the last decade or so attosecond science has attracted a great deal of attention due to the promise of high-resolution temporal and spectral spectroscopy of dynamic processes in various systems. Laser systems, capable of efficiently creating attosecond pulses through HHG have, until recently, been limited to Ti:sapphire based systems with driving wavelengths centered around 800 nm. It was often only possible to operate these laser systems in one configuration providing little flexibility. This meant that the harmonics, and thus the attosecond pulses, produced by these systems had poor tunability.

Several approaches to expanding the attosecond toolbox have been presented in this thesis. Improvements of the tunability of the attosecond sources, using high-order frequency up-conversion of a wavelength-tunable ti:sapphire laser system and a wavelength-tunable optical parametric amplifier, have been described. The increased tunability relies largely on recent advances in laser technology, and the work described here therefore depends on a number of prototype lasers. These highly tunable lasers and XUV sources were combined with a newly built high-stability attosecond interferometer intended for attosecond pump-probe experiments. The first attosecond experiment using this new interferometer was presented in this thesis. Before the advent of attosecond science, only the absolute square of dipole transition matrix elements were accessible experimentally. However, the complex matrix elements have recently become available for broadband ranges, although with limited spectral resolution [5]. In the first experiment with the new attosecond interferometer the complex two-photon transition matrix element near a Fano resonance was measured using the RABBITT technique together with the frequency tunability of the light sources.

Expanding the attosecond metrology to higher photon energies will improve our understanding of the dynamics of inner-shell electrons. In the Lund group work towards pump-probe experiments higher energies is already ongoing. In the first instance this is still conducted with 800 nm driving lasers at the original attosecond interferometer in a coincidence detection scheme between photo-ionization of an inner-valence shell electron followed by the sequential emission of an Auger electron [202]. Reference [202] also presents a plan to improve the stability of the original setup by implementing experiences gained from building the new setup in order to have two equally stable setups.

At even higher photon energies an inner-shell electron may be photo-ionized directly, and the system will relax through dynamic reorganization of the other electrons. In large atoms, the parameter space is too large to model with conventional computers, so experimental measurements are needed to complement theory in order to improve our understanding of core-shell ionization.

Accessing core-shell dynamics will probably require driving lasers with longer wavelengths. However, an unfortunate side effect of long-wavelength drivers is that the efficiency of harmonic generation, η, is significantly reduced, due to the combined effect of increased wave packet spreading and a reduction in the tunnel ionization rate.

The precise extent of this decrease is still being debated, but it is generally accepted that with the same intensity of the driving laser the scaling is on the order of $\eta \propto \{\lambda^{-5}$–$\lambda^{-7}\}$ [203, 204]. However, coherent combination of multiple CEP-locked pulses with different carrier wavelengths has recently been applied to overcome the otherwise unfavorable efficiency scaling [70].

Methods of making attosecond/XUV sources accessible to the broader community, and not only the highly specialized attosecond community, were also explored in this thesis. This was done by combining a simple to use HHG setup with a highly reliable commercial laser system. The development of this simplified setup proved to be very beneficial. In addition to the high reproducibility of the setup, the setup operated at high repetition rate, which allowed for detailed studies of the long trajectories involved in HHG. The ellipticity dependence of these trajectories were studied for the first time. The intensity dependent dipole phase of these trajectories were also quantified over a broadband range in the present work. Generally, these measurements each took less than 20 minutes, so the system should, in principle, allow for measurements of far more complex problems within reasonable time frames. For the present work the laser system used for these experiments was located in a collaborator's laboratory, however, due to the large success a similar laser has recently been installed locally in the group, and work towards a true prototype of a commercial HHG source will be interesting to follow.

Laser pulses in the optical to NIR regime in most laser laboratories are controlled by either acousto-optic modulators, electro-optic modulators [16], or spatial light modulators (SPM) [205]. These techniques, which have opened femtosecond control of the light, are generally limited to the to VIS/NIR regimes, due to absorption in the material. The development of controlled FID light presented in the last chapter will open the possibility of extending the control of IR light to a previously inaccessible spectral regime. One could imagine extending the control by adding a sequence of precisely timed short NIR laser pulses following the attosecond pulse. As described in the chapter the attosecond pulse is used to create a coherent superposition of the excited atoms, which emit light after the passing of the attosecond pulse. An intense NIR pulse could be used to control the spatial phase of the superposition, changing the phase-matching direction of the re-emitted FID light. The FID now emits light in a certain direction, which could be terminated by yet another NIR pulse, which changes the spatial phase of the FID for a second time. By precisely controlling the amplitude and phase of these two NIR pulses, by an appropriate technique, the control could be transferred to the XUV light. Adding additional laser pulses we may be able to turn on and off XUV emission in a controlled direction for short time-windows. As demonstrated in Paper **IX**, the control relies on a state with a long coherence time, so the photon energy of the controlled FID light could be adjusted by exploring different

atoms or molecules. This technique could develop into an opto-opto-modulator in the XUV. A well controlled XUV pulse would be beneficial for a number of applications. It has recently been demonstrated that using a single harmonic, which was produced through HHG, as a seed for the free-electron lasers is beneficial for the time structure of the light [113], so exactly controlled XUV seed light might be even better. Other possible applications include pump-probe experiments with multiple probe pulses for coherent control applications, and, for example, quantum computing typed experiments in the XUV. It will also be interesting to study the temporal structure of the controlled FID signal in order to determine if superradiance plays a role in process.

One of the goals with the present work was towards a quantum stroboscope driven by SIR pulses delivered by a TOPAS for rescattering experiments of photo-ionized electrons with high Ponderomotive energy. This included the construction of an appropriate attosecond pump-probe interferometer, which was described in Chapter 5. In addition, a quantum stroboscope requires breaking of the half-cycle temporal symmetry of HHG in order to produce XUV light only once per laser cycle [32], this is conventionally performed by driving the HHG process by the fundamental laser field coherently combined with its second harmonic [206]. For this purpose an achromatic inline two-color interferometer for SIR light pulses was developed [207]. The achromaticity of this interferometer will allow for the quantum stroboscope to easily be combined with the frequency tunability of the TOPAS, which may allow for the study of resonance effects in rescattering experiments.

The future of attosecond science require a strong joint development of experiments and theory. Going to progressively more complex systems experiments, such as inner-shell dynamics, require well-adjusted theories to understand the measurements. Similarly, theory without experiments to guide the development may be used to predict anything. To quote Johnny Von Neumann: "*With four parameters I can fit an elephant, and with five I can make him wiggle his trunk.*" [208, 209]

Comments on the papers

I **High-order harmonic generation using a high-repetition-rate turnkey laser**
In this paper we demonstrate HHG using a high repetition rate turnkey laser. I participated in the planning and building of the setup. I conducted the experiments together with the other students, wrote parts of the analysis software and gave comments to the manuscript.

II **Sub-cycle ionization dynamics revealed by trajectory-resolved, elliptically-driven high-order harmonic generation**
In this paper we investigate how ellipticity of the driving laser effects the HHG process. In addition we investigate the role of the short and long trajectories in the shaping of the spectrum in the vicinity of resonances. I lead the experimental work, performed the analysis and participated heavily in the interpretation and development of the model. However, I did not perform any of the numerical calculations. In addition I wrote the majority of the manuscript.

III **Spatially and spectrally resolved quantum path interference with chirped driving pulses**
In this paper we investigate the chirp dependence of HHG, with the emphasis on the impact on various quantum trajectories. In particular we determine dipole phase for the long trajectories for the first time. I conducted the experiments together with another student participated in the analysis and gave comments to the manuscript.

IV **Carrier-envelope phase-dependent high-order harmonic generation with a high-repetition-rate OPCPA system**
We study the carrier-envelope phase dependence of HHG. I participated in the building of the HHG setup which was used for this experiment, and took part in the initial measurements of HHG using the laser system.

V **Measurements of relative photoemission time delays in noble gas atoms**
In this paper we compare the photo-ionization time delays of the valence electrons of argon, helium and neon. Most of the experiments were performed prior to the upgrade of the 1 kHz laser system. I participated in the preparation for redoing the experiments after the upgrade, took part in some measurements and gave comments to the manuscript

VI **Attosecond pulse walk-off in high-order harmonic generation**
In this paper we measure a temporal walk-off effect of the XUV pulse in HHG as a function of gas pressure in the generation medium. The results are explained through a 1-D phase-matching model. I participated in the preparation for the experiments, took part in a number of the experimental measurements, discussions and gave comments to the manuscript.

VII **Spectral phase measurement of a Fano resonance using tunable attosecond pulses**
Using the tunability of the 1 kHz system, we were able to measure the phase variation across an autoionizing resonance in argon. The results are compared with ab initio calculations. I was responsible for building of the attosecond interferometer used for this experiment. I participated in discussions and gave comments to the manuscript.

VIII **Gating attosecond pulses in a noncollinear geometry**
We demonstrate experimentally a new gating technique for production of single attosecond pulses, called the non-collinear optical gating. I participated in the planning of the experimental parts, which occurred in the 1 kHz lab. I was responsible for building the HHG setup used for this experiment. I planned the implementation for the parts beyond the pulse compression into the HHG setup. I did not participate in the final data acquisition, but participated in discussions and gave comments to the manuscript.

IX **Controlled free induction decay in the extreme ultraviolet**
In this manuscript we demonstrate the spatial-phase control of free induction decay in the XUV through spatial dependent Ponderomotiveshift induced by a strong laser field. I participated in the planning of the experiments and conducted them together with another student. I also participated in the analysis and interpretation of the experimental data, and wrote major parts of the manuscript.

X **Photoemission electron microscopy of localized surface plasmons in silver nanostructures at telecommunication wavelengths**
In this paper we demonstrate spatially resolved photo electron emission from silver nanostructures using 1550 nm light produced by a TOPAS. I was responsible for the laser system and the TOPAS. I gave comments to the manuscript.

Acknowledgements

It has been a great pleasure and a privilege to be part of the Attosecond Physics Group at the Division of Atomic Physics at Lund University for the past six years. After spending the first year as a Master's student, I rejoined the group just over four and a half years ago as a PhD student. During this time I have shared numerous fun times with many people from the department; We have gone on skiing camps, conferences, Christmas markets in Lübeck, shared Jacuzzis, hot springs and saunas; and countless of lunches and dinners.

I have had the pleasure of working in numerous collaborative projects with experts from many different fields. I would like to thank everyone who contributed in some way to this work, and I apologize in advance for anyone I might have forgotten.

More than anyone, I owe my gratitude to my supervisor, Johan Mauritsson, for providing me with this wonderful opportunity and for his help and support throughout my PhD studies. You helped me focus on what is important, and your passion for spreading knowledge through teaching is inspiring. I would also like to extend a special thanks to the director of the group, Professor Anne L'Huillier, for accepting me into the group first as a Master's student and later as a PhD student, and for treating me like one of her own students throughout both periods. Her enthusiasm for physics is unprecedented and her scientific skills contribute greatly to the working atmosphere in the Attosecond Physics Group. I am also grateful to my co-supervisor Anders Persson, for his contributions to this work. I would also like to thank Cord Arnold, for his large contributions to this work.

Sharing an office with Cord Arnold, Diego Guénot, Hélène Coudert-Alteirac, Sylvain Maclot, Anne Harth, and Stefanos Carlström has been an amazingly fun experience over the years. I would particularly like to thank Diego for giving me the window seat without competition when Cord changed office, and for sharing his passion for RABBITT oscillations with me; Sylvain for adding sophistication to the group, Hélène for the Jazz events, and Stefanos for his numerical calculations for many of the projects I was involved in, and for his choir organization for the PhD parties.

I would like to thank all former and present members of the Attolab crew; Cord Arnold, Kathrin Klünder, Diego Guénot, Miguel Miranda, Marija Kotur, Mathieu Gisselbrecht, David Kroon, Maïté Louisy, Neven Ibrakovič, Marcus Isinger, Thomas Fordell, Stefan Plugmaker and Samuel Bengtsson.

I would especially like to thank my closest collaborator Samuel for the evenings and nights we spent working together on the TOPAS, as well as the Death Star, which was unfortunately overrun and renamed the Enterprise. Also, Neven for the ping-pong training during the time of my thesis writing. Diego, Marija and David

for the many nights of RABBITT scans; Cord, Miguel and Thomas, for sharing their limitless knowledge about ultrafast and nonlinear optics with me; and Mathieu for sharing his knowledge about everything.

Thanks to Erik Mårsell for his persistence with the TOPAS-PEEM article, and for his recommendations regarding beer and black metal.

Thanks to everyone involved in the Kemicentrum campaign: Eleonora Lorek, Stefanos Carlström, Jana Preclíková, Christoph Heyl, Donatas Zigmantas and David Paleček. It was a short, but very successful campaign. Special thanks to Eleonora for always(!) laughing at my jokes, even when noone else would, and for teaching me how to ski together with Marija.

To the MHz crew: Anne Harth, Arthur Losquin, Chen Guo, Yu-Chen Cheng and Erik Mårsell, I wish you the best of luck in overcoming the dragon and achieving attosecond pump-probe experiments in the near future. Especially, thanks to Chen and Anne for indulging me in many discussions about everything from lasers and HHG to attosecond time delays, PEEM and FID. Your passion for discussing and understanding things was very inspiring.

Thanks to everyone in the 10 Hz and ELI crews: Per Johnsson, Piotr Rudawski, Rafal Rakowski, Fernando Brizuela, Filippo Campi, Linnea Rading, Jörg Schwenke, Hélène Coudert-Alteirac, Jan Lahl, Hampus Nilsson, Bastian Manschwetus, Christoph Heyl, Byunghoon Kim and Sylvain Maclot, for the many interesting discussions during group meetings. I wish the current master students, Lana, Emma, Jasper, Chuang, Damien and Mallikarjun, the best of luck with their dissertations.

I would also like to thank our international collaborators, Professors Mette Gaarde and Kenneth J. Schafer for their theoretical support in numerous experiments and Emma Simpson, Paloma Matía-Hernando, Professor John Tisch and Professor Jon Marangos for the XUV seeding experiment.

Thanks to everyone involved with the OSA/SPIE Student Chapters for organizing many fun events; I will especially miss the annual laser tag tournament. Thanks also to the Fun in Fysicum team for organizing many competitions, in particular the multisport events, for the whole of the Department of Physics. Thanks to Diana Serrano for teaching me tennis, and Jenny Karlsson for the coffees and her tremendous work in the student chapters.

I would also like to thank Lars Rippe for preventing me from being the loudest person in the corridor and for teaching me three new words.

The amazing working environment at the Division of Atomic Physics is largely due to the organization and administration team. I would therefore also like to thank the Head of Division Professor Claes-Göran Wahlström, and current and former deputy heads Professors Stefan Kröll and Stefan Andersson-Engels. I would also like to thank the rest of the current and former administrative team, consisting of Anne Petersson Jungbeck, Bertil Hermansson, Camilla Nilsson, Harriet Lindahl, Jakob Testad, Minna Ramkull and Åke Johansson.

Finally, thanks to all my friends and my family for their support, and for reminding me of the world outside academia. I would especially like to thank my late father for his passion for learning new things, without his and my older brother's fascination with technology, I would probably never have been as fascinated with understanding technology and the world.

In short – Thank you to everyone!

References

1. M. Drescher *et al.*, Time-resolved atomic inner-shell spectroscopy. Nature **419**, 803-807 (2002).

2. A. L. Cavalieri *et al.*, Attosecond spectroscopy in condensed matter. Nature **449**, 1029 (2007).

3. M. Stockman *et al.*, Attosecond nanoplasmonic-field microscope. Nature Photonics **1**, 539-544 (2007).

4. M. Schultze *et al.*, Delay in Photoemission. Science **328**, 1658-1662 (2010).

5. K. Klünder *et al.*, Probing Single-Photon Ionization on the Attosecond Time Scale. Phys. Rev. Lett. **106**, 143002 (2011).

6. E. P. Månsson *et al.*, Double ionization probed on the attosecond timescale. Nature Physics **10**, 207-211 (2014).

7. F. Lepine, M. Y. Ivanov, and M. J. J. Vrakking, Attosecond molecular dynamics: fact or fiction?. Nature Photonics **8**, 195-204 (2014).

8. F. Calegari *et al.*, Ultrafast electron dynamics in phenylalanine initiated by attosecond pulses. Science **346**, 336–339 (2014).

9. A. P. Shimamura, Muybridge in motion: Travels in art, psychology and neurology. History of Photography **26**, 341-350 (2002).

10. H. E. Edgerton, Movie: Seeing the Unseen (1936). Viewable at http://edgerton-digital-collections.org/videos/hee-fv-038 .

11. H. Edgerton and J. Killian, *Flash!: Seeing the unseen by ultra high-speed photography* (C.T. Branford Co., ASIN: B0000CJ034, 1954).

12. T. H. Maiman, Stimulated Optical Radiation in Ruby. Nature **187**, 493-494 (1960).

13. K. Nakagawa *et al.*, Sequentially timed all-optical mapping photography (STAMP). Nature Photonics **8**, 695-700 (2014).

14. https://pixabay.com/ (2016).

15. C. Rullière, in *Femtosecond Laser Pulses - Principles and Experiments*, edited by P. D. Rullière (Springer-Verlag, Print ISBN 978-0-387-01769-3 Online ISBN 978-0-387-26674-9, 2005).

16. B. E. A. Saleh and M. C. Teich, *Fundamentals of Photonics 2nd Edition* (Wiley and Sons, ISBN: 978-0-471-35832-9, 2007).

17. T. Fuji *et al.*, Generation of smooth, ultra-broadband spectra directly from a prism-less Ti:sapphire laser. Applied Physics B **77**, 125–128 (2003).

18. A. McPherson *et al.*, Studies of multiphoton production of vacuum-ultraviolet radiation in the rare gases. Journal of the Optical Society of America B **4**, 595 (1987).

19. M. Ferray *et al.*, Multiple-harmonic conversion of 1064 nm radiation in rare gases. Journal of Physics B: Atomic, Molecular and Optical Physics **21**, L31 (1988).

20. G. Farkas and C. Tóth, Proposal for attosecond light pulse generation using laser induced multiple-harmonic conversion processes in rare gases. Physics Letters A **168**, 447 (1992).

21. P. M. Paul *et al.*, Observation of a train of attosecond pulses from high harmonic generation. Science **292**, 1689 (2001).

22. M. Hentschel *et al.*, Attosecond metrology. Nature **414**, 509–513 (2001).

23. K. Zhao *et al.*, Tailoring a 67 attosecond pulse through advantageous phase-mismatch. Optics Letters **37**, 3891–3893 (2012).

24. T. Popmintchev *et al.*, Bright Coherent Ultrahigh Harmonics in the keV X-ray Regime from Mid-Infrared Femtosecond Lasers. Science **336**, 1287-1291 (2012).

25. F. R. Elder *et al.*, Radiation from Electrons in a Synchrotron. Phys. Rev. **71**, 829–830 (1947).

26. S. C. Leemann *et al.*, Beam dynamics and expected performance of Sweden's new storage-ring light source: MAX IV. Phys. Rev. ST Accel. Beams **12**, 120701 (2009).

27. J. M. J. Madey, Stimulated Emission of Bremsstrahlung in a Periodic Magnetic Field. Journal of Applied Physics **42**, 1906-1913 (1971).

28. B. W. J. McNeil and N. R. Thompson, X-ray free-electron lasers. Nature Photonics **4**, 814-821 (2010).

29. E. Gustafsson *et al.*, Broadband attosecond pulse shaping. Optics Letters **32**, 1353–1355 (2007).

30. M. Dahlström, A. L'Huillier, and A. Maquet, Introduction to attosecond delays in photoionization. Journal of Physics B: Atomic, Molecular and Optical Physics **45**, 183001 (2012).

31. D. Guénot *et al.*, Photoemission-time-delay measurements and calculations close to the 3s-ionization-cross-section minimum in Ar. Phys. Rev. A **85**, 053424 (2012).

32. J. Mauritsson *et al.*, Coherent Electron Scattering Captured by an Attosecond Quantum Stroboscope. Phys. Rev. Lett. **100**, 073003 (2008).

33. G. Grynberg, A. Aspect, and C. Fabre, *Introduction to Quantum Optics - From the Semi-classical Approach to Quantized Light* (Cambridge University Press, ISBN-13 978-0-521-55112-0, 2010).

34. R. P. Feynman, *The Feynman Lectures on Physics Vol. 1* (Addison-Wesley, ISBN: 978-0465024933, 1964).

35. www.refractiveindex.info (2016).

36. http://henke.lbl.gov/optical_constants (2016).

37. B. Henke, E. Gullikson, and J. Davis, X-Ray Interactions: Photoabsorption, Scattering, Transmission, and Reflection at E = 50-30,000 eV, Z = 1-92. Atomic Data and Nuclear Data Tables **54**, 181 - 342 (1993).

38. S. Feng and H. G. Winful, Physical origin of the Gouy phase shift. Optics Letters **26**, 485–487 (2001).

39. J. D. Jackson, *Classical Electrodynamics 3rd Edition* (Wiley, ISBN: 9780471309321, 1999).

40. R. Syms and J. Cozens, *Optical Guided Waves and Devices* (McGraw-Hill Companies, ISBN 0-07-707425-4, 1992).

41. M. Bass *et al.*, Optical Rectification. Phys. Rev. Lett. **9**, 446–448 (1962).

42. D. H. Auston *et al.*, Cherenkov Radiation from Femtosecond Optical Pulses in Electro-Optic Media. Phys. Rev. Lett. **53**, 1555–1558 (1984).

43. F. Kadlec, P. Kužel, and J.-L. Coutaz, Optical rectification at metal surfaces. Optics Letters **29**, 2674–2676 (2004).

44. E. Witting Larsen, *Generation of tunable broadband deep ultraviolet radiation from gaseous media using ultrashort laser pulses.*, *Lund Reports in Atomic Physics* (Atomic Physics, Department of Physics, Lund University, and Institut for Fysik og Astronomi, Aarhus Universitet, 2011).

45. Y. Shen, Self-focusing: Experimental. Progress in Quantum Electronics **4**, 1 - 34 (1975).

46. J. Marburger, Self-focusing: Theory. Progress in Quantum Electronics **4**, 35 - 110 (1975).

47. F. DeMartini *et al.*, Self-Steepening of Light Pulses. Phys. Rev. **164**, 312–323 (1967).

48. W. Koechner, Thermal Lensing in a Nd:YAG Laser Rod. Applied Optics **9**, 2548–2553 (1970).

49. S. A. Akhmanov *et al.*, Observation of Parametric Amplification in the Optical Range. Sov. Phys. JETP **2**, 191–193 (1965).

50. A. Baltuška, T. Fuji, and T. Kobayashi, Controlling the Carrier-Envelope Phase of Ultrashort Light Pulses with Optical Parametric Amplifiers. Phys. Rev. Lett. **88**, 133901 (2002).

51. R. W. Boyd, *Nonlinear Optics* (Academic Press, ISBN 10: 0123694701, 2003).

52. T. Driscoll, G. Gale, and F. Hache, Ti:sapphire second-harmonic-pumped visible range femtosecond optical parametric oscillator. Optics Communications **110**, 638 - 644 (1994).

53. G. Cerullo, M. Nisoli, and S. De Silvestri, Generation of 11 fs pulses tunable across the visible by optical parametric amplification. Applied Physics Letters **71**, 3616-3618 (1997).

54. S. Rausch *et al.*, Controlled waveforms on the single-cycle scale from a femtosecond oscillator. Optics Express **16**, 9739–9745 (2008).

55. H. M. Crespo *et al.*, Nonintrusive phase stabilization of sub-two-cycle pulses from a prismless octave-spanning Ti:sapphire laser. Optics Letters **33**, 833–835 (2008).

56. D. Strickland and G. Mourou, Compression of amplified chirped optical pulses. Optics Communications **56**, 219 (1985).

57. D. Charalambidis *et al.*, *Lasers and Electro-Optics Europe (CLEO EUROPE/IQEC), 2013 Conference on and International Quantum Electronics Conference* (OSA Publishing Group, ISBN: 978-1-4799-0594-2, 2013).

58. P. Rudawski, *Second-generation High-Order Harmonic Sources - From CPA to OPCPA* (Department of Physics, Lund University, ISBN: 978-91-7473-940-4, 2014).

59. G. Cheriaux *et al.*, Aberration-free stretcher design for ultrashort-pulse amplification. Optics Letters **21**, 414–416 (1996).

60. W. Koechner, Thermal Lensing in a Nd:YAG Laser Rod. Applied Optics **9**, 2548–2553 (1970).

61. P. Schulz and S. Henion, Liquid-nitrogen-cooled Ti:Al_2O_3 laser. IEEE Journal of Quantum Electronics **27**, 1039-1047 (1991).

62. T. Oksenhendler *et al.*, Self-referenced spectral interferometry. Applied Physics B **99**, 7–12 (2010).

63. C. L. Blanc, P. Curley, and F. Salin, Gain-narrowing and gain-shifting of ultrashort pulses in Ti: sapphire amplifiers. Optics Communications **131**, 391 - 398 (1996).

64. J. Reichert *et al.*, Measuring the frequency of light with mode-locked lasers. Optics Communications **172**, 59 - 68 (1999).

65. H. Telle *et al.*, Carrier-envelope offset phase control: A novel concept for absolute optical frequency measurement and ultrashort pulse generation. Applied Physics B **69**, 327–332 (1999).

66. M. Zimmermann *et al.*, Optical clockwork with an offset-free difference-frequency comb: accuracy of sum- and difference-frequency generation.. Optics Letters **29**, 310–312 (2004).

67. T. Fuji *et al.*, Attosecond control of optical waveforms. New Journal of Physics **7**, 116 (2005).

68. C. Vozzi *et al.*, High-energy, few-optical-cycle pulses at 1.5 µm with passive carrier-envelope phase stabilization. Optics Express **14**, 10109–10116 (2006).

69. T. Fordell *et al.*, Carrier-envelope phase stabilization of a multi-millijoule, regenerative-amplifier-based chirped-pulse amplifier system. Optics Express **17**, 21091–21097 (2009).

70. S. Haessler *et al.*, Optimization of Quantum Trajectories Driven by Strong-Field Waveforms. Phys. Rev. X **4**, 021028 (2014).

71. P. W. Milonni and J. H. Eberly, *Eberly* (John Wiley and Sons, Inc, ISBN 13: 9780471627319, 1988).

72. K. C. Kulander, K. J. Schafer, and J. L. Krause, in *Super-Intense Laser-Atom Physics*, edited by B. Piraux, A. L'Huillier, and K. Rzążewski (Springer US, ISBN: 978-1-4615-7963-2, 1993), Chap. Dynamics of Short-Pulse Excitation, Ionization and Harmonic Conversion, pp. 95–110.

73. K. J. Schafer *et al.*, Above threshold ionization beyond the high harmonic cutoff. Phys. Rev. Lett. **70**, 1599 (1993).

74. P. B. Corkum, Plasma perspective on strong-field multiphoton ionization. Phys. Rev. Lett. **71**, 1994 (1993).

75. Y. Mairesse *et al.*, Attosecond Synchronization of High-Harmonic Soft X-rays. Science **302**, 1540–1543 (2003).

76. M. Lewenstein *et al.*, Theory of high-order harmonic generation by low-frequency laser fields. Phys. Rev. A **49**, 2117 (1994).

77. R. López-Martens *et al.*, Amplitude and Phase Control of Attosecond Light Pulses. Phys. Rev. Lett. **94**, 033001 (2005).

78. J. Mauritsson *et al.*, Attosecond Pulse Trains Generated Using Two Color Laser Fields. Phys. Rev. Lett. **97**, 013001 (2006).

79. J. J. Sakurai, *Modern Quantum Mechanics Revised Edition* (Addison Wesley, ISBN: 0201539292, 1993).

80. M. Dahlström, *Light-Matter Interaction on the Attosecond Timescale*, Vol. LRAP-438 of *Lund Reports on Atomic Physics* (Department of Physics, Lund University, 978-91-7473-140-8, 2011).

81. D. M. Wolkow, Über eine Klasse von Lösungen der Diracschen Gleichung. Zeitschrift für Physik **94**, 250–260 (1935).

82. L. B. Madsen, Strong-field approximation in laser-assisted dynamics. American Journal of Physics **73**, 57-62 (2005).

83. P. Salières *et al.*, Feynman's Path-Integral Approach for Intense-Laser-Atom Interactions. Science **292**, 902 (2001).

84. M. Lewenstein, P. Salières, and A. L'Huillier, Phase of the atomic polarization in high-order harmonic generation. Phys. Rev. A **52**, 4747–4754 (1995).

85. M. B. Gaarde *et al.*, Spatiotemporal separation of high harmonic radiation into two quantum path components. Phys. Rev. A **59**, 1367–1373 (1999).

86. K. Varjú *et al.*, Reconstruction of Attosecond Pulse Trains Using an Adiabatic Phase Expansion. Phys. Rev. Lett. **95**, 243901 (2005).

87. K. Varjú *et al.*, Frequency chirp of harmonic and attosecond pulses. Journal of Modern Optics **52**, 379 (2005).

88. B. H. Bransden and C. J. Joachain, *Physics of Atoms and Molecules (2nd Edition)* (Prentice Hall, ISBN 13: 978-0582356924, 2003).

89. T. Porwol *et al.*, Autoionization Versus Photoionization and Auger Decay of Physisorbed Molecular Adsorbates: Condensed Benzene on Cu (110). Physica Scripta **1992**, 197 (1992).

90. U. Fano, Effects of Configuration Interaction on Intensities and Phase Shifts. Phys. Rev. **124**, 1866–1878 (1961).

91. J.-E. Rubensson *et al.*, Influence of the Radiative Decay on the Cross Section for Double Excitations in Helium. Phys. Rev. Lett. **83**, 947–950 (1999).

92. M. Swoboda, *Attosecond Wave Packet Metrology*, Vol. 414 of *Lund Reports on Atomic Physics* (Department of Physics, Lund University, ISSN: 0281-2762, 2010).

93. S.-F. Zhao, L. Liu, and X.-X. Zhou, Multiphoton and tunneling ionization probability of atoms and molecules in an intense laser field. Optics Communications **313**, 74 - 79 (2014).

94. M. V. Ammosov, N. B. Delone, and V. P. Kraĭnov, Tunnel Ionization of Complex Atoms and of Atomic Ions in Alternating Electromagnetic Field. Sov. Phys. JETP **64**, 1191–1194 (1986).

95. N. B. Delone and V. P. Kraĭnov, Energy and angular electron spectra for the tunnel ionization of atoms by strong low-frequency radiation. Journal of the Optical Society of America B **8**, 1207–1211 (1991).

96. A. Perelomov, V. Popov, and M. Terent'ev, Ionization of Atoms in an Alternating Electric Field. Sov. Phys. JETP **23**, 924–936 (1966).

97. H. Lehmeier, W. Leupacher, and A. Penzkofer, Nonresonant third order hyperpolarizability of rare gases and N2 determined by third harmonic generation. Optics Communications **56**, 67 - 72 (1985).

98. R. P. Feynman, *The Feynman Lectures on Physics Vol. 2* (Addison-Wesley, ISBN 0-201-50064-7., 1964).

99. E. Constant *et al.*, Optimizing High Harmonic Generation in Absorbing Gases: Model and Experiment. Phys. Rev. Lett. **82**, 1668–1671 (1999).

100. T. Harada and T. Kita, Mechanically ruled aberration-corrected concave gratings. Applied Optics **19**, 3987–3993 (1980).

101. T. Harada *et al.*, Optimum design of a grazing-incidence flat-field spectrograph with a spherical varied-line-space grating. Applied Optics **38**, 2743–2748 (1999).

102. D. Simons *et al.*, UV and XUV quantum detection efficiencies of CsI-coated microchannel plates. Nuclear Instruments and Methods in Physics Research Section A: Accelerators, Spectrometers, Detectors and Associated Equipment **261**, 579 - 586 (1987).

103. P. Ranitovic *et al.*, Attosecond vacuum UV coherent control of molecular dynamics. Proceedings of the National Academy of Sciences **111**, 912-917 (2014).

104. J. Higuet *et al.*, High-order harmonic spectroscopy of the Cooper minimum in argon: Experimental and theoretical study. Phys. Rev. A **83**, 053401 (2011).

105. H. J. Shin *et al.*, Generation of Nonadiabatic Blueshift of High Harmonics in an Intense Femtosecond Laser Field. Phys. Rev. Lett. **83**, 2544–2547 (1999).

106. J. Samson and W. Stolte, Precision measurements of the total photoionization cross-sections of He, Ne, Ar, Kr, and Xe. Journal of Electron Spectroscopy and Related Phenomena **123**, 265 - 276 (2002).

107. F. Silva *et al.*, Simultaneous compression, characterization and phase stabilization of GW-level 1.4 cycle VIS-NIR femtosecond pulses using a single dispersion-scan setup. Optics Express **22**, 10181–10191 (2014).

108. M. Miranda *et al.*, Simultaneous compression and characterization of ultrashort laser pulses using chirped mirrors and glass wedges. Optics Express **20**, 688–697 (2012).

109. C. M. Heyl *et al.*, Noncollinear optical gating. New Journal of Physics **16**, 052001 (2014).

110. H. Mashiko *et al.*, Double Optical Gating of High-Order Harmonic Generation with Carrier-Envelope Phase Stabilized Lasers. Phys. Rev. Lett. **100**, 103906 (2008).

111. X. Feng *et al.*, Generation of Isolated Attosecond Pulses with 20 to 28 Femtosecond Lasers. Phys. Rev. Lett. **103**, 183901 (2009).

112. H. Vincenti and F. Quéré, Attosecond Lighthouses: How To Use Spatiotemporally Coupled Light Fields To Generate Isolated Attosecond Pulses. Phys. Rev. Lett. **108**, 113904 (2012).

113. G. Lambert *et al.*, Injection of harmonics generated in gas in a free-electron laser providing intense and coherent extreme-ultraviolet light. Nature Physics **4**, 296-300 (2008).

114. A. Mikkelsen *et al.*, Photoemission electron microscopy using extreme ultraviolet attosecond pulse trains. Review of Scientific Instruments **80**, 123703 (2009).

115. E. Mårsell *et al.*, Secondary electron imaging of nanostructures using Extreme Ultra-Violet attosecond pulse trains and Infra-Red femtosecond pulses. Annalen der Physik **525**, 162–170 (2013).

116. G. Saathoff *et al.*, Laser-assisted photoemission from surfaces. Phys. Rev. A **77**, 022903 (2008).

117. J. Mikosch and S. Patchkovskii, Coincidence and covariance data acquisition in photoelectron and -ion spectroscopy. I. Formal theory. Journal of Modern Optics **60**, 1426-1438 (2013).

118. E. Mårsell, *Photoemission Electron Microscopy for Ultrafast Nano-Optics - Femtoseconds to Attoseconds* (Division of Synchrotron Radiation Research, Department of Physics, Faculty of Science, Lund University, 978-91-7623-615-4 (pdf), 2015).

119. E. Lorek, *Time-resolved plasmonics in designed nanostructures* (Department of Physics, Lund University, ISBN: 978-91-7623-633-8, 2016).

120. E. Brüche, Elektronenmikroskopische Abbildung mit lichtelektrischen Elektronen. Zeitschrift für Physik **86**, 448–450 (1933).

121. C. M. Heyl *et al.*, High-order harmonic generation with μ J laser pulses at high repetition rates. Journal of Physics B: Atomic, Molecular and Optical Physics **45**, 074020 (2012).

122. M. Bellini *et al.*, Temporal Coherence of Ultrashort High-Order Harmonic Pulses. Phys. Rev. Lett. **81**, 297–300 (1998).

123. E. Benedetti *et al.*, Frequency chirp of long electron quantum paths in high-order harmonic generation. Optics Express **14**, 2242–2249 (2006).

124. L. He *et al.*, Spectrally resolved spatiotemporal features of quantum paths in high-order-harmonic generation. Phys. Rev. A **92**, 043403 (2015).

125. K. S. Budil *et al.*, Influence of ellipticity on harmonic generation. Phys. Rev. A **48**, R3437 (1993).

126. V. V. Strelkov, Theory of high-order harmonic generation and attosecond pulse emission by a low-frequency elliptically polarized laser field. Phys. Rev. A **74**, 013405 (2006).

127. N. I. Shvetsov-Shilovski *et al.*, Ellipticity effects and the contributions of long orbits in nonsequential double ionization of atoms. Phys. Rev. A **77**, 063405 (2008).

128. C. Vozzi *et al.*, Coherent continuum generation above 100 eV driven by an ir parametric source in a two-color scheme. Phys. Rev. A **79**, 033842 (2009).

129. A. D. Shiner *et al.*, Observation of Cooper minimum in krypton using high harmonic spectroscopy. Journal of Physics B: Atomic, Molecular and Optical Physics **45**, 074010 (2012).

130. J. W. Cooper, Photoionization from Outer Atomic Subshells. A Model Study. Phys. Rev. **128**, 681–693 (1962).

131. E. S. Toma *et al.*, Resonance-enhanced high-harmonic generation. Journal of Physics B: Atomic, Molecular and Optical Physics **32**, 5843 (1999).

132. R. Ganeev, *High-Order Harmonic Generation in Laser Plasma Plumes* (Imperial College Press, ISBN 978-1-84816-980-7, 2013).

133. N. B. Delone and V. P. Kraĭnov, AC Stark shift of atomic energy levels. Physics-Uspekhi **42**, 669 (1999).

134. M. Fieß *et al.*, Versatile apparatus for attosecond metrology and spectroscopy. Review of Scientific Instruments **81**, 093103 (2010).

135. M. Schultze *et al.*, State-of-the-art attosecond metrology. Journal of Electron Spectroscopy and Related Phenomena **184**, 68 - 77 (2011).

136. R. Locher *et al.*, Versatile attosecond beamline in a two-foci configuration for simultaneous time-resolved measurements. Review of Scientific Instruments **85**, 013113 (2014).

137. M. Huppert, I. Jordan, and H. J. Wörner, Attosecond beamline with actively stabilized and spatially separated beam paths. Review of Scientific Instruments **86**, 123106 (2015).

138. S. J. Weber *et al.*, Flexible attosecond beamline for high harmonic spectroscopy and XUV/near-IR pump probe experiments requiring long acquisition times. Review of Scientific Instruments **86**, 033108 (2015).

139. Y. Nabekawa *et al.*, Production of Doubly Charged Helium Ions by Two-Photon Absorption of an Intense Sub-10-fs Soft X-Ray Pulse at 42 eV Photon Energy. Phys. Rev. Lett. **94**, 043001 (2005).

140. D. Fabris *et al.*, Synchronized pulses generated at 20 eV and 90 eV for attosecond pump-probe experiments. Nature Photonics **9**, 383-387 (2015).

141. F. Campi *et al.*, Design and test of a broadband split-and-delay unit for attosecond XUV-XUV pump-probe experiments. Review of Scientific Instruments **87**, 023106 (2016).

142. J. Norin *et al.*, Time-Frequency Characterization of Femtosecond XUV Pulses. Phys. Rev. Lett. **88**, 193901 (2002).

143. R. López-Martens *et al.*, Amplitude and Phase Control of Attosecond Light Pulses. Phys. Rev. Lett. **94**, 033001 (2005).

144. P. Hariharan, *Basics of Interferometry Second Edition* (Academic Press, ISBN 978-0-12-373589-8, 2007).

145. S. Ek, Interferometer Design for Attosecond Experiments, (2015).

146. B. P. Abbott *et al.*, Observation of Gravitational Waves from a Binary Black Hole Merger. Phys. Rev. Lett. **116**, 061102 (2016).

147. F. Pedrotti, L. M. Pedrotti, and L. S. Pedrotti, *Introduction to Optics* 3^{rd} *Edition* (Pearson Education, ISBN 13: 978-0131499331, 2014).

148. N. Ibrakovic, Pulse Compression of Short Wavelength Infrared Optical Parametric Amplified Pulses Using a Hollow Core Capillary, (2015).

149. G. Gorju *et al.*, Active stabilization of a rapidly chirped laser by an optoelectronic digital servo-loop control. Optics Letters **32**, 484–486 (2007).

150. A. Einstein, Über einen die Erzeugung und Verwandlung des Lichtes betreffenden heuristischen Gesichtspunkt. Annalen der Physik **322**, 132–148 (1905).

151. L. Eisenbud, 1948, Unpublished PhD Thesis, Princeton, New Jersey.

152. E. P. Wigner, Lower Limit for the Energy Derivative of the Scattering Phase Shift. Phys. Rev. **98**, 145–147 (1955).

153. P. Hockett *et al.*, Time Delay in Molecular Photoionization. ArXiv e-prints **1**, 1–10 (2015).

154. M. Miranda, *Sources and Diagnostics for Attosecond Science*, Vol. LRAP-466 of *Lund Reports on Atomic Physics* (Atomic Physics, Department of Physics, Lund University, 978-91-7473-392-1, 2012).

155. R. Trebino *et al.*, Measuring ultrashort laser pulses in the time-frequency domain using frequency-resolved optical gating. Review of Scientific Instruments **68**, 3277-3295 (1997).

156. J. Mauritsson *et al.*, Measurement and control of the frequency chirp rate of high-order harmonic pulses. Phys. Rev. A **70**, 021801 (2004).

157. Y. Mairesse and F. Quéré, Frequency-resolved optical gating for complete reconstruction of attosecond bursts. Phys. Rev. A **71**, 011401 (2005).

158. S. Nagele *et al.*, Time-resolved photoemission by attosecond streaking: extraction of time information. Journal of Physics B: Atomic, Molecular and Optical Physics **44**, 081001 (2011).

159. M. Sabbar *et al.*, Resonance Effects in Photoemission Time Delays. Phys. Rev. Lett. **115**, 133001 (2015).

160. V. Véniard, R. Taïeb, and A. Maquet, Phase dependence of (N+1)-color (N>1) ir-uv photoionization of atoms with higher harmonics. Phys. Rev. A **54**, 721–728 (1996).

161. J. Mauritsson, M. B. Gaarde, and K. J. Schafer, Accessing properties of electron wave packets generated by attosecond pulse trains through time-dependent calculations. Phys. Rev. A **72**, 013401 (2005).

162. P. Eckle *et al.*, Attosecond Ionization and Tunneling Delay Time Measurements in Helium. Science **322**, 1525–1529 (2008).

163. A. Ludwig *et al.*, Breakdown of the Dipole Approximation in Strong-Field Ionization. Phys. Rev. Lett. **113**, 243001 (2014).

164. J. M. Dahlström and E. Lindroth, Study of attosecond delays using perturbation diagrams and exterior complex scaling. Journal of Physics B: Atomic, Molecular and Optical Physics **47**, 124012 (2014).

165. D. W. Chandler and P. L. Houston, Two-dimensional imaging of state-selected photodissociation products detected by multiphoton ionization. The Journal of Chemical Physics **87**, 1445-1447 (1987).

166. R. Dörner *et al.*, Cold Target Recoil Ion Momentum Spectroscopy: a 'momentum microscope' to view atomic collision dynamics. Physics Reports **330**, 95 - 192 (2000).

167. C. Palatchi *et al.*, Atomic delay in helium, neon, argon and krypton. Journal of Physics B: Atomic, Molecular and Optical Physics **47**, 245003 (2014).

168. C. Cirelli *et al.*, Energy-Dependent Photoemission Time Delays of Noble Gas Atoms Using Coincidence Attosecond Streaking. IEEE Journal of Selected Topics in Quantum Electronics **21**, 1-7 (2015).

169. A. F. Starace, Behavior of partial cross sections and branching ratios in the neighborhood of a resonance. Phys. Rev. A **16**, 231–242 (1977).

170. S. L. Sörensen *et al.*, Argon 3s autoionization resonances. Phys. Rev. A **50**, 1218–1230 (1994).

171. T. Carette *et al.*, Multiconfigurational Hartree-Fock close-coupling ansatz: Application to the argon photoionization cross section and delays. Phys. Rev. A **87**, 023420 (2013).

172. A. Jiménez-Galán, L. Argenti, and F. Martín, Modulation of Attosecond Beating in Resonant Two-Photon Ionization. Phys. Rev. Lett. **113**, 263001 (2014).

173. P. Salières *et al.*, Conference talk. Atto2015: Phase spectroscopy of resonant photo-ionization: Accessing attosecond delays and wavepacket dynamics (2015).

174. E. Goulielmakis *et al.*, Real-time observation of valence electron motion. Nature **466**, 739-743 (2010).

175. H. Wang *et al.*, Attosecond Time-Resolved Autoionization of Argon. Phys. Rev. Lett. **105**, 143002 (2010).

176. C. Ott *et al.*, Reconstruction and control of a time-dependent two-electron wave packet. Nature **516**, 374–378 (2014).

177. A. R. Beck *et al.*, Attosecond transient absorption probing of electronic superpositions of bound states in neon: detection of quantum beats. New Journal of Physics **16**, 113016 (2014).

178. C.-T. Liao *et al.*, Beyond the Single-Atom Response in Absorption Line Shapes: Probing a Dense, Laser-Dressed Helium Gas with Attosecond Pulse Trains. Phys. Rev. Lett. **114**, 143002 (2015).

179. M. Wu *et al.*, Time-domain perspective on Autler-Townes splitting in attosecond transient absorption of laser-dressed helium atoms. Phys. Rev. A **88**, 043416 (2013).

180. J. Vura-Weis *et al.*, Femtosecond $M_{2,3}$-Edge Spectroscopy of Transition-Metal Oxides: Photoinduced Oxidation State Change in α-Fe_2O_3. The Journal of Physical Chemistry Letters **4**, 3667-3671 (2013).

181. A. H. Zewail, Femtochemistry: Atomic-Scale Dynamics of the Chemical Bond. The Journal of Physical Chemistry A **104**, 5660-5694 (2000).

182. R. Mathies *et al.*, Direct observation of the femtosecond excited-state cis-trans isomerization in bacteriorhodopsin. Science **240**, 777–779 (1988).

183. F. Ráksi *et al.*, Ultrafast x-ray absorption probing of a chemical reaction. The Journal of Chemical Physics **104**, 6066-6069 (1996).

184. Z.-H. Loh *et al.*, Quantum State-Resolved Probing of Strong-Field-Ionized Xenon Atoms Using Femtosecond High-Order Harmonic Transient Absorption Spectroscopy. Phys. Rev. Lett. **98**, 143601 (2007).

185. C. Ott *et al.*, Lorentz Meets Fano in Spectral Line Shapes: A Universal Phase and Its Laser Control. Science **340**, 716-720 (2013).

186. R. G. Brewer and R. L. Shoemaker, Optical Free Induction Decay. Phys. Rev. A **6**, 2001–2007 (1972).

187. F. A. Hopf, R. F. Shea, and M. O. Scully, Theory of Optical Free-Induction Decay and Two-Photon Superradiance. Phys. Rev. A **7**, 2105–2110 (1973).

188. F. Bloch, Nuclear Induction. Phys. Rev. **70**, 460–474 (1946).

189. E. L. Hahn, Nuclear Induction Due to Free Larmor Precession. Phys. Rev. **77**, 297–298 (1950).

190. R. Damadian, Tumor Detection by Nuclear Magnetic Resonance. Science **171**, 1151–1153 (1971).

191. A. Filler, The History, Development and Impact of Computed Imaging in Neurological Diagnosis and Neurosurgery: CT, MRI, and DTI. Nature Precedings , 1-76 (2009).

192. R. P. Feynman, F. L. Vernon, and R. W. Hellwarth, Geometrical Representation of the Schrödinger Equation for Solving Maser Problems. Journal of Applied Physics **28**, 49-52 (1957).

193. L. Rippe, *Quantum computing with naturally trapped sub-nanometre-spaced ions* (Department of Physics, Lund University, ISBN: 978-91-628-6907-6, 2006), p. 1.

194. C.-T. Liao *et al.*, Attosecond transient absorption in dense gases: Exploring the interplay between resonant pulse propagation and laser-induced line-shape control. Phys. Rev. A **93**, 033405 (2016).

195. R. H. Dicke, Coherence in Spontaneous Radiation Processes. Phys. Rev. **93**, 99–110 (1954).

196. R. Bonifacio and L. A. Lugiato, Cooperative radiation processes in two-level systems: Superfluorescence. Phys. Rev. A **11**, 1507–1521 (1975).

197. R. Jodoin and L. Mandel, Superradiance in an inhomogeneously broadened atomic system. Phys. Rev. A **9**, 873–884 (1974).

198. R. Jodoin and L. Mandel, Superradiance and optical free induction. Phys. Rev. A **10**, 1898–1903 (1974).

199. M. O. Scully and A. A. Svidzinsky, The Super of Superradiance. Science **325**, 1510–1511 (2009).

200. M. Chini *et al.*, Coherent phase-matched VUV generation by field-controlled bound states. Nature Photonics **8**, 437-441 (2014).

201. M. B. Gaarde *et al.*, Transient absorption and reshaping of ultrafast XUV light by laser-dressed helium. Phys. Rev. A **83**, 013419 (2011).

202. D. Kroon, *Attosecond interferometry: techniques and spectroscopy* (Department of Physics, Lund University, 978-91-7623-689-5, 2016).

203. J. Tate *et al.*, Scaling of Wave-Packet Dynamics in an Intense Midinfrared Field. Phys. Rev. Lett. **98**, 013901 (2007).

204. A. D. Shiner *et al.*, Wavelength Scaling of High Harmonic Generation Efficiency. Phys. Rev. Lett. **103**, 073902 (2009).

205. A. M. Weiner, Femtosecond pulse shaping using spatial light modulators. Review of Scientific Instruments **71**, 1929-1960 (2000).

206. J. Mauritsson *et al.*, Sub-cycle control of attosecond pulse generation using two-colour laser fields. Journal of Physics B: Atomic, Molecular and Optical Physics **42**, 134003 (2009).

207. N. Ibrakovic, Design and Calculations of a Broadband Two Color Inline Interferometer, 2014, (2014).

208. F. Dyson, A meeting with Enrico Fermi. Nature **427**, 297-297 (2004).

209. J. Mayer, K. Khairy, and J. Howard, Drawing an elephant with four complex parameters. American Journal of Physics **78**, 648-649 (2010).

Papers

Paper I

High-order harmonic generation using a high-repetition-rate turnkey laser

E. Lorek, E.W. Larsen, C.M. Heyl, S. Carlström, D. Paleček, D. Zigmantas and J. Mauritsson.

Review of Scientific Instruments **85**, 123106 (2014).

Paper II

Sub-cycle ionization dynamics revealed by trajectory-resolved, elliptically-driven high-order harmonic generation

E.W. Larsen, S. Carlström, E. Lorek, C.M. Heyl, D. Paleček, K. J. Schafer, A. L'Huiller, D. Zigmantas and J. Mauritsson.

Submitted for publication.

Paper III

Spatially and spectrally resolved quantum path interference with chirped driving pulses

J. Preclíková, S. Carlström, E. Lorek, E. W. Larsen, C. M. Heyl, D. Paleček, D. Zigmantas, K. J. Schafer, M. Gaarde, and J. Mauritsson.

Submitted for publication.

Paper IV

Carrier-envelope phase-dependent high-order harmonic generation with a high-repetition-rate OPCPA system

P. Rudawski, A. Harth, C. Guo, E. Lorek, M. Miranda, C.M. Heyl, E.W. Larsen, J. Ahrens, O. Prochnow, T. Binhammer, U. Morgner, J. Mauritsson, A. L'Huillier and C.L. Arnold.

The European Physical Journal D **69**, 1434-6060 (2015).

Paper V

Measurements of relative photoemission time delays in noble gas atoms

D. Guénot, D. Kroon, E. Balogh, E. W. Larsen, M. Kotur, M. Miranda, T. Fordell, P. Johnsson, J. Mauritsson, M. Gisselbrecht, K. Varjú, C. L. Arnold, T. Carette, A. S. Kheifets, E. Lindroth, A. L'Huillier and J. M. Dahlström.

Journal of Physics B: Atomic, Molecular and Optical Physics **47**, 245602 (2014).

.

Paper VI

Attosecond pulse walk-off in high-order harmonic generation

D. Kroon, D. Guénot, M. Kotur, E. Balogh, E. W. Larsen,
C. M. Heyl, M. Miranda, M. Gisselbrecht, J. Mauritsson, P. Johnsson,
K. Varjú, A. L'Huillier and C. L. Arnold.

Optics Letters **39**, 2218-2221 (2014).

Paper VII

Spectral phase measurement of a Fano resonance using tunable attosecond pulses

M. Kotur, D. Guénot, Á. Jiménez-Galán, D. Kroon, E. W. Larsen, M. Louisy, S. Bengtsson, M. Miranda, J. Mauritsson, C. L. Arnold, S. E. Canton, M. Gisselbrecht, T. Carette, J. M. Dahlström, E. Lindroth, A. Maquet, L. Argenti, F. Martín and A. L'Huillier.

(2016) *Nature Communications.*

Paper VIII

Gating attosecond pulses in a noncollinear geometry

M. Louisy, C. L. Arnold, M. Miranda, E. W. Larsen, S. N. Bengtsson, D. Kroon, M. Kotur, D. Guénot, L. Rading, P. Rudawski, F. Brizuela, F. Campi, B. Kim, A. Jarnac, A. Houard, J. Mauritsson, P. Johnsson, A. L'Huillier, and C. M. Heyl.

Optica **2**, 563-566 (2015).

Paper IX

Controlled free induction decay in the extreme ultraviolet

E.W. Larsen, S. Bengtsson, D. Kroon, S. Camp, M. Miranda, C. L. Arnold, A. L'Huillier, K. J. Schafer, M. Gaarde, L. Rippe, and J. Mauritsson.

Manuscript in preparation.

Paper X

Photoemission electron microscopy of localized surface plasmons in silver nanostructures at telecommunication wavelengths

E. Mårsell, E. W. Larsen, C. L. Arnold, H. Xu, J. Mauritsson, and A. Mikkelsen.

Journal of Applied Physics **117**, 083104 (2015).